Forschungsbericht 2020-47

Contribution to Load Alleviation in Aircraft Predesign and Its Influence on Structural Mass and Fatigue

Vega Handojo

Deutsches Zentrum für Luft- und Raumfahrt
Institut für Aeroelastik
Göttingen

DLR Deutsches Zentrum für Luft- und Raumfahrt

Forschungsbericht 2020-47

Contribution to Load Alleviation in Aircraft Pre-design and Its Influence on Structural Mass and Fatigue

Vega Handojo

Deutsches Zentrum für Luft- und Raumfahrt
Institut für Aeroelastik
Göttingen

150 Seiten
88 Bilder
41 Tabellen
107 Literaturstellen

Deutsches Zentrum
DLR für Luft- und Raumfahrt

Contribution to Load Alleviation in Aircraft Pre-design and Its Influence on Structural Mass and Fatigue

vorgelegt von

Vega Handojo, M.Sc.

ORCID iD 0000-0001-6030-2383

an der Fakultät V – Verkehrs- und Maschinensysteme

der Technischen Universität Berlin

zur Erlangung des akademischen Grads

Doktor der Ingenieurwissenschaften

- Dr. Ing. -

genehmigte Dissertation

Promotionsausschuss:

Vorsitzender:	Prof. Dr.-Ing. Henning Jürgen Meyer
Gutachter:	Prof. Dr.-Ing. Robert Luckner
Gutachter:	Prof. Dr.-Ing. Wolf-Reiner Krüger
Gutachter:	Dr.-Ing. Thomas Klimmek

Tag der wissenschaftlichen Aussprache: 04. September 2020

Berlin 2020

Abstract

This thesis develops and demonstrates an aircraft pre-design process for loads analysis, load alleviation, structural optimization and fatigue analysis. It is shown that the consideration of maneuver and gust load alleviation in early design stages is a promising concept to reduce wing bending moments, structural mass and extend the fatigue life. The reference aircraft considered are two mid-range configurations: one with a backward and another one with a forward swept wing, respectively.

In the loads analysis, quasi-steady maneuvers and dynamic 1-cos gusts are considered. For the load alleviation during maneuvers, the ailerons are deflected symmetrically with pre-calculated amplitudes. For the gust load alleviation, a feed-forward, proportional control algorithm is set up and the main input for the controller is the gust angle of attack. Analogous to maneuver load alleviation, the ailerons are deflected symmetrically.

With the post-processed loads from the simulations, the structure of the wing and horizontal tailplane (HTP) is optimized toward mass minimization. The constraints considered are material strength, buckling stability and static aeroelastic requirements. The steps loads analysis and structure optimization of the developed design process are conducted iteratively until the wing box mass converges. For the reference aircraft, the load alleviation yields a reduction of wing box mass by 2.8% and 6.1%, respectively.

Beyond that, a qualitative fatigue analysis is carried out to compare the fatigue behaviors of the active and passive aircraft (with and without load alleviation). In this step, loads due to continuous turbulence and ground-air-ground cycles are considered. For the reference missions, the fatigue life of the active aircraft is improved by 28% and 12% respectively, on top of the mass benefit. However, these numbers of fatigue life improvement are only valid for the considered loads and selected positions. If more loading conditions or structure elements are taken into account, the fatigue benefit may vary.

As a conclusion, the proposed process can serve to gain an insight into the benefits of load alleviation for a given aircraft in the pre-design phase, before it advances to the next design stage.

Keywords: load alleviation, loads analysis, structural optimization, fatigue analysis, aircraft pre-design, feed-forward control

Kurzfassung

In dieser Arbeit wird ein Prozess zur Lastanalyse, Lastabminderung, Strukturoptimierung und Ermüdungsanalyse im Flugzeugvorentwurf entwickelt und demonstriert. Dabei wird gezeigt, dass bei Berücksichtigung von Manöver- und Böenlastabminderung in den frühen Phasen des Flugzeugentwurfs die Biegemomente am Flügel und die Strukturmasse reduziert, und die Lebensdauer der Struktur verlängert werden kann. Die für die Untersuchung verwendeten Referenzflugzeuge sind zwei Mittelstreckenkonfigurationen, jeweils eine mit einem rückwärts und eine mit einem vorwärts gepfeilten Flügel.

In der Lastanalyse werden quasistatische Manöver und dynamische 1-cos-Böen berücksichtigt. Die Lastabminderung bei Manövern geschieht durch symmetrisch ausgeschlagene Querruder. Für die Böenlastabminderung wird ein proportionaler Vorsteuer-algorithmus entwickelt, dabei stellt der Böenanstellwinkel die Eingangsgröße für die Vorsteuerung dar. Analog zur Manöverlastabminderung werden hierbei die Querruder symmetrisch ausgeschlagen.

Mit ausgewählten Lasten aus der Lastanalyse wird die Struktur des Flügels und des Höhenleitwerks hinsichtlich minimaler Strukturmasse optimiert. Die in der Struktur-optimierung berücksichtigten Randbedingungen sind Zugfestigkeit des Materials, Beulstabilität und statische aeroelastische Anforderungen. Die Lastanalyse und Strukturoptimierung im entwickelten Entwurfsprozess wird iterativ durchgeführt, bis die Flügelmasse konvergiert. Bei den Referenzflugzeugen ergeben sich Masseneinsparungen für den Flügelkasten von jeweils 2,8% bzw. 6,1%.

Darüber hinaus wird eine Ermüdungsanalyse durchgeführt, um das Ermüdungsverhalten der aktiven und passiven Flugzeuge (mit und ohne Lastabminderung) zu vergleichen. Dabei werden Lasten aufgrund von kontinuierlicher Turbulenz und von Boden-Luft-Boden-Zyklen berücksichtigt. Für die ausgewählten Referenzmissionen erhöht sich die Lebensdauer der Flugzeuge mit aktiver Lastabminderung jeweils um 28% bzw. 12%, zusätzlich zu der Masseneinsparung. Die Werte gelten jedoch nur für die berücksichtigten Lastkonditionen und Positionen. Falls weitere Lastszenarien oder Strukturelemente berücksichtigt werden, kann die Erhöhung der Lebensdauer variieren.

Insgesamt ermöglicht der entwickelte Vorentwurfsprozess, den Nutzen der Lastabminderung bei einem gegebenen Flugzeug zu berücksichtigen, bevor dieses in die nächste Entwurfsphase voranschreitet.

Stichwörter: Lastabminderung, Lastanalyse, Strukturoptimierung, Ermüdungsanalyse, Flugzeugvorentwurf, Vorsteuerung

Acknowledgments

Since my Bachelor's studies, I have been interested in the multidisciplinary world of aircraft design, and I am grateful to have the opportunity to do research on the topic. This thesis evolved during my employment as research scientist at DLR German Aerospace Center, Institute of Aeroelasticity in Göttingen, Germany.

My gratitude goes to Prof. Dr. Robert Luckner for supervising, supporting the thesis, for the time and the fruitful discussions. I would like to thank Prof. Dr. Wolf Krüger for giving me the freedom and opportunity to write this thesis, for the supervision and support for its entire duration. Moreover, I would like to thank Dr. Thomas Klimmek for introducing me to aeroelastic modeling and design, for providing the baseline models of the reference aircraft, for supervising and supporting this thesis.

Many thanks go to my colleagues (and former colleagues) at the institute who supported my work in various ways. Dr. Markus Ritter introduced me to DLM and its applications, Matthias Schulze supported me in learning about gust loads in the beginning of my time at DLR. Dr. Arne Voß and I worked on our theses in roughly the same period and our topics have similarities, so that we could motivate each other and have technical discussions. Dr. Gabriel Pinho Chiozzotto inspired me with his expertise in aircraft conceptual design. I would also like to thank Dr. David Quero for the helpful discussions, both regarding technical topics or PhD in general. Furthermore, I would like to thank Yasser Meddaikar for the fruitful discussions, among others regarding composite materials. Many thanks go to Kjell Bramsiepe and Kautuk Sinha for their support and help in the projects. My thanks go to the whole institute as well, I have been enjoying my time at DLR and it is a pleasure to have colleagues to share after-work evenings, go on holidays and play music with.

I would also like to thank Dr. Roeland De Breuker for supervising and motivating me during my research stay in Delft. My thanks also go to Paul Lancelot for the pleasant and successful collaboration, and to all colleagues in Delft for the hospitality.

Moreover, I would like to thank my schoolmates: Philipp, Máté, Martin and Daniel for their morale support. Last but not least, I would like to express my gratitude to my parents who have made all this possible, for always supporting, encouraging me and for teaching me to stay curious and persistent.

Göttingen, November 2020

Table of content

List of figures

List of tables

Nomenclature

Abbreviations

AIC	: aerodynamic influence coefficient matrix
ALLEGRA	: DLR project, AeroeLastic stability and Loads prediction for Enhanced GReen Aircraft
ATC	: air traffic control
CAS	: calibrated airspeed
CG	: center of gravity
CS	: coordinate system
CPACS	: Common Parametric Aircraft Configuration Schema
CS25	: Certification Specifications and Acceptable Means of Compliance for Large Aeroplanes
DLM	: doublet lattice method
DLR	: German Aerospace Center
EAS	: equivalent airspeed
EFCS	: electronic flight control system
FCC	: flight control computer
FE	: finite element
FL	: flight level
GLA	: gust load alleviation
HTP	: horizontal tailplane
iLOADS	: DLR project on integrated loads analysis
LamAiR	: DLR project, Laminar Aircraft Research
LIDAR	: light detection and ranging
LRA	: load reference axis
MAC	: mean aerodynamic chord
MDO	: multidisciplinary optimization
ModGen	: Model Generator, an in-house program to generate Nastran simulation models
MLA	: maneuver load alleviation
MLM	: maximum landing mass
MONA	: ModGen-Nastran, a process to generate and optimize FE models
MSC.Nastran	: commercial FE program
MTOM	: maximum take-off mass
MZFM	: maximum zero fuel mass
OEM	: operating empty mass
PSD	: power spectral density
RAM	: random-access memory
RMS	: root mean square
SOL101	: static loads analysis in MSC.Nastran

SOL144 : quasi-steady aeroelastic analysis in MSC.Nastran
SOL145 : flutter analysis in MSC.Nastran
SOL146 : dynamic aeroelastic analysis in MSC.Nastran
SOL200 : structural optimization in MSC.Nastran
TAS : true airspeed
TF : transfer function
VAMP : DLR project, Virtual Aircraft Multidisciplinary Analysis and Design Processes
VTP : vertical tailplane

Latin alphabet

A : aerodynamic influence coefficient matrix in general
B : damping matrix in general
b : buckling field width
C : constants in general
$\bar{c}$: mean aerodynamic chord
c_L : lift coefficient
$c_{l\xi}$: roll moment coefficient due to aileron deflection
c_p : pressure coefficient
D : differentiation matrix in general
D_F : fatigue damage
d : artificial damping
E : tensile modulus
F : aerodynamic force in general
F_g : gust alleviation factor
F_z : shear force
F_S : safety factor
f : frequency
f_{opt} : objective function in structural optimization
G : coupling matrix in general
g : gravitational acceleration
g_c : optimization constraints
H : gust gradient
i : imaginary number
K : structural stiffness matrix in general
k : reduced frequency
k_a : GLA amplification factor in the aerodynamic coordinate system
k_c : compressive buckling coefficient
k_{GLA} : gain of gust load alleviation
k_s : shear buckling coefficient
L : turbulence scale
M : mass matrix in general
M_x : bending moment
M_y : torsion moment, hinge moment
Ma : Mach number

m_{MTO} : maximum take-off mass
N : number of cycles to failure in general
n : number of elements in general, S-N curve exponent in general
n_z : vertical load factor
P : force on structural nodes in general
p : roll velocity
p_f : flutter eigenvalue
Q : aerodynamic matrix in general
q : pitch velocity
$\bar{q}$: dynamic pressure
R : mass ratio in general
r : yaw velocity
r_s : stress or strain ratio
r_{CG} : distance between aerodynamic sensor and aircraft center of gravity
rms : root mean square in general
S : wing reference area
TF : transfer function in general
t : material thickness
t_{del} : delay time
U : gust speed in general
u : displacement in general
V_A : design maneuvering speed
V_C : design cruise speed – not necessarily equal with the economic cruise speed
V_D : design dive speed
V_{MO} : maximum operating speed
V_S : stall speed
V_{TAS} : true airspeed
w : downwash in general
w_g : vertical wind speed
x : aircraft response quantity in general, longitudinal coordinate
x_g : distance penetrated into gust
x_v : design variable
x_{wing} : longitudinal position of the wing
y : lateral displacement, lateral coordinate
y_v : analysis variable
Z : altitude
z : vertical displacement

Greek alphabet

α : angle of attack
β : slip angle
δ : twist angle
ϵ : strain in general
η : elevator or control surface deflection in general
θ : aircraft pitch angle
μ : potential doublet strength

ν	: Poisson ratio
ξ	: aileron deflection
π	: circle constant
ρ	: air density
σ	: stress in general
τ	: shear stress
Φ	: turbulence power spectral density
φ	: phase angle, sweep angle
ω	: circular frequency

Notation conventions

[ ]	: matrix
{}	: vector
$\dot{(\,)}$	: first derivative
$\ddot{(\,)}$	: second derivative

1 Introduction

1.1 Motivation

The design of new aircraft is a long, complex multidisciplinary process. It has to comply with a variety of requirements, among others regarding safety and performance. At the same time, manufacturers strive to minimize the aircraft's development risk and optimize the production as well as operational cost, where each of those factors is already a challenge itself.

To minimize the aircraft's development risk and time, it is advisable to shift as many analyses and calculations as possible to earlier stages of the design. This is due to the fact that the aircraft becomes more complex with every the design stage, so that a late consideration and implementation of functions/technologies is more expensive and time consuming.

One solution to lower the aircraft's operational cost is by minimizing the fuel consumption. This can be achieved e.g. by reducing the structural mass. At the same time, the structural mass directly depends on the design loads. Hence, structural mass can be reduced by alleviating the design loads. One possible method is by using active control to redistribute lift during maneuvers or reduce lift increments induced by gusts or turbulence. Nowadays, active load alleviation is implemented on commercial transport aircraft as a part of the electronic flight control system (EFCS). However, before the load alleviation is well adjusted to the aircraft, it has to be modeled in the design process first – the earlier the better.

Depending on the stage of the aircraft design process, the suitable modeling depth of the load alleviation also varies. In the conceptual stage, empirical regression formulae – including technology factors for load alleviation – are often used since information about the aircraft is insufficient. In the preliminary design stage, the aircraft configuration is frozen and more details about the aircraft are known. In this case, a physics-based modeling of load alleviation systems is seen as appropriate since it can be efficiently integrated into the physics-based loads analysis as shown by this thesis. With a physics-based method, there are more degrees of freedom in setting the load alleviation parameters to maximize the load reduction. However, the algorithm should be computer-time efficient so that the load calculations, which can comprise hundreds or more load cases, are considerably fast. These large number of load cases argue against the use of high-fidelity methods such as computational fluid dynamics (CFD). Besides, CFD grids are not always available for any aircraft in the early design stages.

With differences in the design loads between the aircraft with and without alleviation, differences in the structural masses are expected. These changes in the structural masses will also likely influence the fatigue behavior of the aircraft. Therefore, to gain an understanding of the interdependency between load alleviation, structural mass and fatigue, all three aspects should be investigated simultaneously. Even if a quantitative statement concerning the fatigue behavior e.g. "the aircraft can survive x flight cycles" cannot be made in the pre-design yet, a qualitative trend can be obtained using relatively simple analysis methods.

1.2 State of the art

Based on the motivation in Section 1.1, an overview of literature references from the fields related to this thesis is provided. The first references comprise methods of gust and maneuver loads analysis that are essential for designing and optimizing aircraft structures. These are followed by references on active control technology on aircraft, the functions that are available and the applications that exist. Development of load alleviation technology in research is also elaborated, followed by a brief overview of fatigue analysis.

Gust and turbulence loads analysis

Gust loads have been investigated since the beginning of aviation, and the theory of an airplane encountering gusts has been described in the first NACA report from 1915 by Hunsaker et al. [43]. Over the years, methods of gust loads analysis with various levels of fidelity have been developed for aircraft design and certification [30]. Those can be classified into quasi-steady and dynamic methods.

Examples of the quasi-steady approach are the method from Rhode and Lundquist [81], where the gust is assumed to have a sharp edge, and the method of Pratt with the assumption of a 1-cos gust shape [74]. Until 2017, the Pratt method was used for the certification specifications for smaller aircraft with up to 19 passengers or a maximum take-off mass up to 8168 kg (19000 lbs) as described in EASA CS23 (until Amendment 4) [19]. In the earlier version of European and US American certification specifications for large aircraft JAR25 [45] and FAR25 [24], the Pratt method was also utilized to calculate gust loads until dynamic simulations became obligatory in change 14 of JAR25 since 1994 [46] (today CS25) and in FAR25 since 1996 [23].

To model the aerodynamics in dynamic simulations, there have been a large range of methods such as the doublet lattice method (DLM) in the frequency domain, developed by Albano et al. [3] and implemented in MSC.Nastran [64], or the computational fluid dynamics (CFD) in the time domain, as described by Harlow et al. [38] and Raveh [78]. For certification, gust loads have to be calculated in the entire flight envelope of the aircraft in combination with various mass configurations and gust parameters. In CS25 [20], there are two approaches to be considered, the first one assumes discrete 1-cos gusts. Methods of calculation of 1-cos gust loads in the frequency domain for whole aircraft configurations have been described by Stauffer et al. [89], Crimaldi et al. [13] and Handojo et al. [35]. To identify the gust evoking the highest loads, Khodaparast et al. [52] developed an interpolation method employing a Gaussian process (kriging).

The second approach in CS25 incorporates continuous atmospheric turbulence where von Kármán turbulence spectra with a turbulence scale of 2500 feet are assumed [20]. A turbulence loads analysis method using power spectral techniques has been introduced by Houbolt [42]. While 1D turbulence analysis is necessary for certification, Teufel [92] and Crimaldi et al. [13] researched the modeling of 2D turbulence. With 2D turbulence, smaller fluctuations of the wing root bending moment compared to 1D turbulence have been observed. However, other load quantities show higher values, such as shear stress in the rear

section of an airliner as stated by Teufel [92], the torsion on Northrop Grumman B-2 as mentioned by Crimaldi et al. [13] and the wing torsion of Lockheed L-1011 as written by Hoblit [40]. According to Crimaldi et al. [13], the stress increase is to be considered in correlation with structure fatigue.

Beyond that, approaches such as the statistical discrete gust, matched filter theory, random process theory and solution of the Lyapunov equation have been developed [27,73]. Jones [48] describes the statistical discrete gust method where gust profiles are generated using step functions based on defined probability distributions. The method enables an assembly of a sizing relevant gust profile in the time domain, e.g. for the wing root bending moment. The sizing relevant gust profile can also be identified with the matched filter theory and random process theory as proposed by Pototzky et al. [73]. A recent development in gust loads analysis is Loads Kernel, a DLR in-house simulation platform developed by Voß [97]. Loads Kernel incorporates the flight mechanics according to Waszak et al. [98] and enables simulations in the time domain.

Maneuver loads analysis

Analogous to gust loads analysis, maneuver load analysis can be performed with various modeling depths. Example of a maneuver simulation method with potential theoretical aerodynamics is the vortex-lattice method (VLM) implemented in MSC.Nastran [65] or by Voß [97], where the latter combines the maneuver and gust analysis in one single simulation run. Maneuver simulations with consideration of nonlinear effects such as shock waves in transonic flow conditions can be carried out with CFD as shown by Dean et al. [15] as well as by Ritter et al. [82].

For certification according to CS25.331 [20], maneuvers in balanced (zero pitch acceleration) and pitching conditions (with pitch acceleration) must be investigated. For the sizing loads on the wing however, maneuvers with zero pitch acceleration are expected to be more relevant.

Active control technology and load alleviation on aircraft

Research activities concerning active control technology (ACT) [17,41] began in the 1960’s. With the introduction of fly-by-wire and electronic flight control system, the implementation of additional active control functions became simpler, so that the degrees of freedom of using the available control surfaces became more diverse. Active control can be utilized to fulfill flight control functions, such as ride comfort improvement, and also structural functions, such as load alleviation, mode control and flutter suppression, as described by Brockhaus et al. [7] and Regan et al. [80].

An early example of active control from the 1960’s is the Load Alleviation and Mode Stabilization (LAMS) on the Boeing B-52 described by Burris et al. [9]. The function has been incorporated to reduce fatigue loads due to turbulence by increasing the damping of the rigid body motion and selected elastic modes. On the Lockheed C-5A, Disney [17] describes an Active Lift Distribution Control System (ALDCS) that has been implemented to decrease wing bending loads due to both gusts and maneuvers. Brockhaus et al. [7] state that the Airbus A320 had a load alleviation function based on acceleration feedback and involves the

deflection of ailerons and spoilers during extreme gust and turbulence encounter. On the Northrop Grumman B-2, the wing bending moment due to continuous turbulence has been significantly reduced by using a gust load alleviation (GLA) system, according to Britt et al. [6]. On the Lockheed L-1011, a maneuver load alleviation (MLA) system is implemented to increase the wingspan without having to extensively reinforce the structure, as described by Ramsey et al. [77]. Another example of active control is the Load Alleviation and Ride Smoothing (LARS) system by König et al. [55] that has been tested on the modified VFW-614 aircraft ATTAS (Advanced Technologies Testing Aircraft System). Its aim is to reduce vertical accelerations of the aircraft in gusty weather. The system uses the angle of attack data as input to control the rigid body motion with direct lift control (DLC) flaps. Since the controller is a feed-forward system, it has the advantage that the stability and dynamic characteristics of the aircraft remain unchanged [56]. For lateral gusts, Hoblit [39] states that the presence of a yaw damper on the Lockheed L-1011 leads to a shear force reduction by up to 27% by increasing the damping of the Dutch roll mode. Furthermore, control systems to improve ride comfort by increasing the damping of fuselage modes are found on the Boeing 747, Boeing 777 and Airbus A340, according to Hönlinger et al. [41] and Teufel [92]. Moreover, Reckzeh [79] describes a multifunctional flap system to optimize the lift distribution on the Airbus A350 XWB during cruise flight.

Simulations and experiments with load alleviation

A typical aim of load alleviation using active control is to reduce the wing bending moment since it influences the wing structural mass significantly [41,105]. Depending on the aircraft, the maximum bending moment in flight is reached either due to design maneuvers or design gusts [62]. Nevertheless, Xu [105] states that both maneuver and gust load alleviation system should be implemented simultaneously to maximize the benefit of load alleviation.

Load alleviation in quasi-steady longitudinal, book-case maneuvers according to CS25 can be achieved by a symmetric deflection of the wing control surfaces [105]. However, in transient maneuver and dynamic gust simulations, a control system is required. Examples of control systems for transient maneuvers have been developed by Burlion et al. [8], Paletta [69] and Woods-Vedeler et al. [103].

Concerning gust load alleviation (GLA) in simulations and experiments, various control systems have been developed and the modeling depth also varies. The GLA system proposed by Xu [105] incorporates a rather simple proportional derivative (PD) controller, while the GLA proposed by Capello et al. [10] utilizes a comprehensive robust adaptive controller. Furthermore, Fonte [28] proposes a GLA algorithm with static output feedback. GLA systems that incorporates light detection and ranging (LIDAR) and disturbance model to predict the upcoming turbulence have been introduced by Giesseler et al. [32] and Fezans et al. [26]. Alam [2] shows a comparison of several feedback controllers to alleviate gust loads on a blended-wing-body configuration. An adaptive feed-forward GLA with the angle of attack as input has been introduced by Zhao et al. [106]. For wind tunnel experiments, Cheung et al. [11] developed folding wingtip devices to alleviate gust loads. Concerning the structural

resizing, the research elaborated by Wildschek et al. [100] shows for a blended-wing-body airliner that a reduction of the structural weight by approx. 2000 kg or 0.5% of the maximum take-off weight can be achieved with a feed-forward GLA.

Beside the control laws, Moulin et al. [63] and Pusch et al. [75] performed studies concerning the control surface concepts and layouts to alleviate gust loads. Furthermore, Kaiser [50] investigated alternative concepts of aileron architectures. Beside using classical control surfaces, load alleviation concepts with active winglets [101] or hinged wingtips [11,102] have been proposed with promising potentials of weight saving.

Fatigue analysis

Fatigue problems on airframes became a significant aspect during the 1950's and 1960's as the cruise altitude of passenger aircraft increased and with it also the pressure difference between the cabin and atmosphere. As stated by Payne [70], considerable loading conditions, that are relevant for fatigue, are ground-air-ground cycles, maneuver and turbulence loads. For fatigue calculations, standardized load spectra such as the TWIST spectrum [49] are commonly used.

On the experimental side, tests ranging from specimen fatigue experiments, e.g. described by Mayer et al. [60], to full-scale tests, as described by Grover [33], have been carried out. While specimen tests can provide an overview of the scatter in the fatigue life, full-scale tests provide findings of fatigue behavior of particular structures. For composites, among others Tan et al. [90] carried out fatigue tests and elaborates the effect of joints on the fatigue behavior.

For damage accumulation, Miner developed a method known as the Palmgren-Miner's rule [61]. Further fatigue prediction methods based on Palmgren-Miner's rule have been developed, e.g. in the method proposed by Schön et al. [86] with focus on spectral loading of composites. The Federal Aviation Administration (FAA) described a fatigue prediction method for composites using life- and load-enhancement factors as guidelines [22]. These factors are intended to take the scatter in the fatigue behavior of composites into account.

In connection with loads, Paletta [69] shows the contribution of load alleviation systems in extending the fatigue life on an aircraft. For that aim, ground-air-ground cycles, in-flight maneuvers and discrete gusts are considered.

1.3 Derivation of contribution

According to the state of the art, the majority of the referred publications investigates the influence of load alleviation on loads only. In the industry, dynamic gust and turbulence loads are typically investigated in the detail design phase. This thesis addresses those aspects for the preliminary design to gain insight into the influence of load alleviation in an earlier stage, where potential design changes are more cost-efficient. Beyond that, the following dissertations investigate the impact of load alleviation on the structural mass, fatigue or analysis of both gust and turbulence loads:

- Xu [105] proposes an aircraft conceptual design process with load alleviation and aircraft optimization. The latter also comprises variations of aircraft geometry along with structural optimization. As a result, differences in structural masses and load case hierarchy emerge, where the aircraft with load alleviation (active aircraft) is lighter than the passive counterpart. Furthermore, the operating costs between the respective aircraft are compared.
- Paletta [69] shows the influence of load alleviation on the loads and fatigue life of a business jet aircraft. In doing so, a reference ground-air-ground cycle, maneuvers, as well as discrete gusts based on the Pratt formula [74] during several flight phases are considered in the fatigue calculation. The conclusion is that load alleviation can extend the fatigue life of the reference aircraft.
- Teufel [92] elaborates the effect of load alleviation on gust and turbulence loads. Analogous to Paletta [69], the gust loads of the active aircraft tend to be lower compared to the passive aircraft. Furthermore, Teufel considers the effects of 2D turbulence on the loads.

From the dissertations mentioned above, however, the chain of impact of load alleviation ranging from design loads, structural mass to fatigue has not been addressed. Hence, the contribution of this thesis is to develop a method/process that considers:

Load alleviation in aircraft pre-design and its influence on design loads, structural mass and fatigue.

The term “load alleviation in aircraft pre-design” implies that the aircraft geometry is frozen, only the available control surfaces should be used for load alleviation, but the properties of the primary structure still have to be determined. For the design loads, quasi-steady maneuvers and dynamic 1-cos gusts are considered. The influence on structural mass means that the structure is optimized iteratively according to the previously calculated design loads until the structural masses converge. By doing so, the active and passive aircraft (with and without load alleviation) are expected to have different structural properties and hence also different fatigue behaviors. To investigate this, a qualitative fatigue analysis is conducted. The analysis focuses on a reference ground-air-ground cycle and turbulence loads in selected flight phases. Furthermore, the entire method should be robust and computationally efficient.

Table 1.1 visualizes the positioning of the contribution of this thesis. The investigated influence of load alleviation on the various aspects listed in the columns are illustrated using block diagram symbols. The three mentioned dissertations by Xu, Paletta and Teufel – which have high correlations with this thesis – are featured as comparison. Furthermore, the general trends of aspects addressed in the publications mentioned in Section 1.2 are included in the illustration. As apparent, no publication considers the influence of load alleviation on all aspects listed in the columns simultaneously.

Beside the major aspect, this thesis addresses several minor points comprising:

- The analysis of a forward swept wing configuration as one of the reference aircraft. This includes the problem of unstable bending-torsion-coupling and a decrease of flight mechanic stability due its aeroelastic behavior.
- The consideration of elastic aircraft, unsteady aerodynamics, active control and continuous turbulence in the analyses.
- The investigation of a retrofit (see Section 8.3) of the passive aircraft with load alleviation instead of including it already in the design process.

Table 1.1. Positioning of the contribution of this thesis

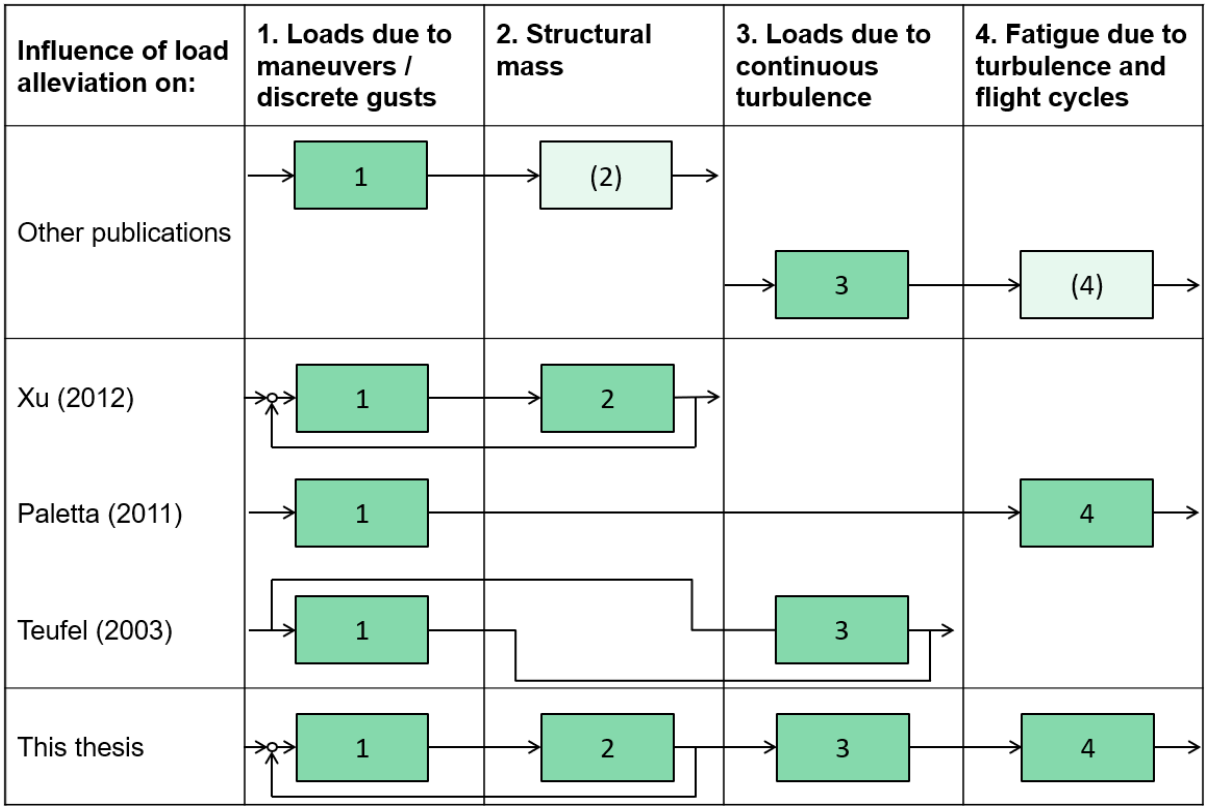

1.4 Dissertation layout

Chapter 2 introduces the two reference aircraft and elaborates their simulation models. The latter includes the structural, aerodynamic models of the aircraft, their coupling and the control surface models. For one reference aircraft, a model adaptation to enhance its flight mechanic stability is described. Chapter 3 addresses the design process featuring the methodology of the loads analysis and structural optimization applied in this thesis. The methodology part comprises the equations of motion used in the maneuver, gust and flutter simulations as well as a description of the structural optimization problem along with the constraints. Furthermore, the considered aeroelastic constraints are explained. An overview of the design process workflow is subsequently shown. Chapter 4 elaborates the load alleviation

applied in this thesis. At first, the considerations and restrictions for the load alleviation algorithm are listed. Then, the control algorithm for the maneuver and feed-forward gust load alleviation is derived. For the gust load alleviation, constraints are considered such as a maximum control surface deflection rate and the delay time representing the computing time of the flight control system. Moreover, the integration of the load alleviation into the design process is addressed. Chapter 5 deals with the methodology for turbulence and fatigue loads. It begins with a selection of the reference flight missions for the reference aircraft. This is followed by an approach to simulate turbulence loads emerging in the reference flight missions. Loads due to ground-air-ground cycles are also taken into account since these are seen to be relevant for the fatigue life of the aircraft. To estimate the fatigue life, methods to calculate the fatigue damage based on the obtained loads are elaborated. Chapter 6 and 7 contain an overview of the simulation parameters, the calculation results of each reference aircraft – with and without load alleviation – and their discussions. The first part of the results comprises the design loads, structural masses and aeroelastic parameters of the reference aircraft. The second part of the results deals with the reference flight missions, the emerging loads collectives as well as the resulting fatigue damage. Further practical aspects are investigated in Chapter 8. The investigations cover several variations of the load alleviation algorithm and their effects on the design loads or fatigue life. As the final part, Chapter 9 elaborates the evaluations, conclusions and outlook of this work.

2 Reference aircraft and their aeroservoelastic modeling

For the investigations concerning the load alleviation, structural masses and fatigue mentioned in Section 1.3, reference aircraft have to be selected and their models have to be generated first. This chapter starts with a brief explanation about why the two mid-range commercial aircraft are taken as reference for the investigations. A description of each reference aircraft with an overview of selected parameters follows. Subsequently, the structural and mass modeling as well as the respective model generation aspects are explained. Furthermore, the aerodynamic theories behind the aeroelastic analyses are described. The last section in this chapter describes the structural and aerodynamic modeling of control surfaces. Since the number of load cases considered in the analyses – including dynamic simulations – is expected to be high (>100), the priority in the aircraft modeling lies in minimizing the computing time.

2.1 Reference aircraft

Two reference aircraft are investigated: the backward swept D150 configuration and the forward swept ALLEGRA configuration. The D150 configuration is similar to the Airbus A320, a typical mid-range commercial aircraft with a conventional configuration. The term conventional configuration represents a backward swept wing, engines mounted under the wing and fuselage mounted empennage. Among Airbus aircraft, the A320 family has the highest number of aircraft in operation [1], which underlines its significance for commercial aviation.

The ALLEGRA configuration is selected as the second reference aircraft. The configuration was studied for future mid-range aircraft. Its parameters such as payload, operating Mach number and design masses are similar to the D150 configuration. ALLEGRA has an unconventional forward swept wing and T-tail configuration. These aspects are expected to evoke aeroelastic effects that are not observable on the D150 configuration. One of such effects is the increase of the lift slope at high dynamic pressures caused by the bending-torsion coupling of the forward swept wing. This effect is elaborated further in Section 2.5.

D150 configuration

D150 is a mid-range transport aircraft configuration with an aluminum structure. It is designed for 150 passengers and originates from the DLR project VAMP (Virtual Aircraft Multi-disciplinary Analysis and Design Processes, 2010-2012) [107]. The aircraft geometry and data are based on the CPACS data set from the DLR project iLOADS (2013-2016) [57,58]. Figure 2.1 shows the geometry of the D150 configuration in cyan. The FE model of the engine cowling generated using the DLR in-house program ModGen [53] is visualized in yellow. Table 2.1 lists the aircraft's key parameters. Since the design of the D150 configuration originates from a process on a conceptual level, the wing twist distribution along the span is constant at 2° (leading edge up).

Table 2.1. Key parameters of the D150 configuration

Parameter	Value
Wing surface	122.3 m²
Wingspan	33.91 m
Mean aerodynamic chord	4.19 m
Wing aspect ratio	9.4
Wing taper ratio	0.246
Sweep angle of 25% chord line	24.94°
Operating empty mass (OEM)	40638 kg
Maximum zero fuel mass (MZFM)	60562 kg
Maximum landing mass (MLM)	62959 kg
Maximum take-off mass (MTOM)	72545 kg
Design cruise speed, Mach number	180 m/s CAS, Mach 0.82
Design dive speed, Mach number	205 m/s CAS, Mach 0.89
Service ceiling	13000 m

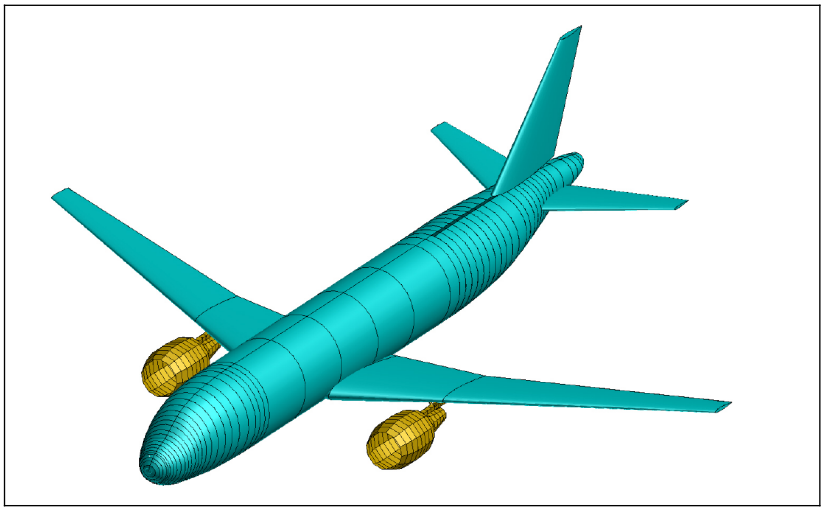

Figure 2.1. Geometry of the D150 configuration

The wing of the D150 configuration is made of aluminum alloy Al2024. Table 2.2 lists the material properties.

Table 2.2. Material properties of D150 wing structure

Material parameter	Value
Tensile modulus E	73.8 GPa
Ultimate strength σ_{ult}	441 MPa
Poisson number ν	0.33
Mass density ρ	2800 kg/m³

ALLEGRA configuration

ALLEGRA is a mid-range transport aircraft configuration for 150 passengers which was investigated in the DLR project ALLEGRA (AeroeLastic stability and Loads prediction for Enhanced GReen Aircraft, 2012-2016) [59]. Its distinguishing features are the forward swept wing that enables natural laminar flow at a cruise Mach number of 0.78 [88] and the T-tail. The design originates from the DLR project LamAiR (Laminar Aircraft Research, 2009-2012). Its structure is made of composite materials [88]. Figure 2.2 shows the geometry of the ALLEGRA configuration. Table 2.3 lists key aircraft parameters. Moreover, Figure 2.3 visualizes the twist distribution $\delta(y)$ of the jig shape. The flight shape twist distribution is a result of an optimization for natural laminar flow (NLF) using CFD. Its jig-shape is derived from the flight shape using the structural stiffness and the design lift distribution [104].

Table 2.3. Key parameters of the ALLEGRA configuration

Parameter	**Value**
Wing surface	132.0 m²
Wingspan	35.81 m
Mean aerodynamic chord	4.01 m
Wing aspect ratio	9.7
Wing taper ratio	0.3
Sweep angle of 25% chord line	-19.6°
Operating empty mass (OEM)	43712 kg
Maximum zero fuel mass (MZFM)	62962 kg
Maximum landing mass (MLM)	65949 kg
Maximum take-off mass (MTOM)	73365 kg
Design cruise speed, Mach number	180 m/s CAS, Mach 0.80
Design dive speed, Mach number	203 m/s CAS, Mach 0.87
Service ceiling	12500 m

For the structure of the lifting surfaces of the ALLEGRA configuration, Carbon-Epoxy (IM6) [44] is used. The ply angle distributions are set to predefined values, each for the skins, spars and ribs. With this approach, the structure is optimized by varying the material thicknesses only, analogous to the aluminum D150 configuration. Aeroelastic tailoring can indeed be considered in the structural optimization of the composite wing [44]. However, since it is not the main focus in this work and requires significantly longer computing times, it is not taken into account.

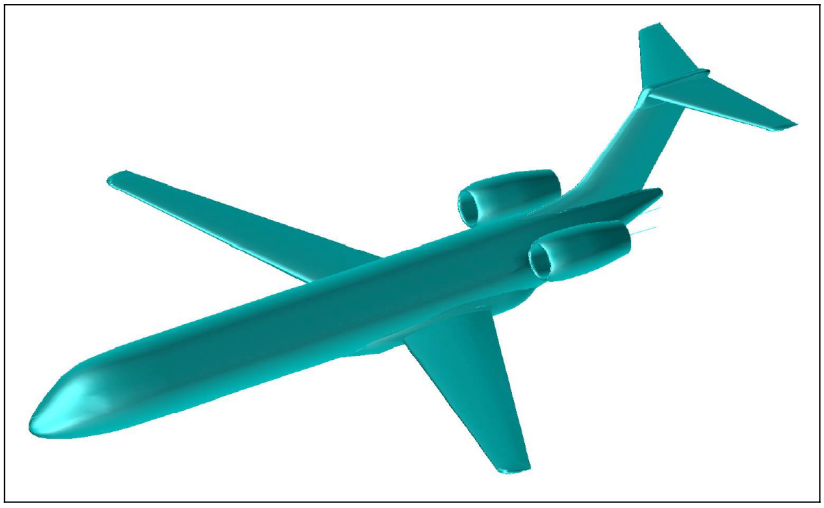

Figure 2.2. Geometry of the ALLEGRA configuration

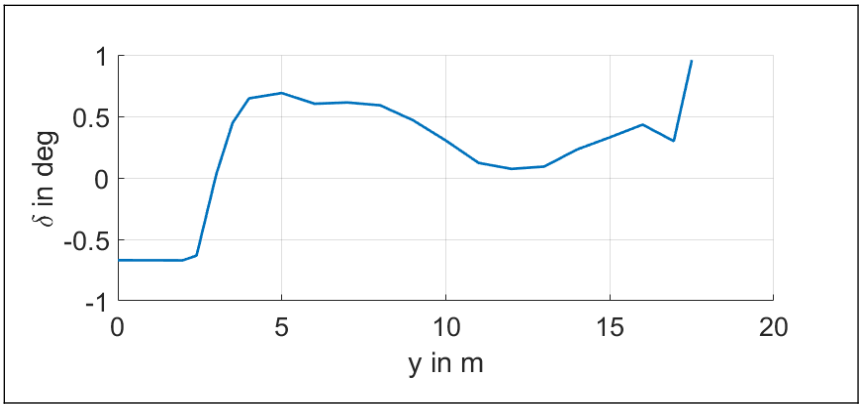

Figure 2.3. Jig shape twist distribution of the ALLEGRA configuration

Table 2.4 shows the material properties of the ALLEGRA wing structure.

Table 2.4. Material properties of carbon-epoxy IM6 composite [44]

Material parameter	**Value**
Longitudinal modulus E_{11}	177 GPa
Transverse modulus E_{22}	10.8 GPa
Shear modulus G_{12}	7.6 GPa
Poisson number ν	0.27
Mass density ρ	1578 kg/m³

Table 2.5 lists the ply angle distributions for the different parts of the wing structure. With these ply angle distributions, the skins have a relatively large stiffness in spanwise direction. Hence, they can absorb the majority of bending moments, particularly because they have a large second moment of area in the bending axis. The spars have a relatively high shear stiffness to absorb the majority of vertical shear forces and torsion moments. Furthermore, the shear stiffness on the ribs is supposed to provide wing box stability.

Table 2.5: Ply angle distributions on ALLEGRA wing structure

Component	0° plies	±45° plies	90° plies
Skins	50%	40%	10%
Spars	10%	80%	10%
Ribs	10%	40%	50%

2.2 Structural and mass models

For the loads analysis and structural optimization, MSC.Nastran models of the reference aircraft generated with the DLR in-house MONA process [53] are used. The primary structure on the lifting surfaces is modeled with shell elements for the spars, skins and ribs, as well as with bar elements for the stiffeners. The fuselage is modeled with beam elements. Furthermore, the engine pylons are modeled using bar elements, and the engine masses are attached to the respective center of gravity positions. In the MONA process, the finite element (FE) models undergo a preliminary structural sizing using analytic-empirical methods [54]. Figure 2.4 shows the FE model of the D150 configuration, while the shell elements of the fuselage and engines are represented for illustration purpose only. In addition, nodes at the leading and trailing edge of the lifting surfaces are visualized.

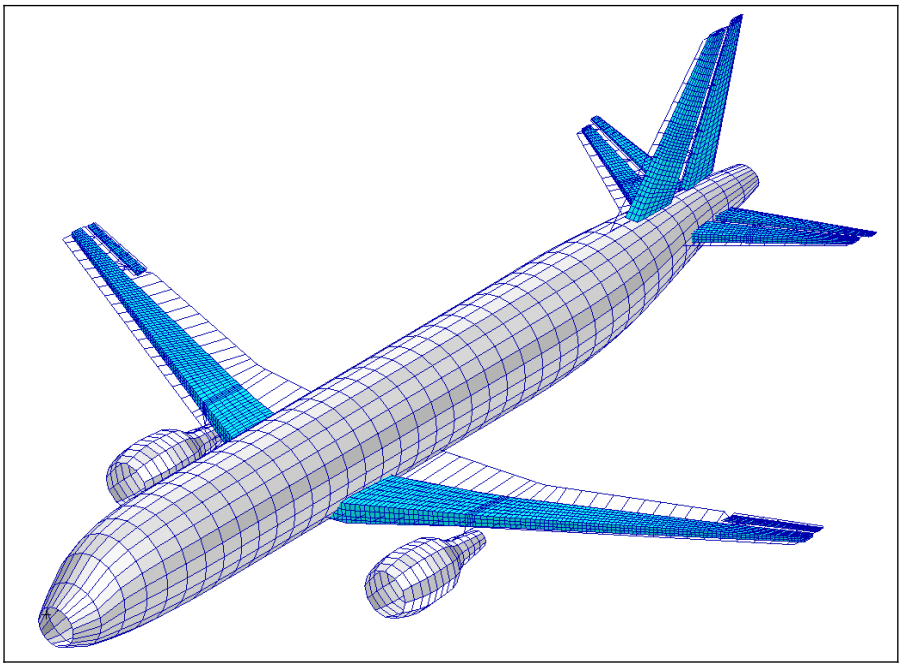

Figure 2.4. Full FE model of the D150 configuration

The total mass of both aircraft models consists of structural masses, secondary masses, systems, fuel modeled according to Klimmek [54] and payload. To resemble realistic load distributions due to fuel masses, the defueling sequence is set to: center tank – inner tank – outer tank, and the fueling sequence is set to: outer tank – inner tank – center tank. The latter is considered when distributing a defined fuel total mass into the fuel tanks. Moreover, this sequence reduces the wing bending moment since fuel mass placed far from the symmetry

plane creates a larger relieving bending moment compared to fuel mass near the symmetry plane. Figure 2.5 illustrates the division of the wing fuel tanks with exemplary, arbitrary fuel levels.

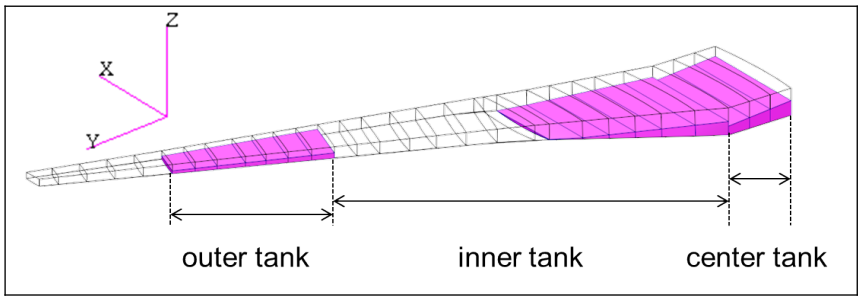

Figure 2.5. Fuel tank division on the D150 configuration

For the payload, masses are distributed over the fuselage to meet the target total masses and center of gravity (CG) positions. To evoke the highest loads resulting from high moment of inertia, the masses are placed as near as possible to the first seat row or the last seat row, see Figure 2.6. At the same time, each fuselage node should carry no more than 1200 kg of payload to avoid having excessively high concentrated masses. This would correspond with a seat row with six passengers weighing 100 kg each (including luggage), combined with a cargo mass of 600 kg.

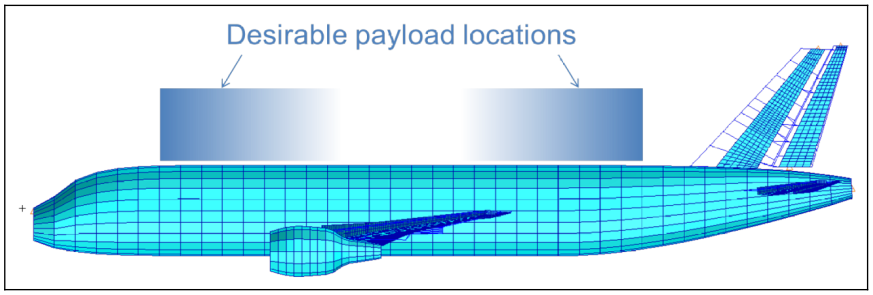

Figure 2.6. Desirable payload locations on the D150 configuration

Table 2.6 gives an overview of the number of elements of the full FE models. It is apparent that the ALLEGRA configuration has significantly more bar elements than the D150 configuration. This is because the D150 only has five stringers along the wing box chord with a variable stringer pitch. In the D150 model generation, the total stringer area is distributed into the five stringers of the FE model. In contrast, the ALLEGRA configuration has a fixed stringer pitch with a variable number of stringers along the wing box chord. This results in larger numbers of stringers – up to 15 around the root. Figure 2.7 shows a cut FE model of the starboard wing box where the bar elements of the stringers on the skins as well as stiffeners on the spars and ribs are visible.

Table 2.6: Overview of the number of elements of the full FE models

Aircraft	Grids	Shell elements	Bar elements
D150	10800	11000	5400
ALLEGRA	13000	13700	14100

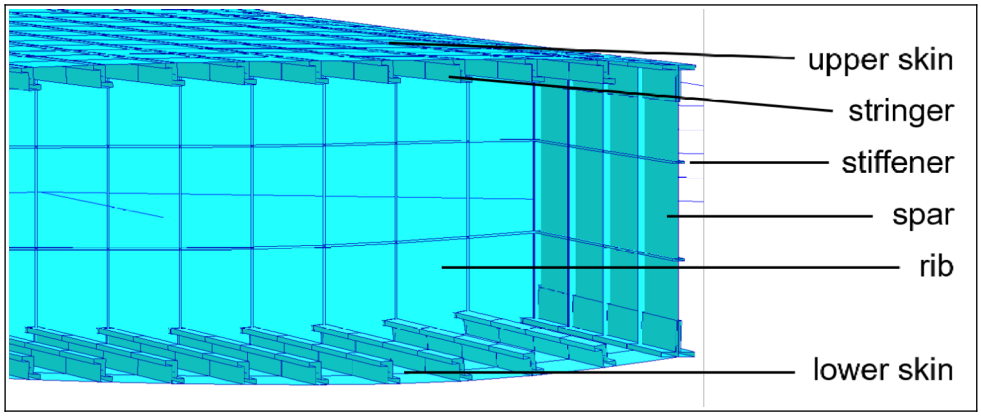

Figure 2.7. View into the wing box of the ALLEGRA configuration

To reduce computing time in the loads analysis, the stiffness and mass properties of the reference aircraft are condensed onto the load reference axis (LRA) nodes. Figure 2.8 shows those nodes using the orange triangle markers. Besides, the condensed models have dependent nodes at the leading and trailing edge of the lifting surfaces which are used for the spline of the aerodynamic forces. Those nodes are connected to the LRA nodes with rigid body elements. In total, the FE model of the D150 configuration has 261 LRA nodes and the ALLEGRA configuration has 214 LRA nodes.

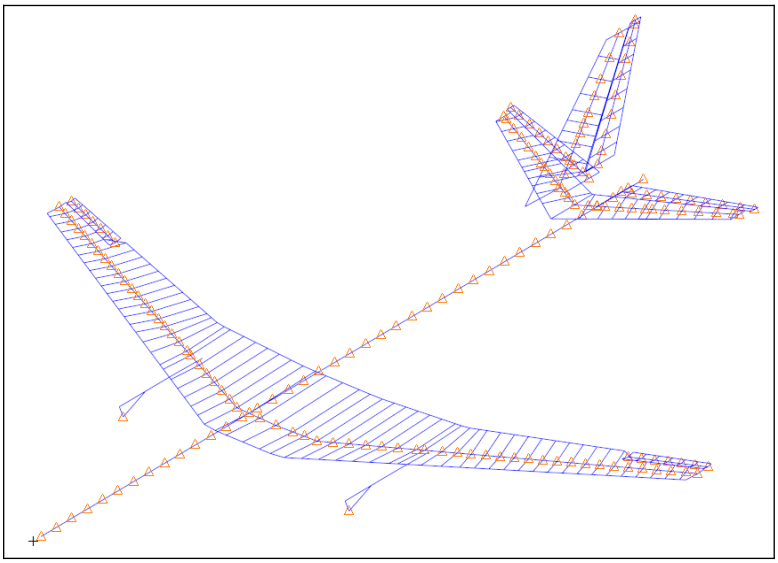

Figure 2.8. Condensed stiffness and mass model of the D150 configuration

2.3 Aerodynamic models

The aerodynamic forces are modeled using the doublet lattice method (DLM) which is based on the potential theory. DLM is introduced by Albano et al. [3], implemented in MSC.Nastran [64] and a fast method to calculate motion-induced aerodynamic forces in the subsonic regime. In DLM, the lifting surfaces are assumed as thin plates and divided into trapezoidal lifting elements (boxes), while the lateral edges are parallel to the free stream, see Figure 2.9.

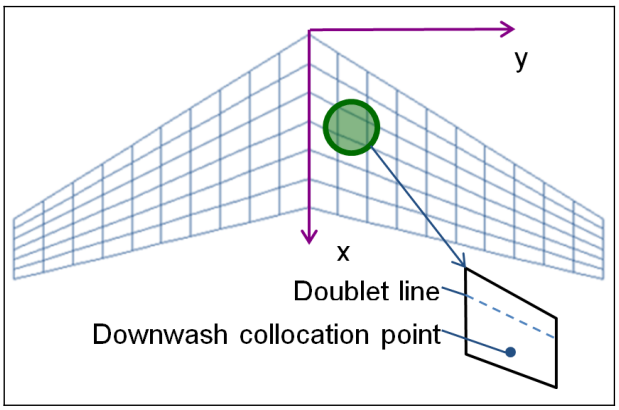

Figure 2.9. Lifting surface discretization in DLM

The pressure difference Δc_p between the upper and lower side is modeled with a potential doublet at the 25% chord line on each box. In a steady flow condition, this corresponds to a horseshoe vortex where the bound segment coincides with the 25% chord line of the box. The evaluation of the downwash w induced by the doublets is done at the collocation point that is located at mid-span and 75% chord of each box [3].

Since the downwash velocity w is also influenced by vortices of neighboring boxes, the influence coefficients of the vortices are written in an aerodynamic influence coefficient (AIC) matrix A as defined by:

$$\{w\} = [A\,(Ma, k)]\,\{\Delta c_p\}, \tag{2.1}$$

with:

$$k = \frac{2\pi f \cdot \bar{c}}{2V_{TAS}}, \tag{2.2}$$

and:

Ma : Mach number [-],
k : reduced frequency [-],
f : frequency [Hz],
$\bar{c}$: mean aerodynamic chord [m],
V_{TAS} : true airspeed [m/s].

The downwash velocity is bound to the condition that the flow at the collocation points must be tangential to the oscillating lifting surface as:

$$\{w\} = [\mathrm{real}(D_a) + ik \cdot \mathrm{imag}(D_a)]\,\{u_a\} + \{w_s\}, \tag{2.3}$$

with:

i : imaginary number [-],
k : reduced frequency [-],
D_a : differentiation matrix [1/s],
u_a : displacements of aerodynamic grid points [m],
w_s : static aerodynamic downwash velocity from angle of attack, camber or twist [m/s].

Since the aerodynamic forces can only be calculated for harmonic motions, they are known in the frequency domain. For investigations in the time domain, an inverse Fourier transform is necessary [3]. The upper frequency limit f_{max}, at which the calculation results are considered as reliable, correlates with the discretization of the DLM boxes and the airspeed [66]. According to the MSC.Nastran documentations [64,66], the aspect ratio of the DLM boxes should be less than three and the chord length should satisfy:

$$\bar{c}_{box} < 0.08 \frac{V_{TAS,min}}{f_{max}}, \tag{2.4}$$

with:

$$\bar{c} = \bar{c}_{box} \cdot n_{box}, \tag{2.5}$$

and:

$\bar{c}_{box}$: typical chord length of aerodynamic box [m],
$V_{TAS,min}$: lowest true airspeed in the analysis [m/s],
f_{max} : highest frequency to be analyzed [Hz],
n_{box} : number of boxes in chordwise direction [-].

On the D150 configuration, the upper frequency limit f_{max} is 41 Hz, and on the ALLEGRA configuration it is 37 Hz. With 12 boxes in the chordwise direction, Equation (2.2), (2.4) and (2.5) yield a maximum observable reduced frequency k_{max} of 3.0.

To consider the aerodynamic effect of the fuselage, the subsonic wing-body interference theory is used [31,65]. For that purpose, a slender body element (see Figure 2.10) and a set of interfering lifting surfaces (see Figure 2.11) are defined. The interfering lifting surfaces circumscribe the slender body and consists of DLM boxes. The wing-body interference is approximated by the doublets on the interfering lifting surfaces μ_I. The slender body element itself implements a line of doublets along its longitudinal axis μ_s. With the boundary condition of no flow through the body, the doublet strength distribution can be determined. The downwash Equation (2.1) is then extended to:

$$\begin{Bmatrix} w_w \\ 0 \\ w_s \end{Bmatrix} = \begin{bmatrix} A_{ww} & A_{wI} & A_{ws} \\ A_{Iw} & A_{II} & A_{Is} \\ 0 & 0 & A_{ss} \end{bmatrix} \begin{Bmatrix} \Delta c_p \\ \mu_I \\ \mu_s \end{Bmatrix}, \tag{2.6}$$

with:

w_w : aerodynamic box downwash at 75% chord,
w_s : downwash on slender body element,
A : aerodynamic influence coefficient,

Δc_p : pressure coefficient on aerodynamic box,
μ_I : acceleration potential interference doublet,
μ_s : acceleration potential slender element doublet.

To consider the aerodynamic effects due to the twist and camber of the wing, a downwash correction with W2GJ matrix [54,64] created using ModGen is implemented. The W2GJ matrix practically describes the incidence angle of each aerodynamic element. The entries correspond to the slope of the respective camber line at the box position. Hence, the entries for a symmetric profile are zero. Furthermore, for transonic flow conditions, a correction of the AIC matrices can be taken into account, for example using data from CFD [36]. For this purpose, prior CFD calculations are necessary. However, CFD grids are not always available in the early stages of the aircraft design process, so that CFD based corrections are not always possible.

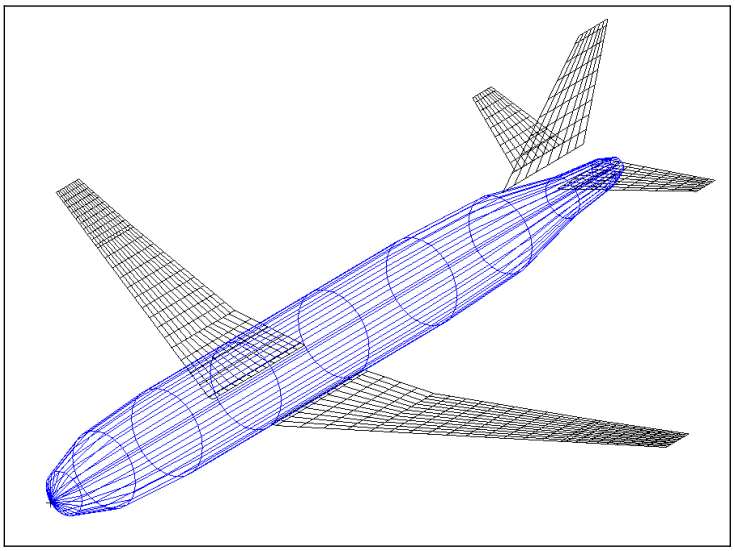

Figure 2.10. Aerodynamic model of the D150 configuration with slender body element

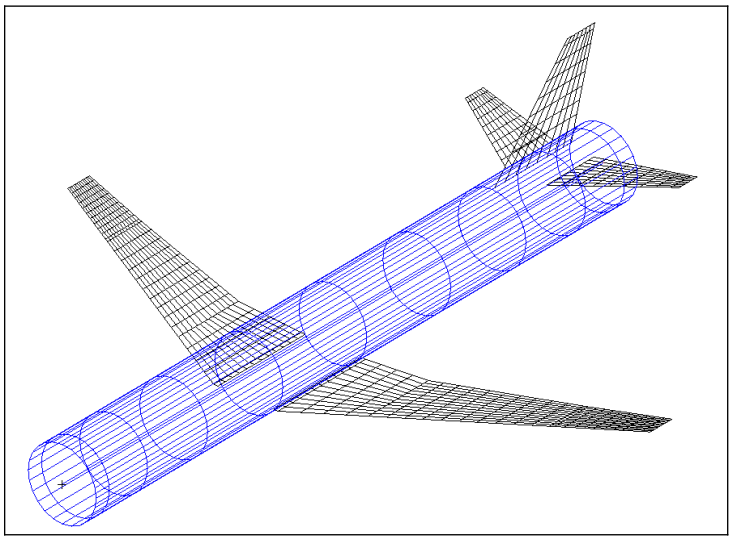

Figure 2.11. Aerodynamic model of the D150 configuration with interference body

For the next step, a coupling between the aerodynamics and the structure is necessary. This is done by introducing a dimensionless coupling matrix G_{kg}:

$$\{u_k\} = [G_{kg}]\,\{u_g\}, \tag{2.7}$$

with:

u_k : deflection of aerodynamic grid points,

u_g : displacement of structural nodes.

For the structural forces, the coupling is done with the transposed matrix:

$$\{P_g\} = [G_{kg}]^T\,\{F_k\}, \tag{2.8}$$

with:

P_g : forces on structural nodes,

G_{kg} : coupling matrix,

F_k : aerodynamic forces.

For the lifting surfaces, the surface spline method is used. In this case, the aerodynamic forces are splined onto the LRA nodes and their dependent nodes at the leading and trailing edges. On the fuselage, the aerodynamic forces are mapped onto the LRA nodes using a beam spline method. The spline for each lifting surface and slender body is carried out separately to avoid having aerodynamic forces on one component being mapped onto an adjacent one.

In total, the aerodynamic model of the D150 configuration has 939 aerodynamic elements and the ALLEGRA configuration has 1176 elements.

2.4 Structural and aerodynamic modeling of control surfaces

To implement the load alleviation functions, the control surface structures – in this case the ailerons, elevators and rudder – are modeled. For the aerodynamic part, the corresponding DLM boxes are assigned to the control surface and a local coordinate system for the orientation of the deflection is defined. Besides, an aerodynamic effectiveness of 0.7 is assumed to take disturbances due to the sudden contour change at the control surface hinge [84] and the vortices at the lateral edges into account. The aerodynamic effectiveness modifies the theoretical forces of an ideal control surface by the set value.

To model the dynamics of the control surface as well, a structural and a mass model are necessary. Hence, an FE model of each control surface is created with ModGen which is one of the main programs used in the MONA process [53]. Analogous to the wing structure, the control surface model consists of a front and rear spar, upper and lower skin, ribs and stiffeners. The skin thickness is adjusted so that the control surface mass matches the estimation by Torenbeek [94] which refers to the mass per control surface area.

The control surface hinge connection is modeled using massless, stiff connector bars. For that aim, several hinge nodes along the hinge line are defined. At the hinge points where an actuator is located nearby, the hinge nodes are connected to the wing, horizontal tailplane (HTP) or vertical tailplane (VTP) box with four bars each. Every other hinge node is

connected to the primary structure with two bars. On the control surface side, the aileron, elevator and rudder structure is connected to each hinge node using two bars. Figure 2.12 shows an FE model of an aileron. The thick blue lines represent the massless bars for the hinge modeling, and the dashed/dotted green line visualizes the hinge line. Moreover, a hinge spring is also visible. The spring is defined to avoid a stiffness singularity of the control surface, and its stiffness is set to 1 Nm/rad. In simulations where the control surface should remain at the neutral position, the spring stiffness is increased to 10^7 Nm/rad. Figure 2.13 shows a principal sketch of the hinge.

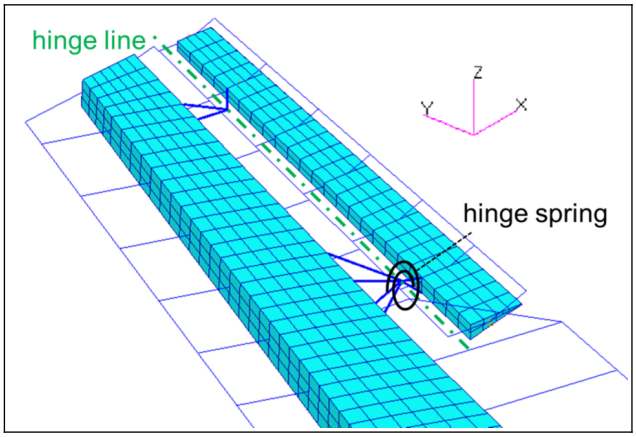

Figure 2.12. Structural modeling of an aileron and its hinge

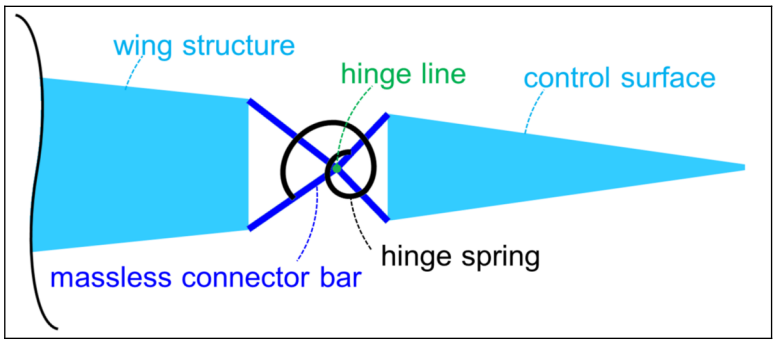

Figure 2.13. Principal sketch of a control surface hinge

2.5 Model adaptation – ALLEGRA configuration

Background

According to Wunderlich [104], the aeroelastic effects of the LamAiR configuration – the base of the ALLEGRA configuration – are not considered in its conceptual design. However, the aeroelasticity of aircraft wings can change the wing lift slope and even shift the aerodynamic center of the whole aircraft. The latter is a crucial aspect since the longitudinal stability of the aircraft may be affected in a negative way.

On the forward swept ALLEGRA configuration, the lift slope of the elastic aircraft becomes larger with increasing dynamic pressure. This is caused by the following points:

- An increase in angle of attack causes more lift and the wing tip bends up.
- Due to the forward sweep and its bending-torsion-coupling, the wing tip's upward bending causes a nose-up twist.
- This nose-up twist amplifies the local angle of attack and with it the local lift, especially at the wingtip.
- Due to the local lift amplification, the lift slope is larger compared to the rigid aircraft.

Figure 2.14 illustrates the wing twist caused by the bending-torsion-coupling.

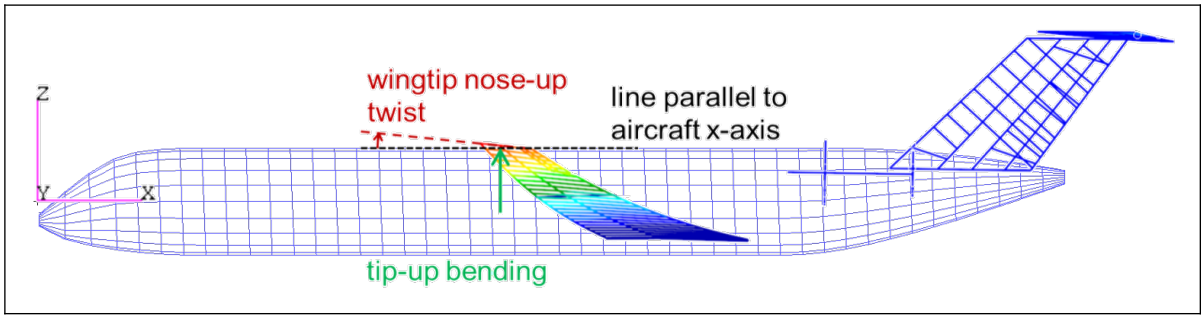

Figure 2.14. Wing twist due to bending-torsion-coupling

The wingtip is the most affected area by the bending-torsion-coupling. It lies further forward compared to the 25% chord line of MAC, see Figure 2.15. Since the 25% chord line of MAC represents the aerodynamic center of the rigid aircraft, the wingtip twist and the amplified local lift on the elastic aircraft result in a forward shift of the aerodynamic center.

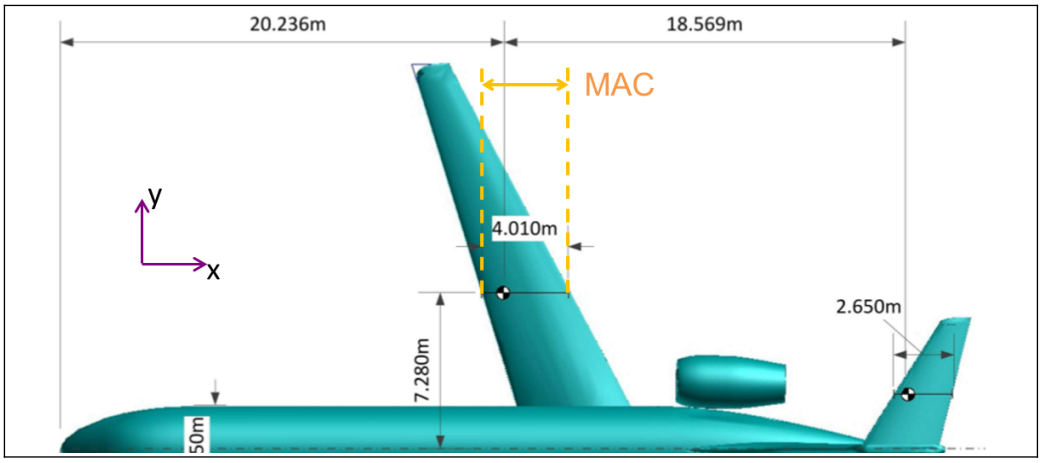

Figure 2.15. Wingtip position relative to MAC

Challenge

On the initial model with IM6 composite, the shift of the aerodynamic center in flight was so large that the aircraft became unstable in the pitch axis. To solve this problem, the rear CG limit was moved forward from 40% to 35% MAC, and the wing skin laminate orientation was rotated to reduce the wingtip twist and also the shift of the aerodynamic center. Figure 2.16 visualizes the laminate rotation and Figure 2.17 shows its effects, among others on the location of the aerodynamic center.

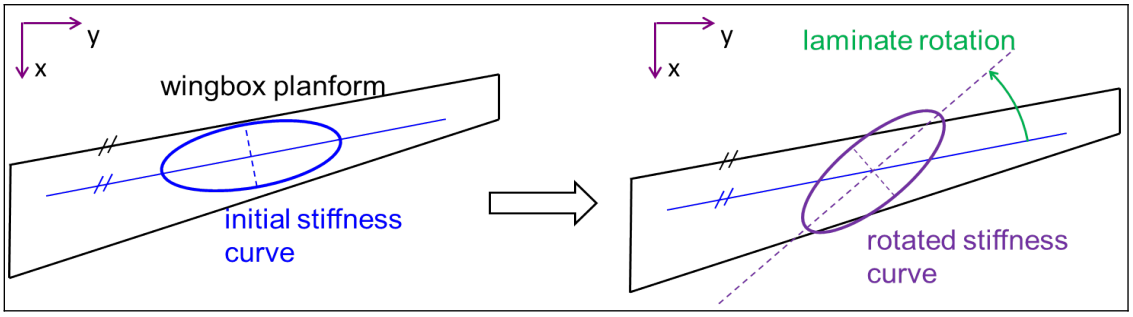

Figure 2.16. Rotation of skin laminate orientation

Reference load case

The trim condition at the design dive speed V_D/M_D as described in Table 2.7 is taken as reference. This trim condition is chosen because it provides the combination of the highest design dynamic pressure and the highest design Mach number, and this maximizes the magnitude of the aeroelastic effects. The trim calculation is conducted using MSC.Nastran as described in Section 3.1.

Table 2.7. Reference trim condition for laminate rotation study

Parameter	Value
Altitude	7010 m
Airspeed	271.6 m/s TAS (Mach 0.87)
Load factor	2.5

Results and discussion

In this investigation, only the laminate rotation and the subsequent reference trim calculation is carried out; no further structural optimization is conducted for the various laminate rotation angles. The reference wing stiffness distribution is taken from the optimized passive aircraft according to Chapter 7 with 30° laminate rotation.

In principle, the laminate rotation – about the positive z-axis of the aircraft – couples the tip-up wing bending with a nose-down twist. On one hand, this can compensate the nose-up twist due to the bending-torsion-coupling by up to 75%, as can be seen in Figure 2.17(a). On the other hand, the wing bending stiffness decreases since a fraction of it is transformed into the coupling stiffness between bending and torsion. This is reflected by the increasing wingtip deflections in z-direction with larger laminate rotation angles in Figure 2.17(b). Hence, with a decreasing bending stiffness, the coupled nose-up twist becomes larger, and the compensation effect by rotating the laminate becomes less effective at a certain point, as can be seen in Figure 2.17(a) between the laminate rotation angles of 30° and 40°. A way to restore the bending stiffness and minimize the wingtip twist at high laminate rotation angles (>30°) is to increase the material thickness, and with it also the wing box mass.

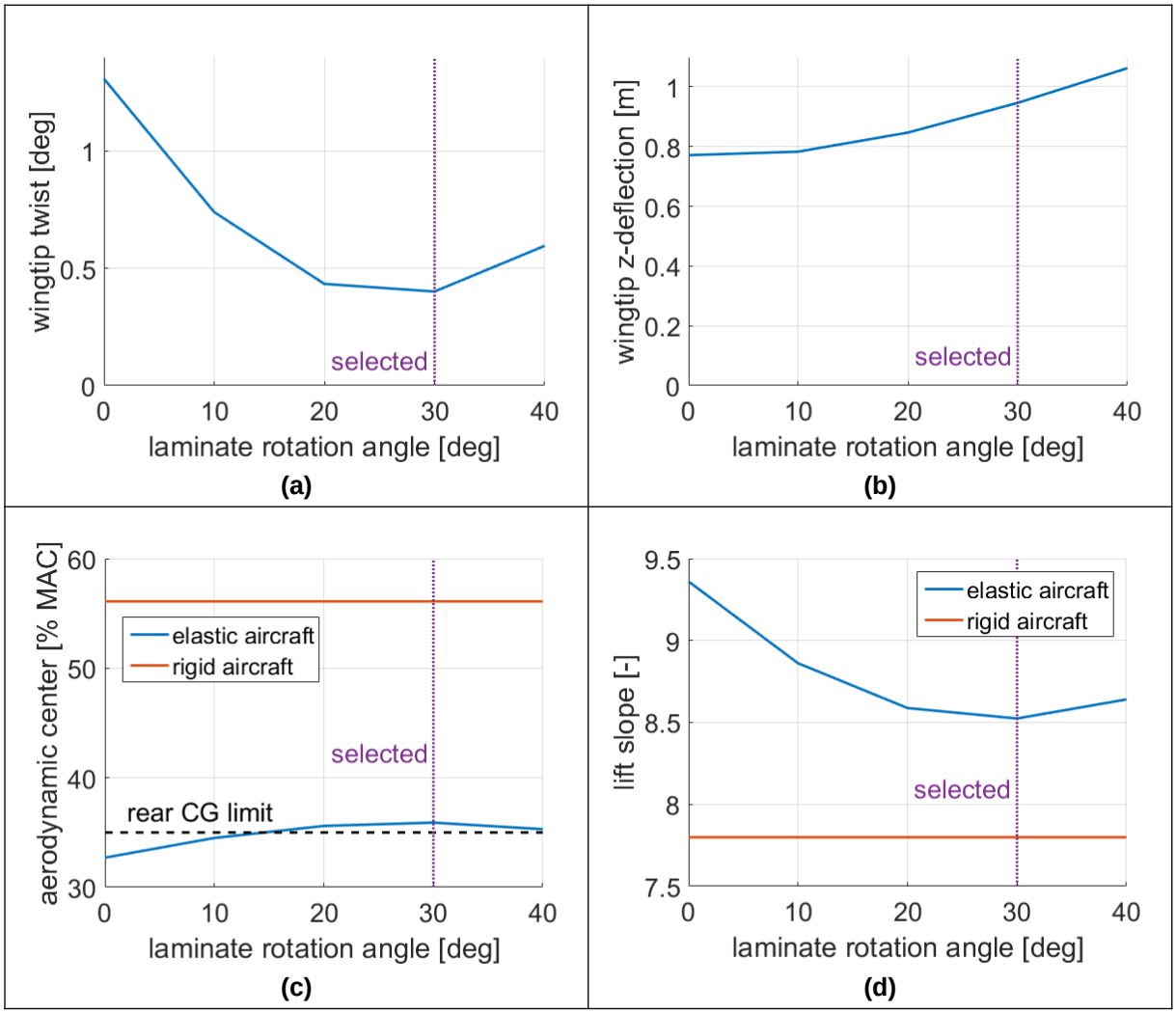

Figure 2.17. Rotation of laminate orientation and their effects on the trim

Trends similar to the wingtip twist in Figure 2.17(a) also appear in the graphs for the aerodynamic center and lift slope Figure 2.17(c) and (d) where a laminate rotation of 30° yields the smallest differences compared to the rigid aircraft. In Figure 2.17(d), the lift slope of the rigid aircraft is larger than 2π due to compressibility effects. To fulfill the stability requirement that the rear CG limit has to be in front of the aerodynamic center, a laminate rotation between 20° and 40° can be considered, as visible in Figure 2.17(c). Since a laminate rotation of 30° provides the largest stability margin, it is taken for the investigations in this thesis.

As a remark: with parameters in Table 2.7, the dynamic pressure is 21717 Pa. Since the shift of the aerodynamic center becomes larger with increasing dynamic pressure, the aircraft's stability margin is expected to become negative if the dynamic pressure is further increased.

As a comparison: On the elastic D150 configuration, the aerodynamic center at V_D/M_D is at 49.8% MAC, and the rear CG limit is at 45% MAC. Hence, the elastic aircraft stays stable at V_D/M_D.

3 Design process of loads analysis and structural optimization

The interdependency between loads and structural properties has to be considered during the optimization of elastic aircraft. However, the load calculation and the optimization of the structure cannot always be conducted simultaneously, especially when dynamic simulations are included. For this reason, an iterative design process – as it is commonly applied in the industry – is set up for the reference aircraft. Each iteration cycle consists of a loads analysis based on the DLR loads process as described by Krüger et al. [58] and a subsequent structural optimization with gradient-based algorithms.

To prepare for the loads and optimization process, load cases according to CS25 [20] are defined for the simulations. The load cases comprise symmetric maneuvers (+2.5g pull-ups and -1g push-downs) and vertical 1-cos gusts with gust gradients ranging from 9 m to 107 m.

The maneuver and gust simulations to obtain the loads are described in the Sections 3.1 and 3.2. The resulting loads are then post-processed to select load cases – among the thousands – that are relevant for the structural optimization. This post-processing is elaborated in Section 3.3 and the gradient-based structural optimization is described in Section 3.4. Beside the structural strength and stability criteria, aeroelastic constraints explained in Section 3.5 are also considered in the optimization. For the optimized models, a flutter calculation as elaborated in Section 3.6 is conducted to identify the flutter speed of the reference aircraft. Section 3.7 gives an overview of the whole loads analysis and structural optimization workflow including the interconnection between the modules.

3.1 Maneuver simulation

The maneuvers are simulated with SOL144 of MSC.Nastran [64] which is designed to perform quasi-steady aeroelastic analyses. The equations of motion solved in SOL144 are:

$$[K_{aa} - \bar{q}Q_{aa}]\{u_a\} + [M_{aa}]\{\ddot{u}_a\} = \bar{q}\,[Q_{ax}]\{u_x\} + \{P_a\}, \tag{3.1}$$

with:

K_{aa} : structural stiffness matrix,
$\bar{q}$: dynamic pressure,
Q_{aa}, Q_{ax} : aerodynamic stiffness matrices,
u_a : nodal displacements,
M_{aa} : structural mass matrix,
u_x : control and rigid body motion variables,
P_a : applied loads, including downwash from twist and camber corrections.

The equations of motion are solved in physical coordinates (thus the index a) and valid for a free flying aircraft. The control and rigid body motion variables in the equation can comprise:

- angle of attack α,
- slip angle β,
- angular velocities p, q, r,
- translational accelerations $\ddot{y}$, $\ddot{z}$,
- angular accelerations $\dot{p}$, $\dot{q}$, $\dot{r}$,
- control surface deflections η_{CS}.

To obtain an explicit solution, the equation system has to be determined. This means, the number of equations has to be equal to the number of unknown variables.

In this thesis, only symmetric maneuvers (pull-ups and push-downs) are considered; no roll and yaw maneuvers are taken into account. For the simulations, the prescribed vertical load factors n_z are +2.5 and -1.0 and the pitch rate q of the aircraft are considered [20]. In the simulation, all maneuvers are assumed as quasi-steady pull-ups and push-downs, and the pitch rate is calculated by:

$$q = \frac{(n_z - 1) \cdot g}{V_{TAS}}, \tag{3.2}$$

with:

g : gravitational acceleration [m/s²],
V_{TAS} : aircraft true airspeed [m/s].

3.2 Dynamic gust simulation

The gust simulations are performed with SOL146 of MSC.Nastran [64], that is designed for dynamic aeroelastic analyses in the frequency domain. The DLM elaborated in Section 2.3 is applied to compute the aerodynamic loads. The equations of motion in SOL146 are:

$$\left[-M_{hh}\omega^2 + iB_{hh}\omega + K_{hh} - \bar{q}Q_{hh}(Ma, k)\right] \{u_h\} = \{P_h(\omega)\}, \tag{3.3}$$

where:

M_{hh} : modal mass matrix,
ω : circular frequency,
B_{hh} : modal damping matrix,
K_{hh} : modal stiffness matrix,
$\bar{q}$: dynamic pressure,
Q_{hh} : aerodynamic matrix,
Ma : Mach number,
k : reduced frequency,
u_h : modal displacements,
P_h : generalized applied loads.

The differential equation system is solved in modal coordinates (thus the index h) to reduce the computing time. This is done for every frequency step. Since the aerodynamic matrix Q_{hh} can only be created for a small number of reduced frequencies due to its size, it is interpolated over the range of the observed circular frequency ω. For the damping matrix B_{hh}, a structural damping of 3% is set, as it can be assumed according to CS25 [20].

In the simulations, frequencies up to 50 Hz and AIC matrices with reduced frequencies up to 1.0 are considered. With the flight parameters of the reference aircraft, a reduced frequency of 1.0, as stated in Equation (2.2), is equivalent to a frequency of up to 20 Hz. This is seen as sufficient since more than 99% of the energy of 1-cos gusts is contained in frequencies up to twice of the gust base frequency f_g defined by:

$$f_g = \frac{V_{TAS}}{2 \cdot H}, \tag{3.4}$$

with:

f_g : gust base frequency [Hz],
V_{TAS} : aircraft true airspeed [m/s],
H : gust gradient [m].

Gust base frequencies, that are potentially relevant for the structural optimization, are expected to be close to the first wing bending frequency. For commercial transport aircraft, the first wing bending mode typically occurs between 1 Hz and 5 Hz, depending on the aircraft geometry and mass configuration. As a conclusion, AIC matrices that cover at least frequencies up to 10 Hz are seen as sufficient for the gust loads analysis.

To obtain the aircraft response to a particular 1-cos gust, the time history of the gust is introduced as the generalized applied loads P_h. Within MSC.Nastran, the time history is transformed into the frequency domain for further processing. In the output, the aircraft responses are given in the time domain again. For the active aircraft, control surface deflections during a gust encounter are inputted as enforced motions. In the equations of motion, the enforced motions are handled as generalized applied loads P_h. This procedure is applied for the design gust load calculations in this thesis.

To obtain the transfer functions, e.g. of the aircraft response to gusts or control surface deflections in general, the loads P_h are introduced as white noise or spectral gust excitation with a predefined amplitude in the frequency domain. The transfer function results are given in the frequency domain as well. This case is relevant for the turbulence analysis described in Section 5.3.

3.3 Loads post-processing for structural optimization

As gust simulations consist of several hundred time steps for every gust encounter, the number of load cases for the structural optimization – comprising all maneuvers and all time steps of every gust encounter – would be too high. In literature references, the typical number of load cases considered in the optimization is below 20, as listed by Bramsiepe et al. [4]. On a composite wing, Dillinger [16] included 13 load cases in the optimization and Klimmek [54] took 16 load cases on an aluminum wing into account. Hence, an algorithm to filter the relevant load cases is necessary. This algorithm is divided into two steps: the first one is to reduce the number of time steps extracted from each gust encounter, and the second one is to identify the load cases with the largest cut loads among all the maneuver and gust cases.

For that aim, monitoring stations for cut loads are defined on the wing and HTP, see Figure 3.1. At the positions of the green circles, the loads are monitored in the local coordinate system. In the gust simulations, those monitoring stations are used for the first step of filtering: when at least one of the monitoring stations reaches its maximum or minimum in shear force F_z, bending moment M_x or torsion moment M_y, all nodal loads at that time step are extracted [12]. Figure 3.2 illustrates this extraction using an exemplary load quantity.

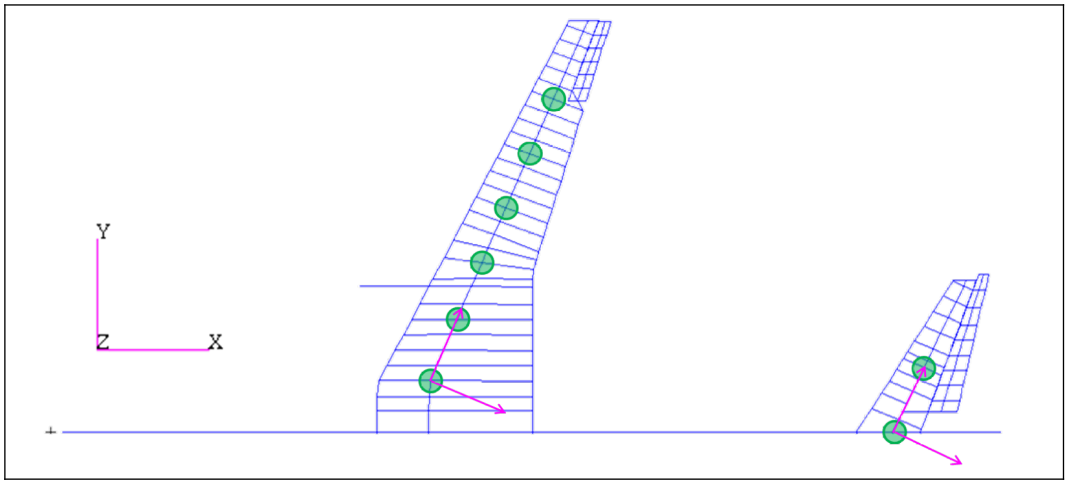

Figure 3.1. Monitoring stations on the D150 configuration

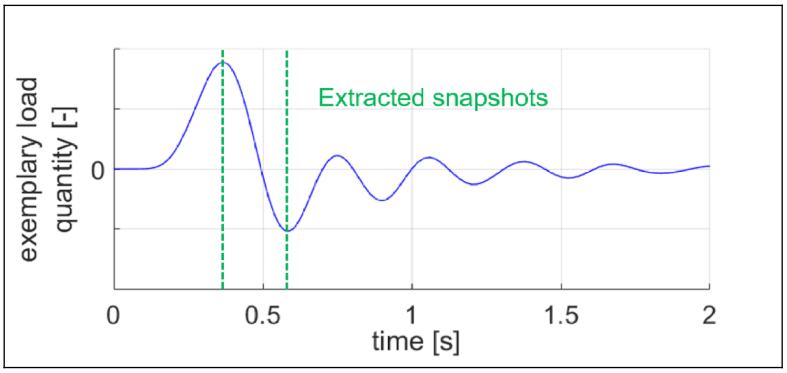

Figure 3.2. Extracted snapshots from a gust encounter

The gust simulations with SOL146 only yield the incremental gust loads acting on the aircraft. To obtain the total loads, the gust loads have to be superposed with the corresponding trim loads:

$$\{P_{total}\} = \{P_{trim}(\text{SOL144})\} + \{P_{gust}(\text{SOL146})\}. \tag{3.5}$$

The trim loads are calculated with SOL144 with a load factor of 1.0 and a pitching velocity of 0 rad/s. Figure 3.3 visualizes an exemplary superposition – in this case of the load factor – during a gust encounter in a V-n diagram.

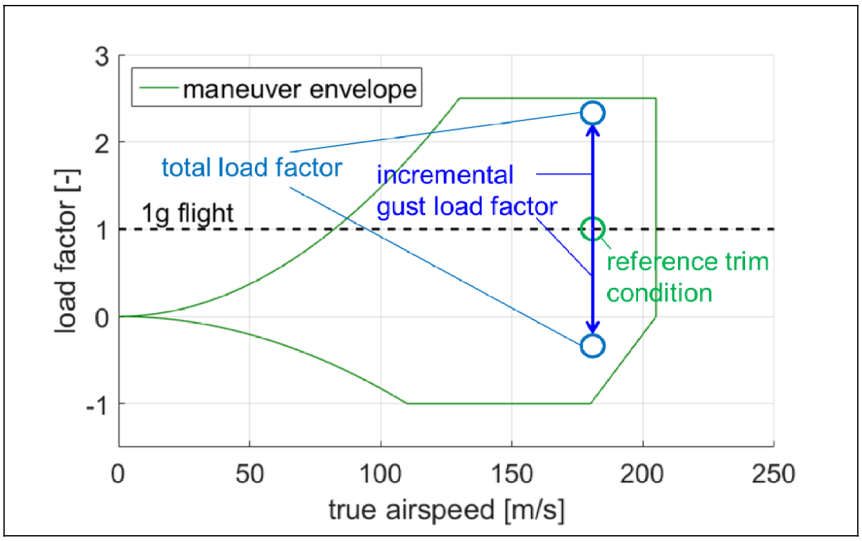

Figure 3.3. Exemplary superposition of load factors during gust encounter

The second step of filtering is carried out after the superposition. 2D envelopes are generated for the maneuver cut loads and the superposed cut loads from the gust simulations. The combination of the load component is M_x/M_y (see Figure 3.4) as well as M_x/F_z. The 2D envelopes are created at every monitoring station. The load cases appearing on the edges of the 2D envelopes comprise the loads considered in the structural optimization.

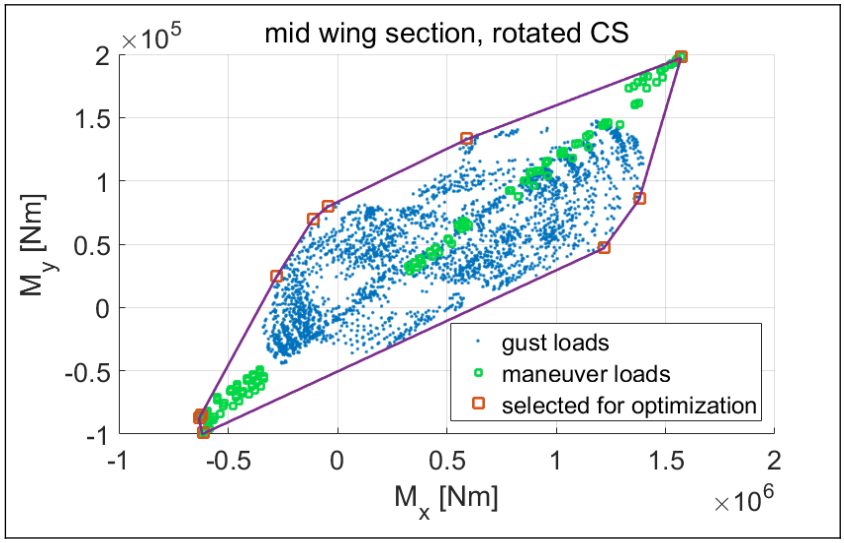

Figure 3.4. 2D envelope surrounding gust and maneuver loads

3.4 Structural optimization

Based on the resulting loads from the maneuver and 1-cos gust simulations, the primary structure of the wing and HTP is optimized using SOL200 of MSC.Nastran [65] that implements gradient-based algorithms. The considered constraints are material strength, buckling stability and minimum thickness that are described in more detail in Subsection 6.1.6 and 7.1.5, as well as aeroelastic constraints elaborated in Section 3.5. The mathematical formulation of the optimization task is:

$$\min(f_{opt}(x_v) \mid \{g_c(x_v)\} \leq \{0\}\,; \{x_{v,min}\} < \{x_v\} < \{x_{v,max}\}), \tag{3.6}$$

with:

f_{opt} : objective function to be minimized, e.g. structural mass,
x_v : design variables,
g_c : optimization constraints,
$x_{v.min}$, $x_{v,max}$: lower and upper limits of the design variables.

An example of the constraint formulation for the stress is:

$$g_{c,\sigma} = 1 - \frac{\sigma_{lim}}{\sigma_m} \leq 0, \tag{3.7}$$

with:

$g_{c,\sigma}$: stress constraint,
σ_{lim} : limit stress,
σ_m : von-Mises stress.

Figure 3.5 visualizes the structural optimization algorithm in MSC.Nastran. At the beginning of the optimization process, an initial design – either from the preliminary cross-section sizing in ModGen as described by Klimmek [53] or the previous cycle of loads and optimization – is put in. Along with the included applied loads, a structural analysis is run. The output of the structural analysis such as stresses and strains is declared as analysis variables y_v. Subsequently, a constraint screening and a sensitivity analysis is conducted. Together with the structural analysis results, the design sensitivities are used to create an approximate model based on Taylor series expansions of objectives and constraints according to the optimization algorithm [65]. With this approximate model, the number of analyses of the full structural model is kept to a minimum and the approximated variables are defined as $\tilde{y}_v$, $\tilde{f}_{opt}$ and $\tilde{g}_c$. The optimizer then communicates with the approximate model. The optimization algorithm used in this thesis is IPOPT (interior point method) that is very robust [65]. After the optimizer has finished the task, the structural model is updated. With the new structural model that is denoted as the improved design, a new structural analysis can be conducted. This iterative design optimization continues until a predefined convergence criterion is met. For the D150 configuration, the defined convergence criterion is a relative mass change of $5.0 \cdot 10^{-4}$ between two design iterations, while a relative mass change of $1.0 \cdot 10^{-3}$ is set for the ALLEGRA configuration due to its non-isotropic material properties and thus longer computing time within the structural optimization. The objective of the structural optimization lies in minimizing the structural mass while complying with the constraints under the applied loads.

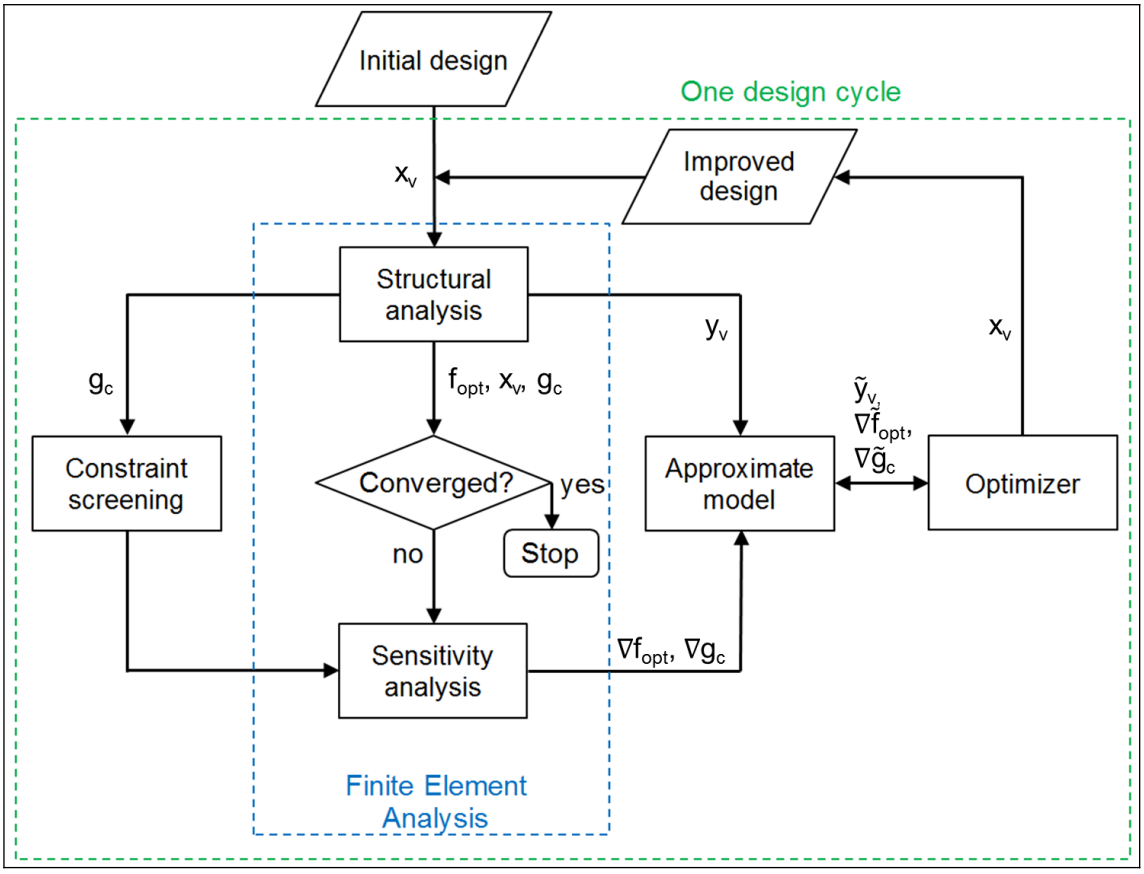

Figure 3.5. Structural optimization flowchart

3.5 Aeroelastic constraints

Beside constraints concerning the structural strength, buckling stability and minimum thickness, static aeroelastic requirements are considered in the structural optimization as well. According to CS25.629, there must be no instability at any speed up to V_D/M_D+15% [20] where V_D is the design dive speed and M_D is the design dive Mach number. Figure 3.6 shows an exemplary flight envelope for the aeroelastic constraints with the stall speed V_S and design dive speed V_D. In this thesis, the focus lies on aileron reversal and divergence.

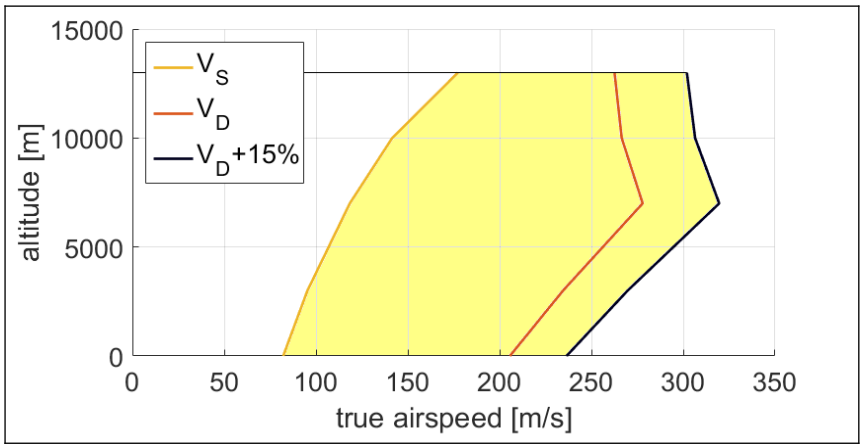

Figure 3.6. Exemplary flight envelope for aeroelastic constraints

Aileron reversal

On an elastic aircraft, an aileron deflection during flight causes the wing to twist due to the torsion moment generated. The twist itself changes the local angle of attack of the wing and counteracts the aileron deflection. As a result, the effectiveness of the aileron is reduced. This effect becomes more pronounced with increasing dynamic pressure. An aileron reversal occurs at the dynamic pressure where the aileron effectiveness becomes negative.

In this case, the aileron effectiveness is defined as the ratio between the roll derivative due to aileron deflection of the elastic aircraft $c_{l\xi}(\mathrm{elastic})$ and that of the rigid aircraft $c_{l\xi}(\mathrm{rigid})$. To meet the requirement defined in CS25, the aileron effectiveness at the aforementioned flight envelope has to be positive:

$$\left.\frac{c_{l\xi}(\mathrm{elastic})}{c_{l\xi}(\mathrm{rigid})}\right|_{1.15\cdot V_D} > 0. \tag{3.8}$$

Backward swept wing configurations are more prone to aileron reversal since the bending-torsion-coupling of the wing reduces the aileron effectiveness further. Therefore, this phenomenon is investigated on the D150 configuration [54].

The constraint is implemented in SOL200 of MSC.Nastran by setting the minimum allowable aileron effectiveness to 1% at V_D/M_D+15%. If a reversal occurs, the wing is re-optimized, where the objective function is minimum mass and only an increase of the material thicknesses is allowed [54].

Divergence

On forward swept wing configurations, the static aeroelastic instability that is more likely to occur is divergence. In a two-dimensional case where the center of pressure is in front of the wing's elastic axis, the lift force induces a torsional moment which causes the wing to twist nose up. This in turn increases the lift and torsion until an equilibrium between the aerodynamic and elastic forces of the wing is reached. With increasing dynamic pressure, the wing twist at the equilibrium state increases, and a divergence occurs when the theoretical wing twist is infinite. In a 1 DoF system with the elastic wing twist angle δ_{el}, the mathematical formulation of the divergence is:

$$0 = [K - \bar{q}_{div} Q]\delta_{el} \mid \delta_{el} \to \infty, \tag{3.9}$$

with:

K : stiffness matrix,
$\bar{q}_{div}$: divergence dynamic pressure,
Q : aerodynamic stiffness matrix,
δ_{el} : elastic wing twist angle.

If the wing is swept forward, the bending-torsion-coupling increases the effect of positive wing twist, and this decreases the divergence dynamic pressure. Therefore, this phenomenon is investigated on the ALLEGRA configuration.

The constraint is implemented in SOL200 of MSC.Nastran by setting a dynamic pressure equivalent to V_D/M_D+15%, up to which divergence must not occur. If a divergence occurs, the wing is re-optimized, and the objective function is mass minimization. In doing so, only an increase of the material thicknesses is allowed.

Theoretically, all constraints – in this case strength, buckling and aeroelastic stability – can be considered in one single optimization run. Due to the heterogeneous constraints however, such an optimization problem would significantly become more complex and the computing times would significantly increase. Since the aeroelastic constraints are not expected to have a large impact on the design that is optimized for material strength and buckling stability, the consideration of aeroelastic constraints in a separate optimization is seen as acceptable.

3.6 Subsonic flutter check

The subsonic flutter checks are intended to ensure that the optimized reference aircraft do not flutter at the prescribed dynamic pressure. These checks are performed with SOL145 of MSC.Nastran [64]. The chosen flutter solution method is the fast KE-method that is based on the K-method. The equation of motion involved in the K-method is similar to Equation (3.3) that is used for the gust simulation:

$$\left[-M_{hh}\omega^2 + iB_{hh}\omega + K_{hh} - \bar{q}Q_{hh}(Ma,k)\right]\{u_h\} = 0, \tag{3.10}$$

with:

M_{hh} : modal mass matrix,
ω : circular frequency,
B_{hh} : modal damping matrix,
K_{hh} : modal stiffness matrix,
$\bar{q}$: dynamic pressure,
Q_{hh} : aerodynamic matrix,
Ma : Mach number,
k : reduced frequency,
u_h : modal displacements.

Within MSC.Nastran, Equation (3.10) is modified slightly by introducing an artificial damping d:

$$\omega \rightarrow \frac{\omega}{\sqrt{1+id}}. \tag{3.11}$$

Equation (3.10) is only valid at the flutter point, i.e. where d is zero. Besides, the airspeed V_{TAS} is written as:

$$V_{TAS} = \frac{\omega\bar{c}}{2k}. \tag{3.12}$$

In the fast KE-method, all viscous dampings B_{hh} such as structural or control system damping are neglected, so that the physically relevant results are restricted to eigenvalues around the flutter point. Moreover, complex eigenvectors of the flutter modes are not available in the KE-method [64]. The equation of motion implemented in MSC.Nastran is:

$$\left[\left[\left(\frac{2k}{\bar{c}}\right)^2 M_{hh} + \frac{\rho}{2} Q_{hh}(Ma,k)\right]\left(\frac{-{V_{TAS}}^2}{1+id}\right) + K_{hh}\right]\{u_h\} = 0, \tag{3.13}$$

with:

$\bar{c}$: mean aerodynamic chord [m],
ρ : mass density of air [kg/m³],
V_{TAS} : true airspeed [m/s],
d : artificial structural damping [-].

Thus, the square of the eigenvalues p_f is defined by:

$${p_f}^2 = \frac{-{V_{TAS}}^2}{1+id}. \tag{3.14}$$

Equation (3.13) is solved for each mode and each step of reduced frequency. Within MSC.Nastran, the eigenvalues are sorted based on their finite differences between the reduced frequencies. With the sorting method, V-d (airspeed and damping) and V-f (airspeed and frequency) curves can be created and interpreted physically [64].

With the Doublet-Lattice-Method, transonic effects cannot be considered. This can become relevant around the transonic dip where the dynamic pressure of the flutter point is reduced due to the transonic effects. To cover this case, high-fidelity simulations such as CFD would become necessary.

3.7 Workflow of the design process

The steps described in the previous sections are implemented in an automated, iterative workflow for the design process with loads analysis and structural optimization. With the initial presized design from ModGen, a condensation of the global stiffness and properties (see Section 2.2) is conducted. The condensed FE-model, along with the aerodynamic model, is used for the gust (see Section 3.2), trim and maneuver (see Section 3.1) calculations. The loads extracted from the gust simulations are then superposed with the corresponding trim loads. Subsequently, the maneuver and gust load cases – which are relevant for the structural optimization – are filtered using the load envelopes (see Section 3.3). With the filtered load cases, the structure of the wing and HTP is optimized (see Section 3.4). The resulting design is put in for the aeroelastic optimization (see Section 3.5). If the defined aeroelastic constraints are violated, the design is adjusted to fulfill the constraints. The design properties from the aeroelastic optimization are then extracted for the next cycle of loads analysis and structural optimization. The cycle is repeated until the relative change in wing structural mass between two cycles is below 0.5%. After the optimized design is reached, a subsonic flutter check (see Section 3.6) is run to ensure that the aircraft does not flutter at the prescribed dynamic pressure envelope. In case of an emerging flutter problem, an implementation of a flutter optimization would become necessary. Figure 3.7 visualizes the implemented workflow.

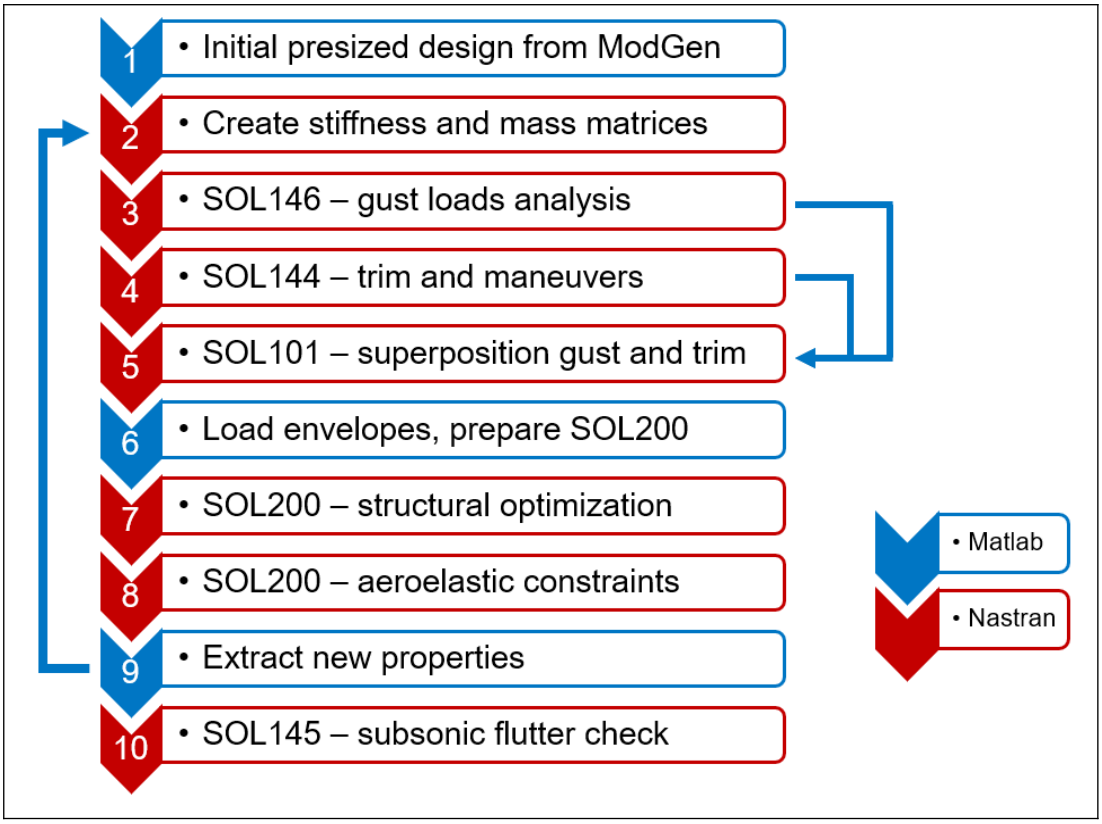

Figure 3.7. Workflow of loads analysis and optimization chain

4 Modeling of load alleviation systems

This chapter explains the objectives of load alleviation and which restrictions are to be considered. These restrictions comprise the assignment of control surfaces used in the maneuver and gust load alleviation respectively. A synthesis of the algorithm for maneuver load alleviation (MLA) that is based on the potential theory follows.

Subsequently, the derivation of the gust load alleviation (GLA) algorithm is explained. This begins with a list of restrictions concerning the dynamics of the GLA. Furthermore, considerations regarding the selection of input parameters for the GLA are elaborated. While taking the mentioned aspects into account, a transfer function of the GLA is synthesized in the frequency domain. Using the transfer function and the respective input during a gust encounter, the GLA command is calculated. This is then transformed into the time domain. To meet the time domain requirements as well, rate limiters are implemented before the GLA deflection is fed into the simulation. A flowchart visualizing the inclusion of GLA in the gust simulation is shown at the end of this chapter.

4.1 Objectives and restrictions

The aim of load alleviation is to reduce the wing loads – especially bending moment – resulting from the design load cases. In the preliminary aircraft design stage, the wing planform and the control surface layout are fixed. This means that the load alleviation should be carried out using the existing control surfaces. High lift systems are not used since the conventional ones can only be extended at low airspeeds. Spoilers are indeed used for load alleviation as well [7]. In this thesis however, spoilers are not included in the load alleviation algorithm since the modeling of spoilers aerodynamics without any DLM correction is unreliable as DLM does not consider flow separation when spoilers are extended.

With the constraints mentioned above and the assumption of symmetric loads, the options available to reduce wing loads are to deflect ailerons and/or elevators. For maneuvers, the load alleviation deflects the ailerons symmetrically to shift the center of lift towards the wing root and reduce the wing bending moment. The resulting change in pitching moment due to the aileron deflection is compensated with the elevators.

During gust encounters, the gust load alleviation deflects the ailerons to reduce the lift increment induced by gusts and – analogous to maneuver load alleviation – to reduce the wing bending moment. The elevators can also be used e.g. to compensate the pitching moment resulting from the aileron deflection. However, elevators are only effective at low frequencies (up to the short period mode), while the highest gust loads typically emerge at higher frequencies (around the first wing bending mode). A transfer function of the D150 in a climb phase emphasizes the effect, see Figure 4.1. The input is the elevator deflection $\eta(f)$ and the output is the bending moment $M_x(f)$ at the wing root. The Bode plot shows that the short period mode occurs at approx. 0.2 Hz, and above that frequency, the influence of the elevator

on the wing root bending moment decreases rapidly. Indeed, elevators can be actuated at higher frequencies, however, this would likely excite fuselage modes without significantly changing the wing loads, and this is undesirable for GLA. For this reason, the elevators are not used for GLA.

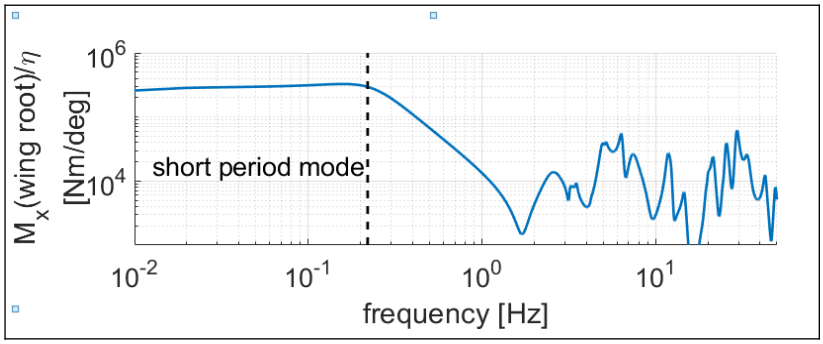

Figure 4.1. Wing root bending moment response to elevator deflection

Furthermore, the load alleviation systems are assumed to have a failure probability below 10^{-5} per flight hour. Taking this into account, the limit load calculations for the failure condition only have to consider a safety factor of 1.0 instead of 1.5 according to Appendix K25.2(c)(2)(ii) of CS25 [20]. Since the load alleviation systems are not expected to reduce loads by more than 33%, the safety factor of 1.0 is inherently achieved and load calculations for the failure condition are omitted.

4.2 Maneuver load alleviation concept

The maneuver load alleviation (MLA) is carried out by deflecting the ailerons symmetrically. To avoid interference with the flight mechanic controller, the MLA should only react to the commanded load factor, but not to the actual load factor. At a load factor of 2.5, the ailerons are deflected upward, and at a load factor of -1.0 downward. This is supposed to shift the center of lift to the root, so that the bending moment is reduced at approximately the same level of lift force, see Figure 4.2.

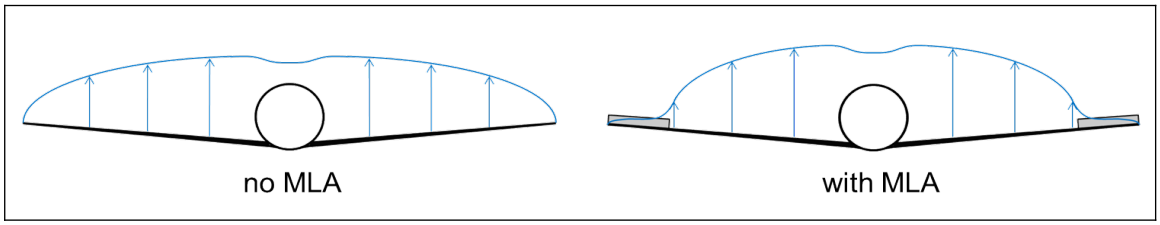

Figure 4.2. Change of spanwise lift distribution with MLA during a pull-up maneuver

The aileron deflection for MLA is set to 8° at the design cruise speed V_C and a load factor of 2.5. Compared to the Lockheed L-1011 (13° at 2.5g) [77], the value taken is indeed relatively small. However, the MLA deflection in this thesis is defined as a function of the airspeed. Hence, the MLA deflections at airspeeds below V_C are larger than 8°, as shown at the end of this section.

To calculate the aileron deflection amplitude for other airspeeds, an ideal case of a rigid, symmetric wing profile with no twist is used as reference. To achieve a constant ratio between lift due to angle of attack and lift from MLA, the aileron deflection has to be proportional to the angle of attack: $\xi \sim \alpha$. The constant lift ratio also yields a constant ratio between the shear force F_z and torsion moment M_y. Furthermore, with constant lift, the angle of attack is inversely proportional to the dynamic pressure: $\alpha \sim \frac{1}{\bar{q}}$. With those proportionality relationships, it can be derived that the aileron deflection ξ should be inversely proportional to the dynamic pressure $\bar{q}$:

$$\xi \sim \frac{1}{\bar{q}}. \tag{4.1}$$

Indeed, for an aircraft with an elastic wing, twist, camber and variable mass, an MLA algorithm as stated in Equation (4.1) will not yield a perfectly constant alleviation effect at every dynamic pressure. However, this approach is still more advantageous compared to setting a constant aileron deflection gain for the 2.5g case over the whole range of dynamic pressure. With a constant aileron deflection gain, at low speeds the alleviation effect would be relatively small, and at high speeds the ailerons might overcompensate the local lift which would decrease the aerodynamic performance of the aircraft. Additionally, this overcompensation would create a large aileron hinge and wing torsion moment.

This range between the small alleviation effect and the overcompensation would also make the 2D load envelopes mentioned in Section 3.3 less slender: the first case would evoke a large bending moment and a small torsion, while the latter would cause a small bending moment and a large torsion. This aspect is further investigated in Section 8.1.

With regard to structural optimization, the less slender load envelope would yield a heavier structure. The reason is: with a slender load envelope, the ratio between bending moment and torsion is more constant. Hence, the stress distributions and load paths among the different load cases are more similar.

Therefore, the maximum MLA amplitude $|\xi_{max}|$ for the +2.5g and -1g is set to 8° with following algorithm:

$$\xi(\bar{q}, n_{z,c}) = \begin{cases} -|\xi_{max}| \cdot \frac{\bar{q}_C}{\bar{q}} \cdot \frac{n_{z,c}-1.0}{n_{z,max}-1.0} = -8° \cdot \frac{\bar{q}_C}{\bar{q}} \cdot \frac{n_{z,c}-1.0}{1.5} \text{ for } n_{z,c} > 1 \\ -|\xi_{max}| \cdot \frac{\bar{q}_C}{\bar{q}} \cdot \frac{n_{z,c}-1.0}{1.0-n_{z,min}} = -8° \cdot \frac{\bar{q}_C}{\bar{q}} \cdot \frac{n_{z,c}-1.0}{2.0} \text{ for } n_{z,c} < 1 \end{cases}, \tag{4.2}$$

with:

ξ : aileron deflection [deg],
$n_{z,c}$: commanded load factor [-],
$\bar{q}_C$: dynamic pressure at design cruise speed [Pa],
$\bar{q}$: actual dynamic pressure [Pa].

An example of the MLA deflection: at the maneuvering speed V_A of the D150 where the dynamic pressure is low with $\bar{q}_A \approx 0.52\,\bar{q}_C$, the MLA deflection $\xi(\bar{q}_A)$ at 2.5g is -15°. This value is comparable to the MLA of the Lockheed L-1011 (-13° at 2.5g) [77].

4.3 Gust load alleviation concept

Requirements

Beside for MLA, symmetric aileron deflections are also used to reduce the lift increment during gust encounters – which also evokes a reduction of wing bending moment. Following constraints are taken into account for the gust load alleviation (GLA) implemented here:

- Only basic control system elements are used. Those elements comprise proportional, integral, derivative terms as well as low-pass and high-pass filters.
- A delay time between the signal detection at the sensor and the control surface actuation is considered. Wildschek [99] applied a delay of 60 ms, while a maximum value of 100 ms should not be exceeded. In the simulations for this work, a minimum delay time of 60 ms is assumed.
- A maximum aileron deflection of 10° and a deflection rate of 40°/s – as applied by Xu [105] – are not exceeded.

Input parameters for GLA

Existing aircraft with GLA function use inertial or aerodynamic sensors or a combination of both to reduce loads or improve ride comfort [80]. On both reference aircraft, GLA only using inertial sensors hardly contributes to load reduction during 1-cos gust encounters, and this is caused by the following:

- The maximum wing loads predominantly emerge when the gust base frequency defined in Equation (3.4) is approximately equal to the first wing bending frequency.
- The frequency of the first wing bending mode of both reference aircraft lies between 2.0 Hz and 3.5 Hz.
- With an assumed delay of 60 ms during a gust encounter, the first wing bending oscillation would almost reach the maximum displacement – with it the maximum bending moment – before the ailerons start to deflect.

Therefore, aerodynamic sensors are considered in the control algorithm. The sensors are assumed to be placed at the aircraft nose and the input parameter is the angle of attack increment due to gust as defined by König et al. [55]:

$$\alpha_g = \alpha_m - \theta + \frac{\dot{z}}{V_{TAS}} + \frac{q \cdot r_{CG}}{V_{TAS}} \approx \frac{w_g}{V_{TAS}}, \tag{4.3}$$

with:

α_g : angle of attack increment due to gust [rad],
α_m : measured angle of attack [rad],
θ : aircraft pitch angle [rad],
$\dot{z}$: aircraft vertical speed [m/s],
V_{TAS} : aircraft true airspeed [m/s],

q : aircraft pitch rate [rad/s],
r_{CG} : distance between aerodynamic sensor and aircraft center of gravity [m],
w_g : vertical wind speed [m/s].

Using the aerodynamic sensors at the aircraft nose also has the advantage that there is a time buffer between the gust detection at the nose and the gust hitting the wing. Hence, the effective delay of the aileron deflection is significantly smaller. As an example: at a design cruise speed of 256.0 m/s TAS and with the 25% of the mean aerodynamic chord (MAC) placed 16 m behind the aircraft nose, it takes 62.5 ms for the gust to reach the 25% MAC after being detected. In this case, the effective delay of the aileron deflection is 0 ms, and the flight control computer still has a buffer of 2.5 ms – if the aileron should start to deflect when the gust reaches the 25% MAC.

Synthesis of GLA transfer function

Figure 4.3 shows the block diagram of the GLA control loop, with the gust angle of attack as input and the aileron deflection as output. Since the dynamic behavior of the aircraft is not affected by the GLA, it is a feed-forward controller. This aspect contributes to the simplicity in the simulations significantly, as opposed to a feedback controller. Moreover, the delay time between the gust detection at the nose and the aircraft response is assumed to be included in the aircraft block in Figure 4.3.

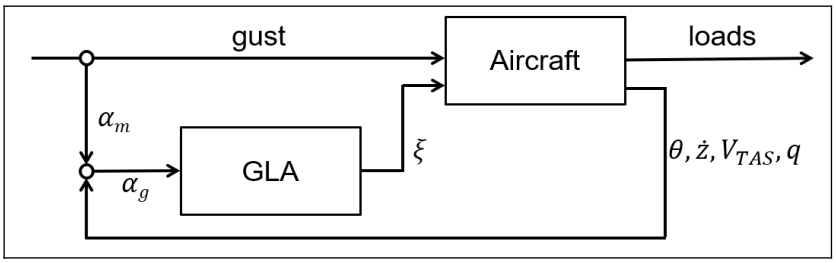

Figure 4.3. Block diagram of feed-forward GLA

For the first step, a proportional term is considered for the GLA, and the amplification factor $k_a = \frac{\Delta\xi_a}{\Delta\alpha_g}$ is set to -2.0. The term ξ_a refers to the aileron deflection in the aerodynamic coordinate system. The value of -2.0 for k_a is derived by applying the potential theory elaborated in Schlichting-Truckenbrodt [84]: for a trailing edge control surface with a relative rudder chord of 0.25 and an aerodynamic effectiveness of 0.75, the derivative $\frac{\partial\alpha}{\partial\xi_a}$ is 0.5. In other words, a control surface deflection ξ_a of 1° generates lift equivalent to a change in angle of attack α by 0.5°. Figure 4.4 shows the orientations of α and ξ_a on a thin wing profile.

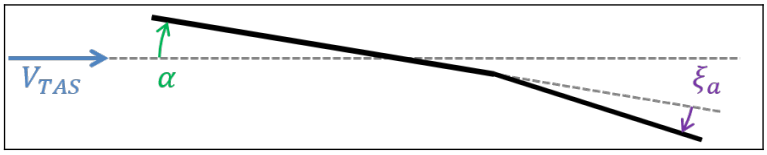

Figure 4.4. Illustration of angle of attack and aileron deflection

As reference: the aileron relative chord of the D150 configuration is 0.30, and the aileron on the ALLEGRA configuration has a relative chord of 0.26. Thus, with an amplification factor k_a of -2.0, in a steady state and with rigid structure, the aileron deflection roughly compensates the lift increment at the wingtip area due to a change in the angle of attack. For the aileron deflection in the hinge coordinate system, the gain k_{GLA} is calculated by:

$$k_{GLA} = \frac{k_a}{\cos(\varphi_{hinge})} = \frac{-2.0}{\cos(\varphi_{hinge})}, \tag{4.4}$$

with:

φ_{hinge} : sweep angle of the hinge line [deg].

Since gust encounters are transient phenomena and the maximum loads occur within one second after the gust detection at the aircraft nose, an inclusion of an integral term in the controller is seen as unnecessary. A derivative term has the advantage that it can reduce the phase lag caused by the delay, however the control amplitude increases at higher frequencies. This combination will lead to an accordingly high commanded aileron travel rate and also high hinge moment values. For this reason, no derivative term is included in the controller.

Beside the proportional term, a second-order low-pass filter is set at 10 Hz to further avoid having excessive commanded aileron travel rates and hinge moments at small deflection amplitudes. The cutoff frequency of 10 Hz also roughly represents the bandwidth of control surfaces with hydraulic actuation according to Brockhaus et al. [7]. Furthermore, a second-order high-pass is set at 0.1 Hz to eliminate offsets in the measurement of parameters involved in Equation (4.3).

The delay time is adjusted to the airspeed, so that the ailerons are deflected after a constant distance of gust penetration to prevent deflecting the ailerons too early or too late at different airspeeds. With a defined minimum of 60 ms, the delay time is expressed by:

$$t_{del} = \max\left(\frac{x_{wing}}{V_{TAS}}, 0.06\ \mathrm{s}\right), \tag{4.5}$$

with:

t_{del} : delay time [s],

x_{wing} : x-position of the wing [m],

V_{TAS} : true airspeed [m/s].

However, the position x_{wing} is not exactly defined yet; this can range e.g. from the foremost leading edge to the sternmost trailing edge. According to a study elaborated in Section 8.2, it turns out that setting x_{wing} to 16 m on the D150 configuration yields the largest reduction of the wing root bending moment. On the ALLEGRA configuration, x_{wing} is set to 18 m to maximize the load alleviation effect. Figure 4.5 visualizes these two positions, and it is apparent that the ailerons should start deflecting relatively soon after the gust hits the foremost leading edge of the wing.

With the selected controller features, the transfer function of the GLA with the commanded aileron deflection ξ_c as output and gust angle of attack α_g as input is:

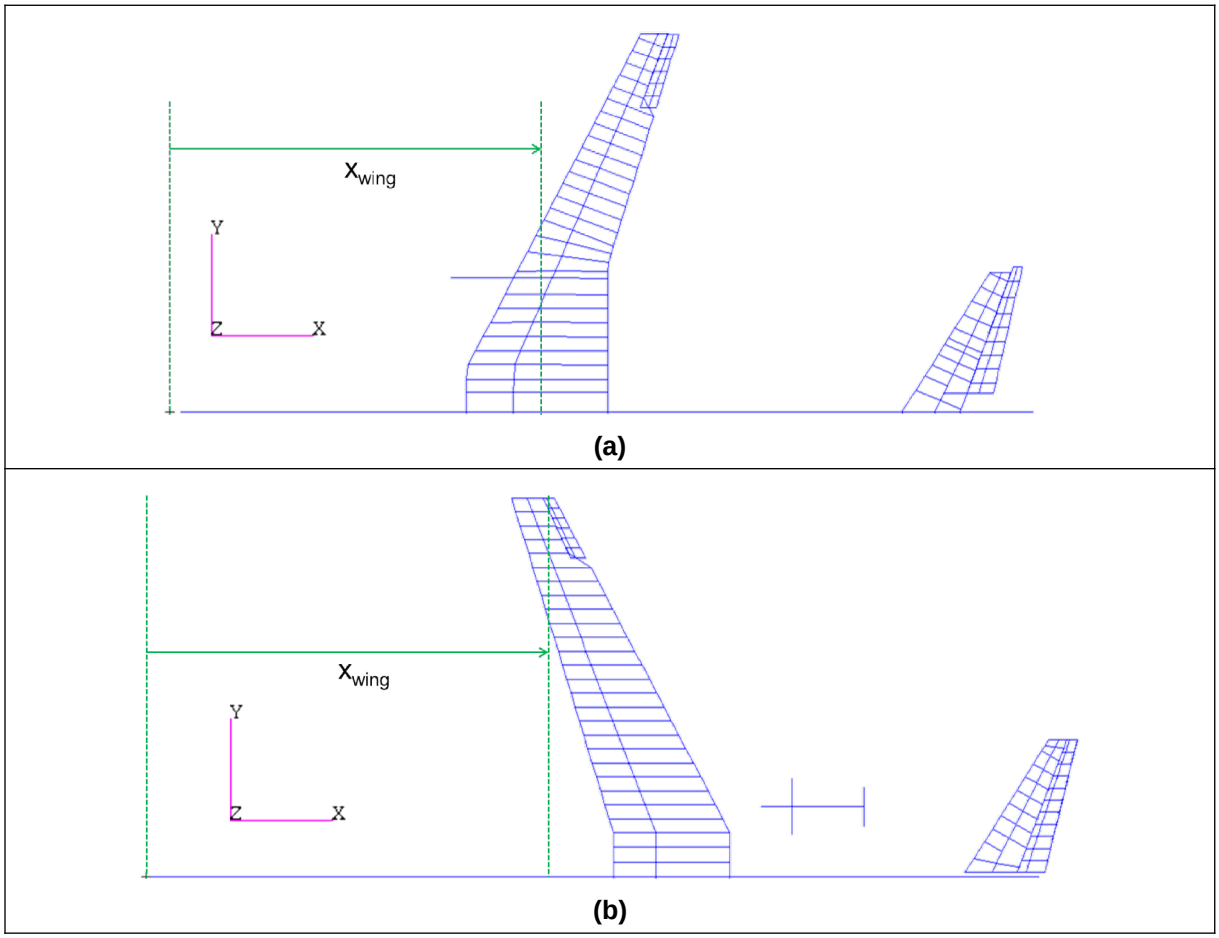

Figure 4.5. Visualization of the reference positions x_{wing} on D150 (a) and ALLEGRA (b)

$$TF_{GLA}(f) = \frac{\xi_c(f)}{\alpha_g(f)} = k_{GLA} \cdot TF_{LP}(f) \cdot TF_{HP}(f) \cdot TF_{del}(f), \tag{4.6}$$

with:

$$TF_{LP} = \left(\frac{1}{\frac{i \cdot f}{f_{LP}} + 1} \right)^2, \tag{4.7}$$

$$TF_{HP} = \left(\frac{\frac{i \cdot f}{f_{HP}}}{\frac{i \cdot f}{f_{HP}} + 1} \right)^2, \tag{4.8}$$

$$TF_{del} = e^{-2\pi \cdot if \cdot t_{del}}, \tag{4.9}$$

and:

TF_{GLA} : GLA transfer function [-],
ξ_c : commanded aileron deflection [rad],
α_g : angle of attack increment due to gust [rad],
f : frequency [Hz],
k_{GLA} : GLA gain [-],
TF_{LP} : transfer function of the low-pass filter [-],
TF_{HP} : transfer function of the high-pass filter [-],
TF_{del} : transfer function of the delay time [-],

f_{LP} : low-pass cutoff frequency [Hz],
f_{HP} : high-pass onset frequency [Hz],
t_{del} : delay time [s].

The term “commanded aileron deflection” implies that the rate limiter has not been applied yet. With the GLA transfer function in Equation (4.6) and a given vertical wind speed in the frequency domain, the commanded aileron deflection ξ_c is calculated by:

$$\xi_c(f) = TF_{GLA}(f) \cdot \alpha_g(f), \tag{4.10}$$

with:

ξ_c : commanded aileron deflection [rad],
TF_{GLA} : GLA transfer function [-],
α_g : angle of attack increment due to gust [rad].

Aileron rate limiter

To meet the requirement of the maximum GLA deflection rate, the deflection command ξ_c is transformed into the time domain so that a rate limiter can be applied. In the time domain, any commanded rate magnitude of larger than 40°/s is limited to 40°/s, and any deviation from the commanded deflection is compensated with a maximum rate of 40°/s. Figure 4.6 shows exemplary commanded and actual aileron deflections (ξ_c and ξ) for three different gust gradients ranging from 9 to 107 m together with the local angles of attack increment due to gust α_g at 25% MAC. The true airspeed is 256.0 m/s which is equal to the design cruise speed of the D150 configuration at an altitude of 7000 m. On the short and medium gusts, it is apparent that the rate limiter intervenes and the actual aileron deflections ξ have an intermittent lag compared to the commanded deflection ξ_c. On the long gust, the commanded aileron deflection rate is low enough that the actual deflection ξ can follow the command ξ_c without any intervention of the limiter. Since the commanded aileron deflection is always below 10° for the considered gusts, the GLA travel limiter at 10° does not intervene. As a remark: the influence of the low-pass filter is visible for the shortest gust: the gust angle of attack α_g reaches its maximum earlier compared to the commanded aileron deflection ξ_c. On the longest gust, their maximums emerge simultaneously.

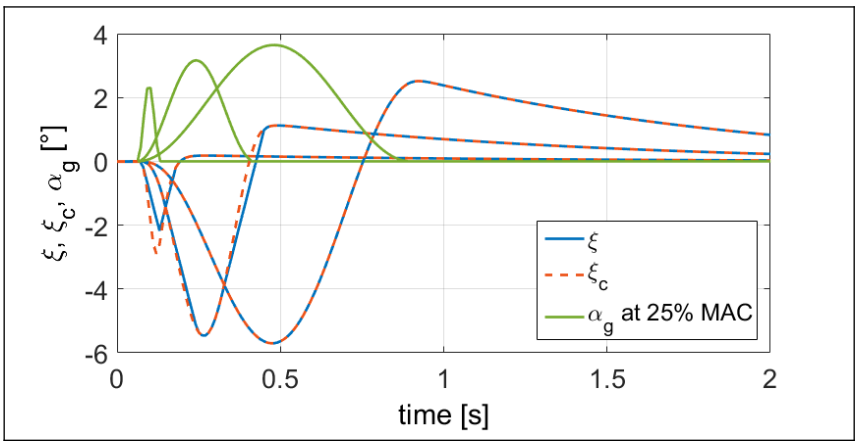

Figure 4.6. Comparison between actual ξ and commanded aileron deflections ξc

Integration of GLA in the 1-cos gust simulation

To integrate the derived GLA in the 1-cos gust simulations, a sub-workflow for step 3 of the workflow shown in Section 3.7 is setup. At first, 1-cos gust time histories encountered by the aircraft are created in the time domain and transformed into the frequency domain. In the frequency domain, gust angles of attack α_g are calculated and multiplied with the GLA transfer function to obtain the commanded aileron deflections ξ_c. These are transformed back into the time domain, and the rate limiting algorithm is applied. Subsequently, the actual aileron deflections ξ are input as time histories into MSC.Nastran, and the aircraft responses are calculated. Figure 4.7 visualizes this sub-workflow.

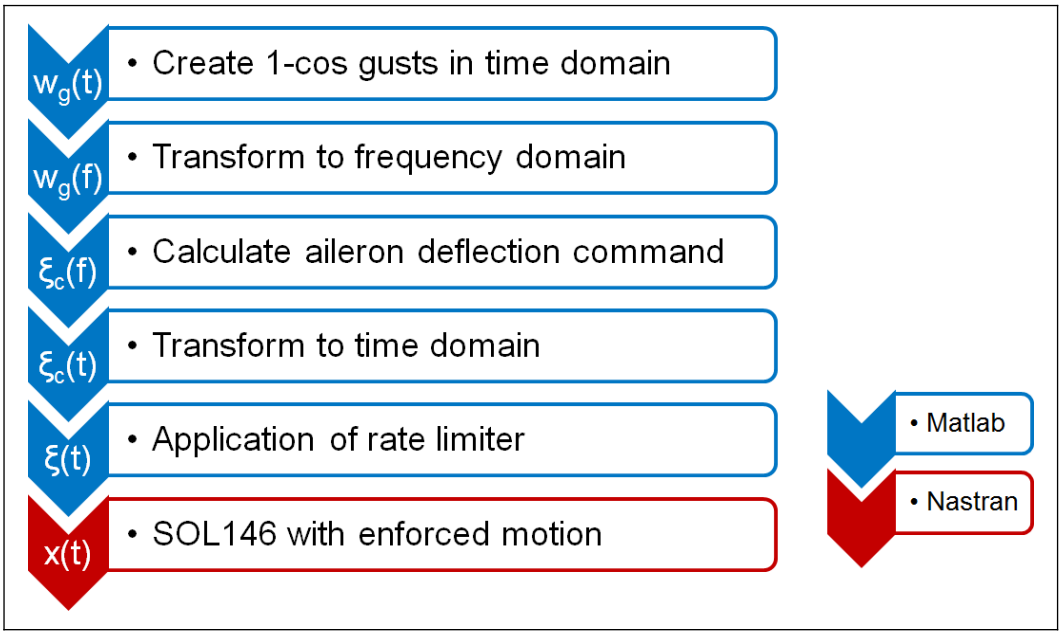

Figure 4.7. Sub-workflow of the GLA integration in the 1-cos gust simulation

5 Methodology of fatigue analysis

This chapter describes the calculation of fatigue damage induced by continuous turbulence and ground-air-ground cycles. For the first step, reference mass configurations, flight phases and turbulence parameters are defined for the each aircraft. Simulations using those parameters are run, and aircraft responses caused by the turbulence are extracted. From the responses, load collectives of the active and passive aircraft are calculated, compared and analyzed. In addition, strain/stress collectives of each aircraft are investigated to calculate the fatigue damage due to continuous turbulence. For the active aircraft, the same GLA algorithm as described in Section 4.3 is used.

5.1 Reference flight parameters

The first parameters to be defined are the **mass configurations** of the reference aircraft. The objective lies in defining the worst-case conditions for the loads evoked by turbulence. In doing so, the mass aspect is divided into two categories:

- Payload masses. During cruise flight, the wing loads – especially at the root – become larger with increasing fuselage mass. The same applies to incremental turbulence loads. Therefore, to induce the maximum wing loads in the turbulence analysis, the aircraft shall carry the maximum payload. The term maximum payload implies that the payload masses bring an empty aircraft (OEM configuration) to its maximum zero fuel mass (MZFM).
- Fuel masses. In gust encounters, the highest wing loads typically occur when the gust base frequency f_g (Equation (3.4)) is near the first wing bending frequency, as mentioned in Section 3.2. This means, the first wing bending mode has a large contribution to the wing loads. On the other hand, in continuous turbulence, most of the energy is stored in the lower frequency range as shown in Section 5.2. Hence, if the first wing bending mode occurs at a lower frequency, it will receive more energy from the turbulence. For this reason, the fuel masses for the reference aircraft should be maximized so that the frequency of the first wing bending is as low as possible. In this case, the fuel masses should bring the reference aircraft from the MZFM to their respective maximum take-off mass (MTOM) with the fueling sequence described in Section 2.2.

Based on the fuel masses, **flight routes** for the reference aircraft are searched to estimate the duration of each flight phase. The criteria of the flight route search are:

- The fuel mass calculation is carried out with Fuelplanner [29]. The reference aircraft for the fuel consumption estimation is the Airbus A320.
- JAR international standard [47] is taken into account for the reserve fuel mass.
- The sum of the trip and reserve fuel should roughly equal the defined fuel masses.

Since the D150 and ALLEGRA configuration have slightly different design masses, each of them has a different flight route for the turbulence analysis. The D150 is assigned for the route from Berlin-Tegel (EDDT) to Porto (LPPR), while the route Berlin-Tegel (EDDT)-Athens International (LGAV) is selected for the ALLEGRA configuration. More details can be found in Section 6.3 and 7.3.

Based on the flight routes, the durations of the climb, cruise and descent as well as the fuel masses in the respective phases are estimated. The reference flight condition for each phase is also defined. For the cruise flight phase, it is assumed that the remaining fuel mass is roughly the take-off fuel subtracted with the half of the trip fuel. Using the estimation, fuel mass models for the respective aircraft and flight phases are generated with ModGen.

5.2 Reference atmospheric turbulence

The reference turbulence considered is the von Kármán spectrum with a scale of turbulence of 762 m (2500 ft) as prescribed in CS25.341(b)(2) [20]. The power spectral density (PSD) of the von Kármán spectrum is defined as follows [40]:

$$\Phi(f) = rms_w^2 \frac{2L_{turb}}{V_{TAS}} \frac{1 + \frac{8}{3}\left(1.339 \cdot 2\pi f \frac{L_{turb}}{V_{TAS}}\right)^2}{\left(1 + \left(1.339 \cdot 2\pi f \frac{L_{turb}}{V_{TAS}}\right)^2\right)^{11/6}}, \tag{5.1}$$

with:

$\Phi(f)$: power spectral density [m²/s²/Hz],
rms_w : root mean square of vertical wind speed [m/s],
L_{turb} : scale of turbulence [m],
V_{TAS} : aircraft true airspeed [m/s],
f : frequency [Hz].

Figure 5.1 shows an exemplary PSD of the von Kármán spectrum for vertical wind with a root mean square (RMS) of 1.0 m/s, a scale of turbulence of 762 m and an aircraft true airspeed of 256.0 m/s.

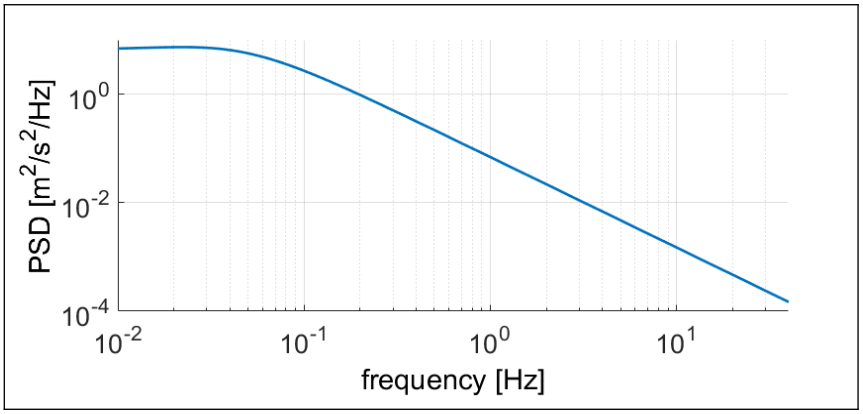

Figure 5.1. Exemplary von Kármán power spectral density

For each reference flight phase, a reference root mean square (RMS) of the vertical wind speed is defined based on the diagram in Figure 5.2 which is taken from MIL-STD-1797A [96]. For the turbulence analysis, it is assumed that the turbulence intensity is moderate such that the probability of exceedance of the RMS is approximately 10^{-3}.

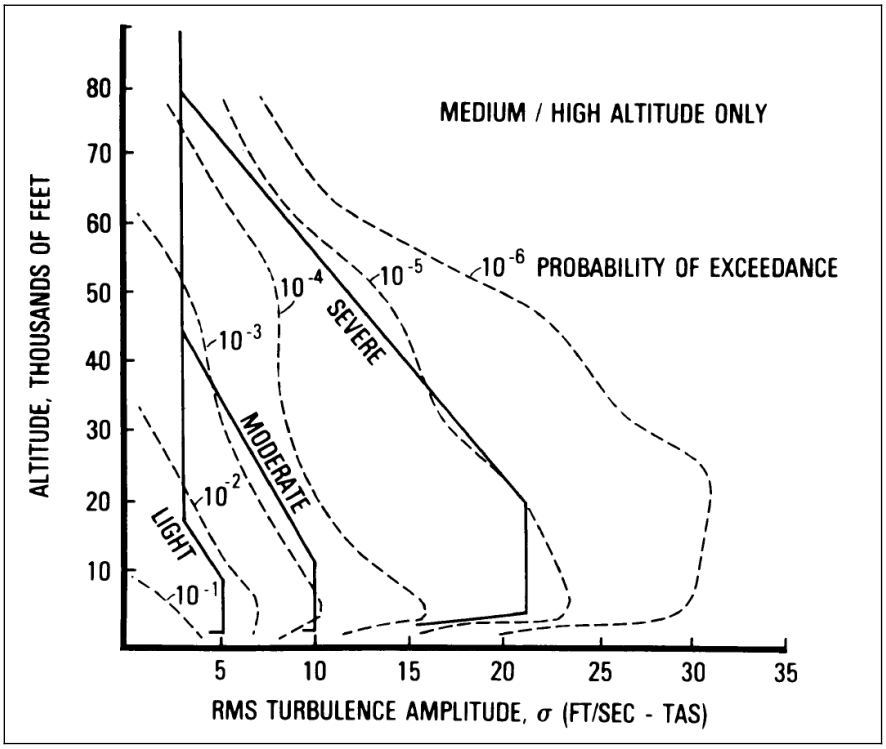

Figure 5.2. Probability of exceedance for various turbulence RMS [96]

To derive the vertical wind speed in the frequency domain, the square root of the reference spectrum is given a random phase angle for each frequency step. Equation (5.2) is used to calculate one side of the two-sided Fourier transform of the vertical wind speed in MATLAB:

$$w_{g,turb}(f) = \sqrt{(\Phi(f) \cdot f_{max} \cdot 2n_f)} \cdot e^{i \cdot \mathrm{rand}(\varphi(f))}, \tag{5.2}$$

with:

$w_{g,turb}$	: vertical wind speed [m/s],
f	: frequency [Hz],
n_f	: number of elements in the frequency vector [-],
Φ	: turbulence power spectral density [m²/s²/Hz],
$\mathrm{rand}(\varphi(f))$	: random phase angle [rad].

Subsequently, $w_{g,turb}(f)$ is adjoined with its flipped complex conjugate form. For an adequate comparability, the phase distribution $\mathrm{rand}(\varphi(f))$ is set equal for the passive and active aircraft. In other words: the climb, cruise and descent phase might have different phase distributions. In each flight phase however, the passive and active aircraft encounter the same turbulence with the same phase distribution.

5.3 Aircraft responses in turbulence analysis

Transfer function generation

For the defined reference flight phases and the respective turbulence spectra, aircraft responses can be calculated using transfer functions (TF) which are generated using MSC.Nastran. The physical principles of the TF generation are the same as gust load calculations, except that the inputs are spectral excitations and the outputs are obtained in the frequency domain instead of the time domain. Since transfer functions are single input single output (SISO) systems, one transfer function is necessary for every combination of input and output quantities.

In this case, the input quantities are unit vertical wind speed and unit aileron deflection, where the output quantities consist of:

- cut loads at the wing root, outer wing section (at 70% half-span) and HTP root,
- aileron hinge moment,
- major principal strain/stress of selected structure elements on the lower skin.

Aileron deflection

The GLA transfer function used for the turbulence analysis is the same as described by Equation (4.6). The input is continuous turbulence expressed by $\alpha_{g,turb}$ instead of 1-cos gusts.:

$$TF_{GLA}(f) = \frac{\xi_c(f)}{\alpha_{g,turb}(f)} = k_{GLA} \cdot TF_{LP}(f) \cdot TF_{HP}(f) \cdot TF_{del}(f), \tag{5.3}$$

where:

TF_{GLA} : GLA transfer function [-],
ξ_c : commanded aileron deflection [rad],
$\alpha_{g,turb}$: angle of attack increment due to turbulence [rad],
f : frequency [Hz],
k_{GLA} : GLA gain [-],
TF_{LP} : transfer function of the low-pass filter [-],
TF_{HP} : transfer function of the high-pass filter [-],
TF_{del} : transfer function of the delay filter [-].

The main feature of the transfer function remains the gain factor k_{GLA} that is set to $\frac{-2.0}{\cos(\varphi_{hinge})}$. The second-order low-pass TF_{LP} at 10 Hz is considered to prevent having excessive deflection rates at higher frequencies. The second-order high-pass TF_{HP} at 0.1 Hz is implemented to avoid having static deflections in a constant wind field. The airspeed-dependent delay TF_{del} is adopted to adjust the timing of the aileron deflection.

With the vertical wind speed derived in Section 5.2, the commanded aileron deflection is calculated with:

$$\xi_c(f) = TF_{GLA}(f) \cdot \alpha_{g,turb}(f) \approx TF_{GLA}(f) \cdot \frac{w_{g,turb}(f)}{V_{TAS}}, \tag{5.4}$$

with:

ξ_c : commanded aileron deflection [rad],
TF_{GLA} : GLA transfer function [-],
$\alpha_{g,turb}$: angle of attack increment due to turbulence [rad],
$w_{g,turb}$: vertical wind speed [m/s],
V_{TAS} : true airspeed [m/s].

Subsequently, the commanded aileron deflection is transformed into the time domain. An aileron rate limiter which is set to a maximum of 40°/s is applied to obtain the actual aileron deflection. The actual aileron deflection is then transformed back into the frequency domain for further processing.

Aircraft response calculation

Analogous to the dynamic gust simulations, the highest frequency considered in the turbulence analysis is 50 Hz. With the Nyquist-Shannon sampling theorem [67], this yields a maximum time increment of 10 ms. To generate statistically relevant load collectives, a sufficient number of time steps in the observed time period is necessary. On the other hand, the computation time and memory requirement also rise with increasing number of time steps. In this case, a number of 10^5 time steps are seen as a reasonable compromise. The number of time steps multiplied with the time increment yields an observed time period of 1000 s and a frequency increment of 10^{-3} Hz. To obtain this discretization, the transfer functions extracted from MSC.Nastran are interpolated. This is done since a direct output of $5 \cdot 10^4$ frequency steps (from 10^{-3} Hz to 50 Hz) is not affordable with regards to computation time and memory requirements.

As a remark: the interpolated transfer functions with $5 \cdot 10^4$ frequency steps are still one-sided. To obtain the two-sided form, the transfer functions have to be adjoined with their flipped complex conjugate form, so that the vector length in the frequency domain is 10^5 and equal to the number of samples in the time domain. Furthermore, to maintain a comparability of the turbulence loads between the passive and active aircraft, the phase angle distribution in Equation (5.2) is identical in each flight phase for both aircraft.

For the passive aircraft, the responses in the frequency domain are calculated using a multiplication of the vertical wind speed $w_{g,turb}(f)$ and the corresponding transfer functions:

$$x(f) = TF_{w_{g,turb} \to x}(f) \cdot w_{g,turb}(f). \tag{5.5}$$

For the active aircraft, the equation has an additional term that is a function of the aileron deflection angle:

$$x(f) = TF_{w_{g,turb} \to x}(f) \cdot w_{g,turb}(f) + TF_{\xi \to x}(f) \cdot \xi(f). \tag{5.6}$$

Subsequently, the responses are transformed into the time domain for further analysis.

Turbulence analysis sub-workflow

Figure 5.3 shows a sub-workflow featuring the aforementioned steps including the derivation of the vertical wind speed in Equation (5.2). For the passive aircraft, the sub-workflow has significantly fewer steps since the aileron deflection is zero and the corresponding operations are skipped.

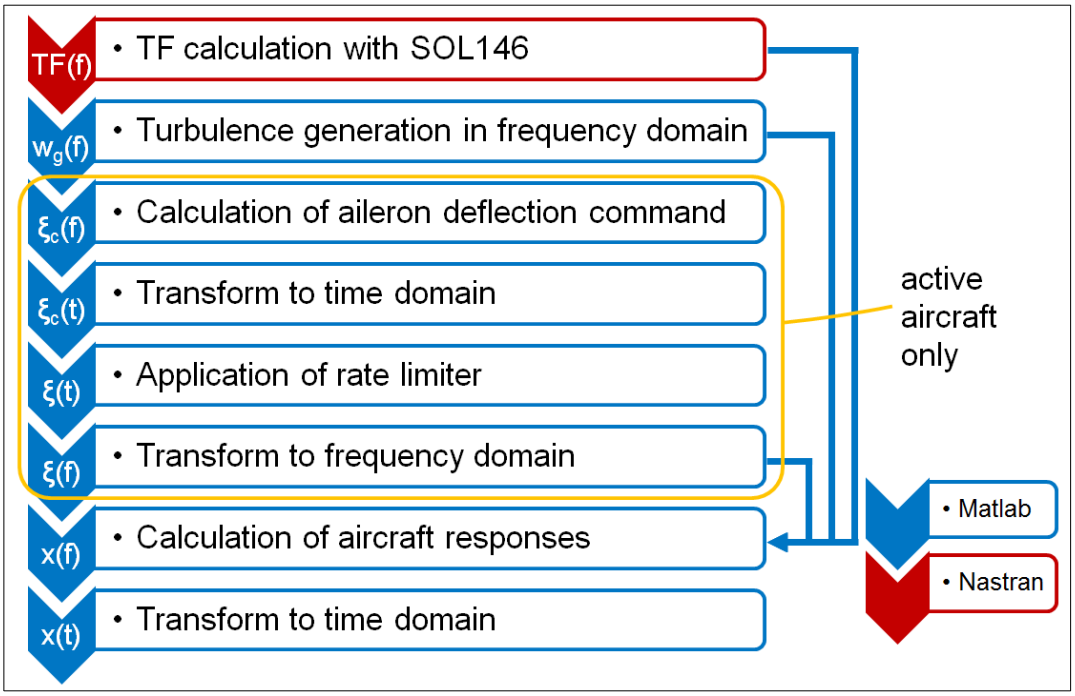

Figure 5.3. Sub-workflow of aircraft response calculation in continuous turbulence

5.4 Rainflow-counting

To derive the collectives from the aircraft responses in continuous turbulence, a rainflow-counting algorithm [68] is applied. The operations conducted are as follows:

1. At first, the time history of e.g. an aircraft response quantity is reduced to its local maxima and minima as shown by a small example in Figure 5.4.

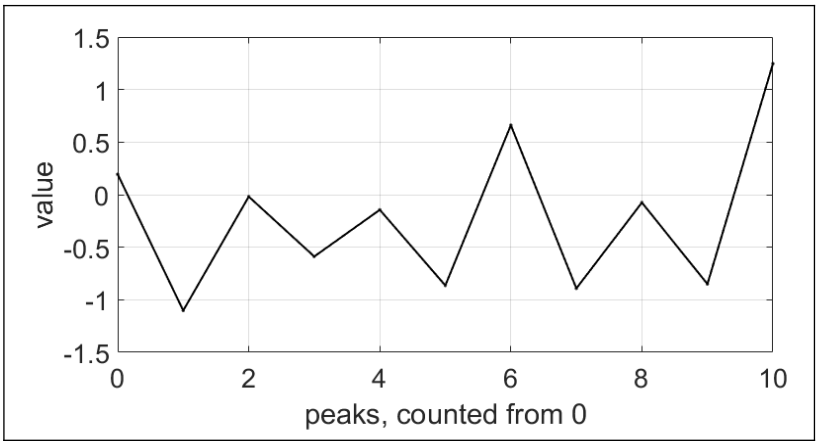

Figure 5.4. Exemplary time history reduced to its peaks

2. The graph is then rotated 90° clockwise and imagined as a pagoda roof.
3. For the ‘rain’ on the left side, each local maximum is imagined as a source of raindrops which start to flow. Vice versa, for the ‘rain’ on the right side, raindrops appear at each local minimum. Figure 5.5 visualizes the emerging raindrops. It is apparent that a few raindrops stop flowing before reaching the edge of the imagined roof, because they will merge with raindrops starting at an earlier peak, as explained in the next step.

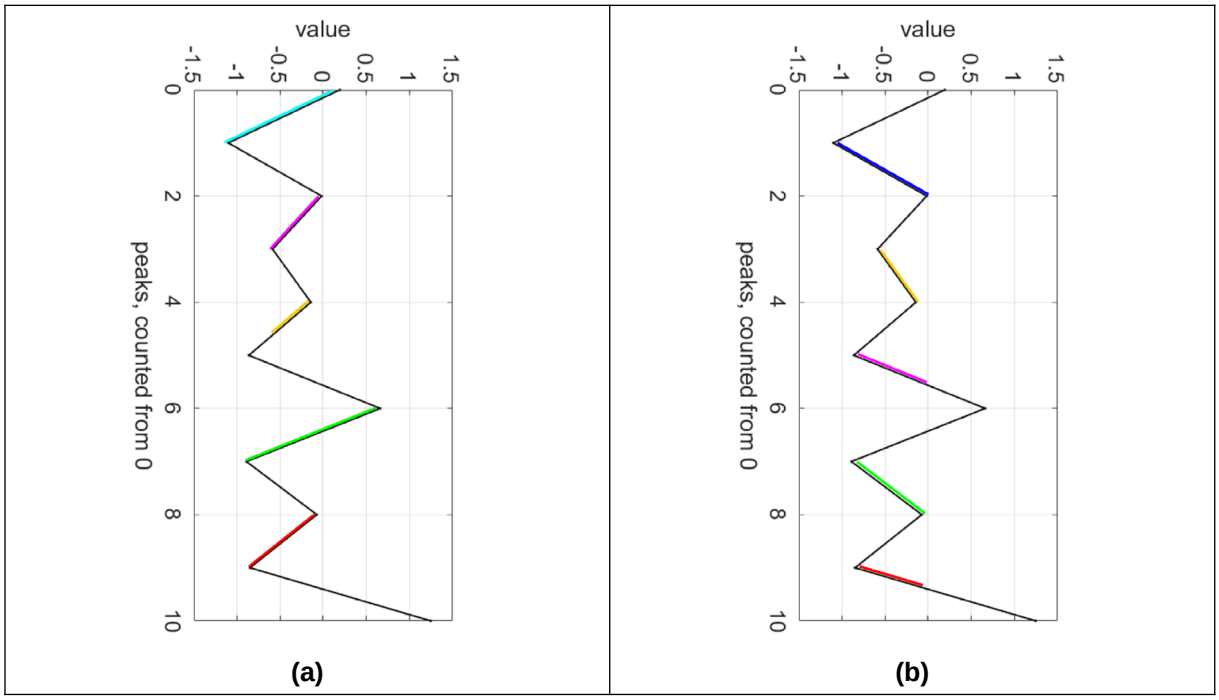

Figure 5.5. Raindrops emerging on the left (a) and right (b) side of the pagoda roof

4. The flow of the raindrops is continued, and it stops if either:
   - it reaches the end of the time history,
   - it merges with a flow which started at an earlier peak, or
   - the next raindrop source has a higher value (for the left side rain) or a lower value (for the right side rain).

   Figure 5.6 shows the flow continuation.

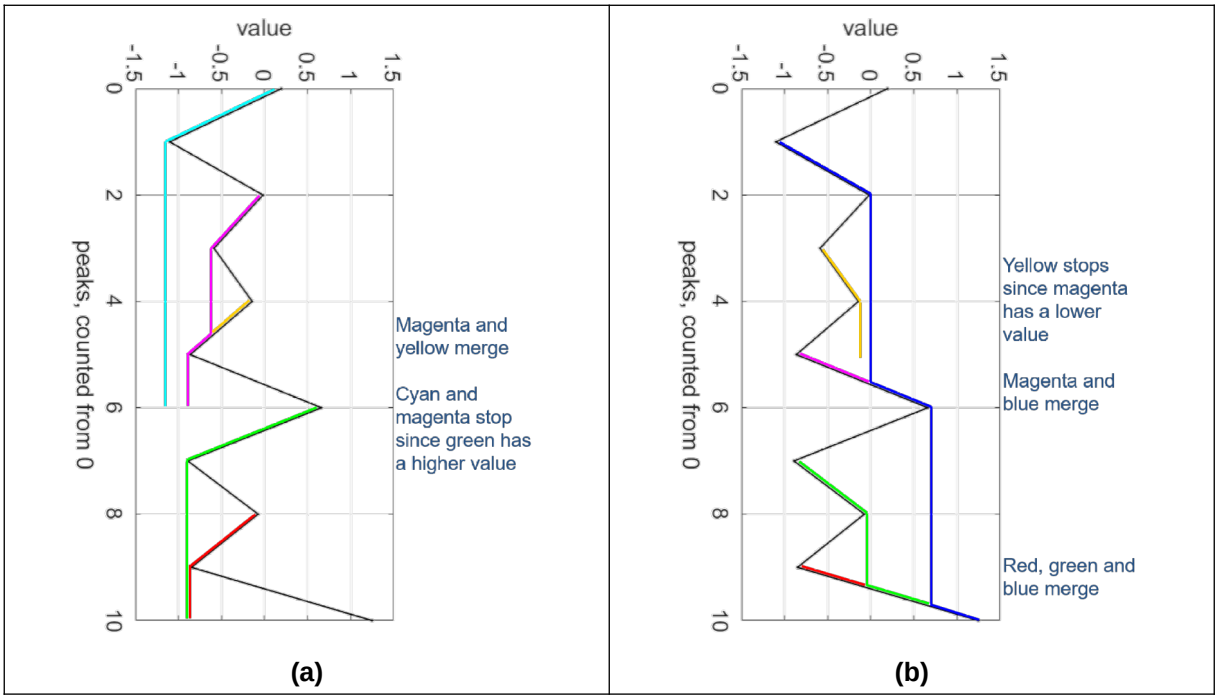

Figure 5.6. Rainflow continuation on the left (a) and right (b) side of the pagoda roof

5. Subsequently, each rainflow is counted as a half loading cycle, and half-cycles with the same magnitude are grouped together. In this example, half-cycles with the same color (from the left and right side each) form a full loading cycle, see Figure 5.7. In case of time histories with a large number of peaks, the grouping of the loading cycles can be conducted in amplitude classes to limit the number of terms in the fatigue damage accumulation as explained in Section 5.6.

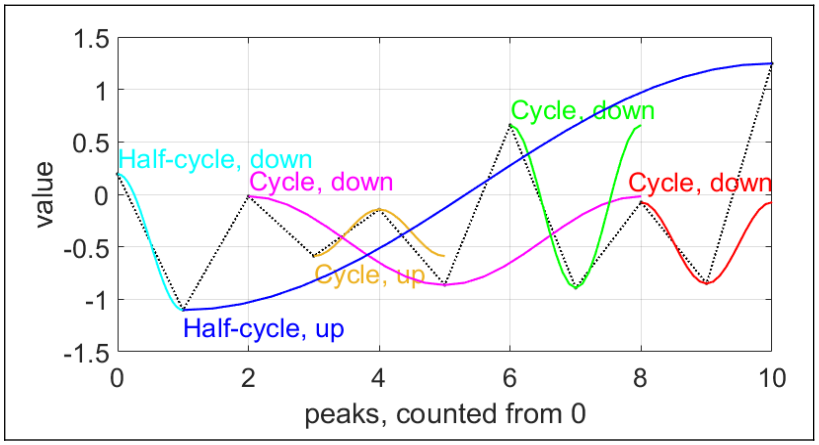

Figure 5.7. Visualization of load cycle generation in rainflow-counting algorithm

The algorithm used in this thesis is developed by Nieslony [68]. With those generated cycles, load collectives – frequencies of occurrence as a function of discrete amplitudes classes – are derived.

5.5 Ground-air-ground cycle

Since ground-air-ground cyclic loads are also relevant for the structure fatigue [70], a simplified ground-air-ground cycle is considered – additionally to the turbulence loads. In this case, the aircraft is assumed to have zero stress on the ground, and the stresses during flight are taken from a reference +1.3g maneuver calculation. The load factor of 1.3 should represent the typical maximum load factor reached in a flight mission, particularly during take-off [25]. This difference between the minimum and maximum load factor during a flight cycle is also what would emerge in the rainflow-counting as the one cycle with the largest amplitude, regardless of other smaller cycles in between. This aspect is visualized by the blue cycle of the stress load factor in an exemplary flight mission in Figure 5.8. As a remark: a stress load factor of zero implies the condition on ground, while peak 1 indicates the maximum load factor of 1.3 during a flight cycle. Furthermore, peak 2 represents the cruise flight, peak 3 and 5 show the load factor during turns, while peak 4 equals the load factor during descent initiation.

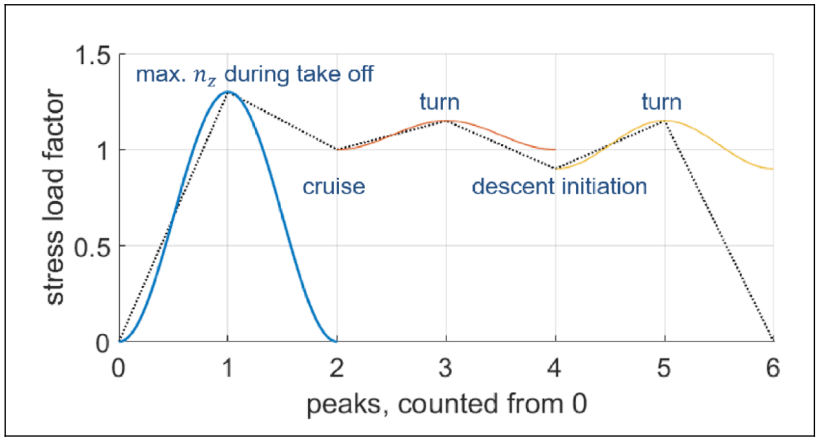

Figure 5.8. Stress cycles during an exemplary flight mission

The focus of the fatigue analysis is the major principal stress on the lower skin of the wing and the HTP. Therefore, landing cases are not considered since large parts of the lower skin are loaded with compressive stress during the impact. Moreover, +1.15g turns – which correspond to 30° bank angle – flown during flight are seen as irrelevant since the load factor fluctuation is only 0.15g, as visible between peak 2 and 4 in Figure 5.8.

For the mass configuration, the aircraft is assumed to have the take-off configuration for the reference mission that is the respective MTOM according to Section 5.1. Table 5.1 defines a trim condition for both reference aircraft that should represent the climb phase. The pitching velocity for the trim calculation is obtained using Equation (3.2). The climb phase is considered instead of the take-off condition since the high-lift systems – that are necessary for take-off at MTOM and change the spanwise lift distribution – are not modeled.

Table 5.1. Parameters of the climb condition

Parameter	Value
Altitude	4572 m (FL150)
Airspeed	181.6 m/s TAS (280 KEAS)
Mach number	0.563
Dynamic pressure	12700 Pa
Load factor	1.3

The MLA deflection of the active aircraft is calculated by:

$$\xi(\bar{q}_{climb}, 1.3\mathrm{g}) = -8° \cdot \frac{\bar{q}_C}{\bar{q}_{climb}} \cdot \frac{1.3\mathrm{g} - 1.0\mathrm{g}}{2.5\mathrm{g} - 1.0\mathrm{g}}, \tag{5.7}$$

with:

ξ : aileron deflection [deg],
$\bar{q}_C$: dynamic pressure at design cruise speed [Pa],
$\bar{q}_{climb}$: dynamic pressure in the climb phase [Pa].

With the dynamic pressure of the climb phase, Equation (5.2) yields -2.5° for both reference aircraft. For the fatigue damage calculation, the stress amplitudes are half of the stresses during the +1.3g maneuver.

5.6 Fatigue damage accumulation

For the linear fatigue damage accumulation, the Palmgren-Miner's rule [18] is applied. With a given S-N (stress-cycle) curve for the respective material and stress ratio, the fatigue damage is accumulated as following:

$$D_F/\mathrm{h} = \sum_i \frac{n_i/\mathrm{h}}{N_i}, \tag{5.8}$$

with:

D_F/h : fatigue damage per hour,
i : index for amplitude classes,
n_i/h : frequency of occurrence of respective amplitude class per hour,
N_i : fatigue life limit of respective amplitude derived from S-N curve.

As an example to Equation (5.8): one loading cycle at a low amplitude causes a different amount of fatigue damage $\frac{1}{N_1}$ compared to one cycle at a high amplitude $\frac{1}{N_2}$. If each of both cycles occur once, the total fatigue damage D_F is the sum of the individual damage values. This operation can be extrapolated to as many different amplitudes with different numbers of cycles each. Furthermore, the Palmgren-Miner's rule states that structural failure is expected to occur when an accumulated fatigue damage of 1.0 is reached. While this method is commonly used for metal fatigue, it is also taken as a first approximation for composite fatigue. The S-N curves used in this thesis are described in Section 6.3 and 7.3.

6 Loads, optimization and fatigue results of D150 configuration

This chapter evaluates the loads, optimization and fatigue results for the D150 configuration. At first, the parameter space considered in the design process is listed. With those parameters, iterative cycles of loads analysis and structural optimization according to the design process workflow described in Section 3.7 are run. The resulting design loads, structural masses and aeroelastic parameters after the final cycle are listed, and a comparison between the active and passive aircraft is given.

The turbulence loads and fatigue analysis follows. It begins with a description of the reference flight mission with its parameters and turbulence intensities. Subsequently, the turbulence loads are calculated for each flight phase and their collectives are derived using the rainflow-counting algorithm. With the load collectives, a first overview of the differences between the active and passive aircraft is gained. The calculations with the continuous turbulence are also conducted for selected structural elements on the lower skin of the wing and HTP, and collectives of the major principal stress are derived. Furthermore, stresses emerging from a reference 1.3g maneuver – that represents a ground-air-ground cycle – are calculated. With those stresses, the collectives for the reference flight cycle are derived, and the fatigue damage values for the active and passive aircraft are calculated with the methodology described in Chapter 5. Subsequently, the differences in the fatigue behavior between the active and passive aircraft are discussed.

6.1 Parameter space for loads analysis and structural optimization

This section begins with an overview of the parameter space for the loads analysis that comprises the mass configurations, flight conditions as well as gust and maneuver cases considered in the simulations. Subsequently, the parameters set in the structural optimization comprising the objective function, design variables and constraints are explained.

6.1.1 Mass configurations

According to CS25.321, load calculations have to be conducted for a representative number of mass configurations between the design minimum and maximum mass while covering the whole design envelope [20]. Theoretically, a large number of mass cases has to be taken into account (>>100) to cover the design mass envelope adequately while taking various mass distributions into account. For this thesis however, the number of mass configurations considered in the loads analysis is set to nine to limit the computational effort for the loads analysis. The mass cases are defined so that they cover the whole range between the empty and maximum take-off mass with a large range for center of gravity (CG) locations. As a comparison: Klimmek [54] covered the mass and balance envelope using four mass

configurations. However, since dynamic loads are considered in this thesis and they are expected to be more sensitive to changes in the mass configuration, nine mass cases are considered as adequate:

- one operating empty mass (OEM) case,
- two lightly loaded cases, each one for the forward and rear CG position,
- three heavy payload cases: forward and rear CG as well as one with middle CG at the maximum zero fuel mass (MZFM),
- three maximum take-off mass (MTOM) cases resulting from the heavy payload cases with fuel masses added.

Figure 6.1 and Table 6.1 show an overview of the mass cases. They are labeled according to Pinho Chiozzotto [72].

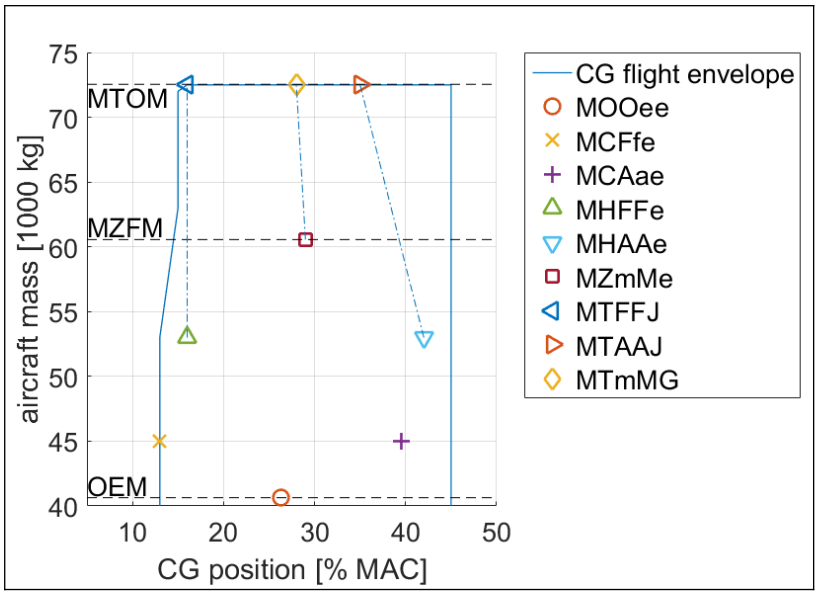

Figure 6.1. Mass and balance diagram of considered configurations – D150

Table 6.1. Overview of the mass configurations – D150

Label	Mass [kg]	CG [% MAC]	Notes
MOOee	40638	26.3	Operating empty mass
MCFfe	45000	13.0	Forward CG, light payload
MCAae	45000	39.5	Rear CG, light payload
MHFFe	52988	16.0	Forward CG, heavy payload
MHAAe	52988	42.0	Rear CG, heavy payload
MZmMe	60548	29.0	Middle CG, maximum zero fuel mass
MTFFJ	72507	16.0	MHFFe with 19.5 t fuel
MTAAJ	72507	35.0	MHAAe with 19.5 t fuel
MTmMG	72507	28.0	MZmMe with 12.0 t fuel

6.1.2 Flight conditions within the design envelope

Beside the mass configurations, the definition of flight conditions for the loads analysis is also necessary. To limit the number of simulations, the considered flight conditions consist of three selected altitudes and the respective airspeeds V_A, V_C and V_D. While the design cruise speed V_C and the design dive speed V_D are defined during the aircraft specification, the maneuvering speed V_A needs to be derived first. Assuming that the aircraft has the minimum dynamic pressure to perform a 2.5g pull-up maneuver at MTOM at the reference V_A using a maximum lift coefficient of 1.4, V_A is calculated by:

$$V_A = \sqrt{\frac{2 \cdot n_z \cdot m_{MTO} \cdot g}{c_{L.max} \cdot S \cdot \rho}}, \tag{6.1}$$

with:

V_A : reference maneuvering speed [m/s],
n_z : maneuver load factor, set to 2.5 [-],
m_{MTO}: maximum take off mass [kg],
g : gravitational acceleration [m/s²],
$c_{L,max}$: maximum incompressible lift coefficient, set to 1.4 [-],
S : wing reference area [m²],
ρ : air density [kg/m³].

Previous studies show that the largest gust loads on the wing are reached at V_C between sea level and approximately 7000 m [34]. The latter is the altitude where the design cruise speed equals the design cruise Mach number: $Z(V_C = M_C)$ and above which the Mach number M_C is the constraining factor instead of the airspeed V_C. Hence, only flight conditions at V_C between sea level and $Z(V_C = M_C)$ are considered for the gust loads analysis. As a remark: V_C is not necessarily equal to the economic cruise Mach number.

For the maneuver loads analysis, the aim of the flight condition definition is to cover the envelope of the dynamic pressure and Mach number. This is achieved by taking airspeeds from V_A to V_D and altitudes from sea level to $Z(V_C = M_C)$ into account. At V_A, the aircraft has the minimum dynamic pressure to perform 2.5g pull-up maneuvers, and it reaches the maximum dynamic pressure at V_D. Flight conditions at sea level correlate with relatively low Mach numbers, while the highest Mach numbers can be flown at approximately $Z(V_C = M_C)$ and above. To further reduce the number of simulations, altitudes above $Z(V_C = M_C)$ are neglected. Figure 6.2 and Table 6.2 give an overview of the considered flight conditions in the simulations. The labels are also based on Pinho Chiozzotto [72].

Table 6.2. Overview of the flight conditions – D150

Altitude [m]	V_A [m/s TAS]	Label	V_C [m/s TAS]	Label	V_D [m/s TAS]	Label
0	129.9	OA000	180.0	OC000	205.6	OD000
3000	150.8	OA100	208.9	OC100	234.5	OD100
7000	187.2	OA230	256.0	OC230	277.9	OD230

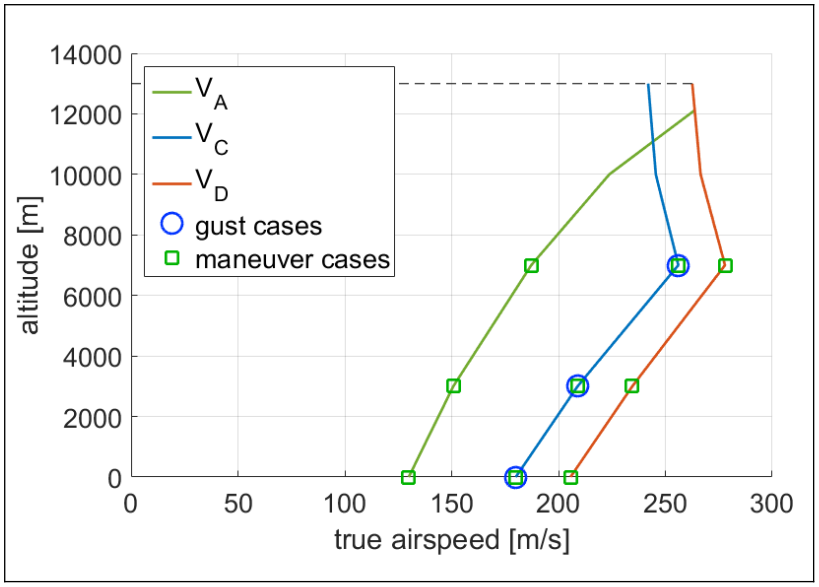

Figure 6.2. Flight conditions in the design envelope – D150

6.1.3 Gust load conditions

For the 1-cos gust loads analysis according to CS25, the aircraft is assumed to encounter symmetric, vertical gusts during level flight. The gust shape is defined by:

$$U(x) = \frac{U_{ds}}{2}\left(1 - cos\left(\frac{\pi x_g}{H}\right)\right), \tag{6.2}$$

with:

$U(x)$: gust shape [m/s],
U_{ds} : design gust speed [m/s],
x_g : distance penetrated into the gust [m],
H : gust gradient [m].

For the load calculation, sufficient gust gradients ranging from 9 m to 107 m (30 ft to 350 ft) must be investigated in dynamic simulations. The design gust speed is a function of the altitude and the gust gradient [20] as defined by:

$$U_{ds} = U_{ref} \cdot F_g \left(\frac{H}{107\ \mathrm{m}}\right)^{\frac{1}{6}}, \tag{6.3}$$

with:

U_{ds} : design gust speed [m/s],
U_{ref} : altitude dependent reference gust speed [m/s],
F_g : altitude dependent profile alleviation factor [m/s],
H : gust gradient [m].

The gust profile alleviation factor F_g is defined to be 1.0 at the maximum operating altitude, and it decreases linearly to the value at sea level calculated by:

$$F_g(Z = 0\ \mathrm{m}) = 0.5 \cdot (F_{gz} + F_{gm}), \tag{6.4}$$

with:

$$F_{gz} = 1 - \frac{Z_{MO}}{76200\ \mathrm{m}}, \tag{6.5}$$

$$F_{gm} = \sqrt{R_2 \cdot \tan(\frac{\pi R_1}{4})}, \tag{6.6}$$

and:

$$R_1 = \frac{m_{ML}}{m_{MTO}}, \tag{6.7}$$

$$R_2 = \frac{m_{MZF}}{m_{MTO}}, \tag{6.8}$$

with:

Z : altitude [m],
Z_{MO} : maximum operating altitude [m],
m_{ML} : maximum landing mass [kg],
m_{MTO}: maximum take-off mass [kg],
m_{MZF}: maximum zero fuel mass [kg].

In this thesis, a total of seven gust gradients are considered. Figure 6.3 illustrates the gust profiles with a reference gust speed of 17.07 m/s and a profile alleviation factor of 1.0, and Table 6.3 lists the corresponding gust gradients.

Table 6.3. Overview of the gust gradients

Gust number	1	2	3	4	5	6	7
Gust gradient [m]	9	15	30	46	61	76	107

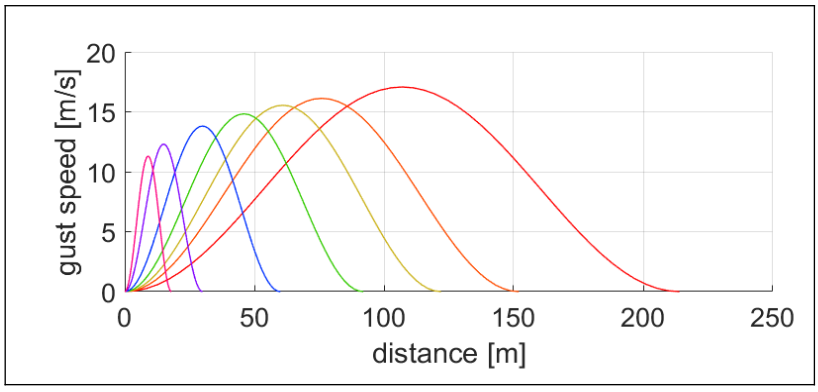

Figure 6.3. Overview of the 1-cos gust profiles

With nine mass configurations, three altitudes, seven gust gradients and two gust directions – vertical upward and downward – each, there are 378 gust cases that are considered in the loads analysis.

6.1.4 Maneuver load conditions

For the maneuver loads analysis at the flight conditions stated in Table 6.2, symmetrical 2.5g pull-up and -1g push-down maneuvers are taken into account. According to the V-n diagram defined in CS25.333 [20], the +2.5g pull-up is to be investigated between V_A and $V_{D,}$ while the -1g push-down has to be considered between V_H to $V_{C.}$ V_H is the stall speed when performing a -1g push-down. However, to simplify the airspeed calculations, V_H is assumed to have the same value as V_A. Besides, to further reduce the number of load cases, only the edges of the maneuvering envelope are considered at every altitude; those are +2.5g pull-up at V_A and V_D as well as -1g push-down at V_A and V_C. Figure 6.4 illustrates the considered maneuver cases that are investigated for every altitude. With nine mass configurations, three altitudes and four maneuvers each, there are 108 maneuver cases considered in the loads analysis.

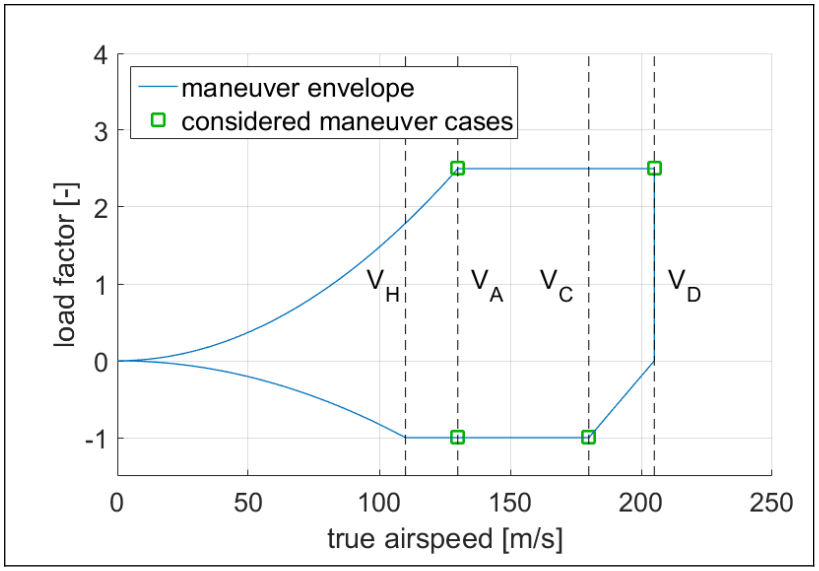

Figure 6.4. Considered maneuver cases in an exemplary V-n diagram

6.1.5 Overview of the optimization task

After the simulations with the parameters described in the Subsections 6.1.1 to 6.1.4 and the post-processing according to Section 3.3, the loads are fed into the structural optimization. The objective of the optimization task lies in minimizing the structural mass while complying with the constraints described in Subsection 6.1.6.

On the D150 configuration, every skin area between two ribs, spar area between two ribs and every rib is counted as one design field each. The term design field implies that the design variable is constant in the respective area. The design variable in every design field is the material thickness. The optimization process is conducted separately for each component (wing and HTP). Moreover, only the starboard half of the wing box and HTP box is included in the optimization, and the resulting properties are then mapped onto the port half on the respective component. With 30 ribs in a wing box half, there are 146 design fields for the wing. An HTP half has 14 ribs and a total of 66 design fields.

6.1.6 Constraints in the structural optimization

The constraints considered in the structural optimization are von-Mises stress, buckling stability and minimum thickness. With an ultimate strength σ_{ult} of 441 MPa for aluminum and a safety factor of 1.5, a limit von-Mises stress σ_{lim} of 294 MPa is taken into account in the structural optimization. The calculation of von-Mises stress is defined by:

$$\sigma_m = \left({\sigma_{xx}}^2 + {\sigma_{yy}}^2 - \sigma_{xx}\sigma_{yy} + 3{\tau_{xy}}^2\right)^{\frac{1}{2}}, \tag{6.9}$$

where:

σ_m : von-Mises stress [Pa],
σ_{xx} : tensile stress in x-direction [Pa],
σ_{yy} : tensile stress in y-direction [Pa],
τ_{xy} : shear stress [Pa].

For buckling stability analysis, the skin fields of the wing are assumed to be sized by compressive buckling, while the spars and ribs are sized by shear buckling [54]. In the optimization, the buckling phenomenon is simplified into a two-dimensional buckling by assuming the buckling fields to be infinitely long plates with a certain width. The width of the buckling field is set to 15 cm which represents the average distance between two stringers.

With the buckling field material thickness, bending stiffness and width, the allowable compressive stress is calculated by:

$$\sigma_{bc} = \frac{\pi^2 k_c E}{12(1-\nu^2)} \left(\frac{t}{b}\right)^2, \tag{6.10}$$

with:

σ_{bc} : compression buckling stress [Pa],
k_c : compression buckling coefficient [-],
E : tensile modulus [Pa],
ν : Poisson ratio [-],
t : material thickness [m],
b : buckling field width [m].

With the assumption that the buckling field has an infinite aspect ratio and the edges are simply supported, the compressive buckling coefficient k_c is set to 4.0. This value represents the lower boundary of the coefficient as shown e.g. by Timoshenko et al. [93] p. 353. To fulfill the buckling constraint, the present minor principal stress has to be smaller in magnitude than the buckling stress.

The allowable shear stress is calculated by:

$$\tau_{bs} = \frac{\pi^2 k_s E}{12(1-\nu^2)} \left(\frac{t}{b}\right)^2, \tag{6.11}$$

with:

τ_{bs} : shear buckling stress [Pa],
k_s : shear buckling coefficient [-],

E : tensile modulus [Pa],
ν : Poisson ratio [-],
t : material thickness [m],
b : buckling field width [m].

The shear buckling coefficient can be taken from diagrams that are shown e.g. by Timoshenko et al. [93] p. 383. In the structural optimization, the maximum shear stress in every element must be smaller than the allowable shear buckling stress.

For the minimum thickness, a value of 2 mm is selected for every design field. Furthermore, a constraint concerning the aileron effectiveness is considered. In this case, the aileron effectiveness $\frac{c_{l\xi}(\text{elastic})}{c_{l\xi}(\text{rigid})}$ has to be positive at V_D/M_D+15% as explained in Section 3.5.

6.2 Comparison of design loads, structural masses and aeroelastic parameters

With the parameters described in Section 6.1, the process explained in Section 3.7 is run. The resulting design loads, structural masses and aeroelastic parameters are elaborated in the following subsections.

6.2.1 Design loads

Figure 6.5 visualizes the resulting wing bending moment envelopes of the passive aircraft after ten cycles of loads analysis and structural optimization, while Figure 6.6 shows the respective envelopes of the active aircraft. It is apparent that maneuvers evoke the largest bending moment M_x on both aircraft, whereas the active aircraft has 6.2% less wing root bending moment. At the outer section (y=11 m) the reduction of wing bending moment due to maneuver is 18.4%. The gust loads generate 10.7% less bending moment at the root of the active aircraft, whereas a decrease by 21.0% results at the outer section. Judging by the bending moment of the active aircraft alone, it is plausible to assume that the MLA could be set more aggressively to match the levels of the gust loads. At this point however, it has to be checked whether larger MLA deflections are still aerodynamically feasible – especially at high Mach numbers. If they are feasible, the additional reduction of the bending moment will come together with a further increase in torsion as shown in the next paragraphs. In the worst case, the increase in torsion due to a more aggressive MLA would lead to heavier system and structural masses.

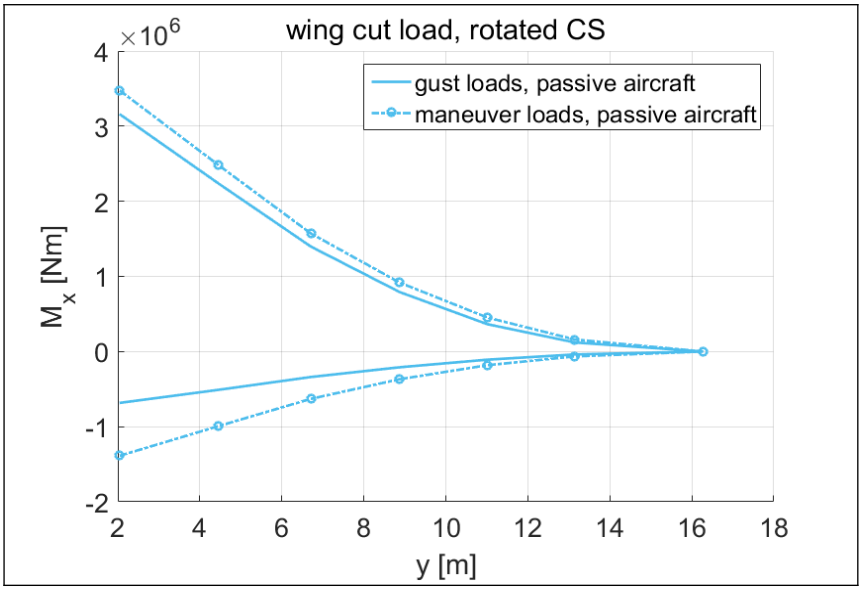

Figure 6.5. Wing bending moment of passive D150

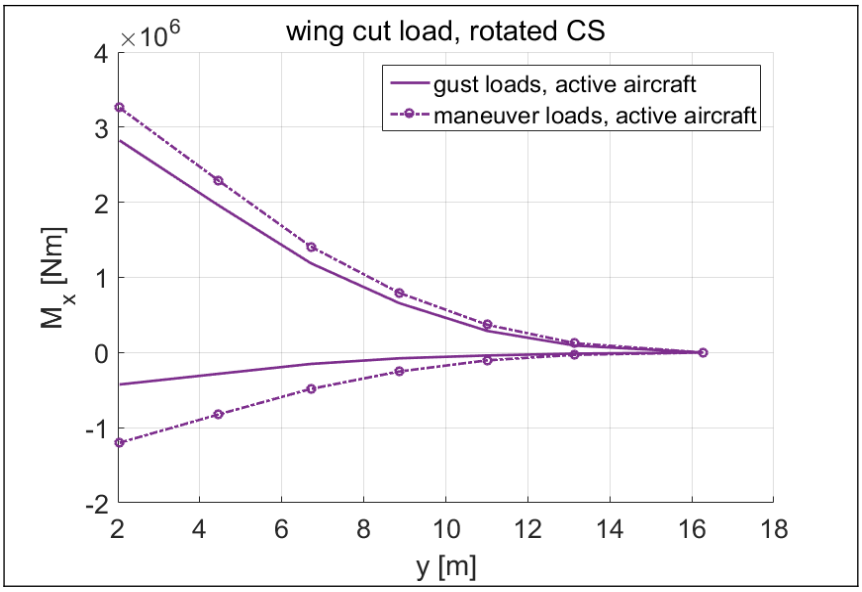

Figure 6.6. Wing bending moment of active D150

While the 1D envelopes of Figure 6.5 and Figure 6.6 give an insight into the global trend of the cut loads, 2D envelopes provide an overview of the correlation between the load components at the respective positions. For this aim – also for the analysis of turbulence loads – three reference monitoring stations at the wing root, wing outer section and the HTP root with the respective local coordinate systems are defined, see Figure 6.7.

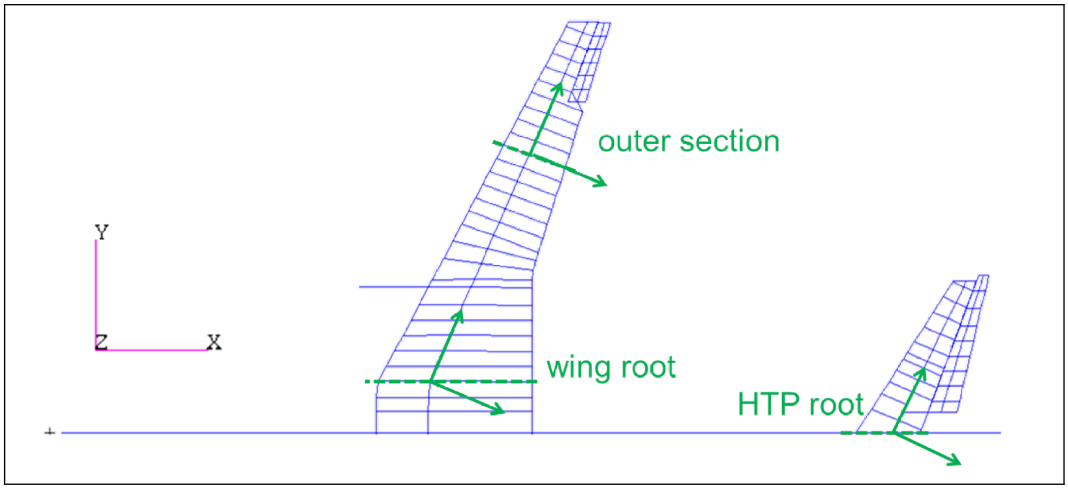

Figure 6.7. Selected cut load monitoring stations on D150

Figure 6.8 visualizes 2D load envelopes of the wing. It is apparent that the envelopes of the active aircraft are rotated counter-clockwise in general, it means that the maximum bending moment M_x is reduced compared to the passive aircraft, however an increase in the torsion M_y is noticeable. At the outer section, the maximum torsion increases by 12.1%. At the root, the increase in maximum torsion is 15.9%, whereas the magnitude of the minimum torsion decreases by 5.2%. However, the rotation of the envelope is however not as clearly visible as at the outer section. This is caused by the engine – that contributes to the loads at the root – evoking large torsion due to its large lever between its CG and the wing's LRA.

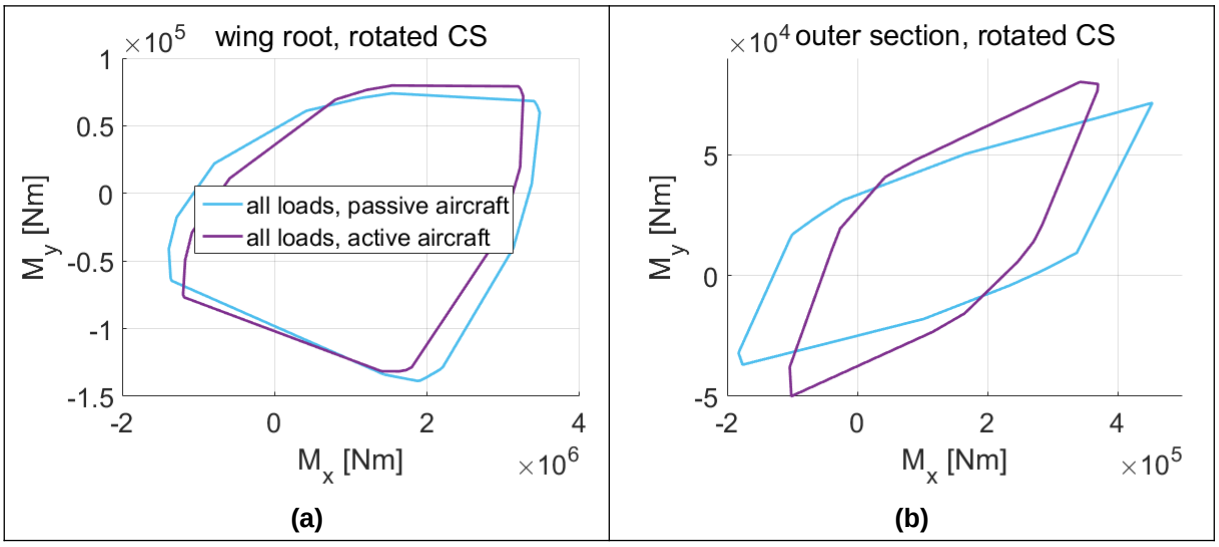

Figure 6.8. 2D load envelope comparison on D150

The maximum bending moment and torsion on the wing is reached during maneuvers, predominantly with the mass configuration MTFFJ (MTOM with forward CG, Table 6.1). Moreover, the gust loads generally cause the envelopes to become rounder while the maneuver loads form a narrow band, see Figure A-1(a) in the Appendix. With the load case selection algorithm described in Section 3.3, the number of load cases for the structural optimization ranges between 51 and 62.

Concerning the aileron hinge moments, the passive aircraft shows a maximum magnitude of 3152 Nm during design maneuvers, while the active aircraft has to withstand moments up to 3355 Nm during design gust encounters which is 6.4% higher. In this case, the actuators of the active aircraft have to be slightly reinforced with regards to maximum torque.

6.2.2 Structural masses

Figure 6.9 shows the convergence history of the D150 wing box mass. However, the mass convergence alone does not always guarantee a convergence of the skin thicknesses on each design field. To quantify the latter in a number, the RMS of the relative change in material thicknesses between each cycle is calculated. This operation is expressed by:

$$rms_{\Delta t}(j_c) = \sqrt{\frac{1}{n_d}\sum_{j_d=1}^{n_d}\left(\frac{t_{j_d,j_c} - t_{j_d,j_c-1}}{t_{j_d,j_c}}\right)^2}, \tag{6.12}$$

with:

$rms_{\Delta t}$: root mean square of the change in material thickness between two cycles,
j_c : counting variable for the cycle of loads analysis and structural optimization,
n_d : number of design fields,
j_d : counting variable for the design fields,
t : material thickness.

Figure 6.10 shows the results.

After ten cycles of loads analysis and structural optimization, the wing box of the active aircraft is 2.8% or 90 kg lighter compared to the passive aircraft. Concerning the material thickness convergence, the RMS values of thickness change between the last two cycles are 1.37% for the passive and 1.11% for the active aircraft.

In a loads and optimization process using static loads as demonstrated by Klimmek [54], the wing box mass does not significantly change after three cycles. In this thesis however, the convergence of the wing box mass is slower. This is caused by the number of load cases and their selection algorithm:

- In total there are 108 quasi-steady maneuver and 378 dynamic gust cases considered to calculate loads for the structural optimization.
- Before the optimization step, a new load case selection is conducted in every cycle. Thus, the composition of load cases considered in the optimization step varies between the cycles. In combination with the large number of load cases, an optimization with the currently selected load cases may cause others to emerge as critical in the next cycle.

Apart from those aspects, a decrease in wing box mass also reduces the wing stiffness. Due to the bending-torsion-coupling of backward swept wings, the lower wing stiffness in turn reduces the loads. This results in a decrease in wing box mass again in the next cycle. This phenomenon contributes to the slower convergence of backward swept wing configurations compared to forward swept ones, as shown in Subsection 7.2.2.

During an aircraft design process however, a convergence in the structural optimization cannot be striven to the last kilogram. The reason is: if a minor modification resulted in a change in e.g. the secondary mass in a late stage, the entire loads analysis and structural optimization procedure would have to be conducted again – which is not affordable. Therefore, at a certain point of the design process, the structural layout is frozen and the target loads are defined [95]. All following loads analyses are then mainly run to verify that the results stay below those target loads.

The wing box masses shown in Figure 6.9 refer only to ideal load-carrying masses. Additional masses due to joints, fasteners, access holes and their reinforcements are not considered. According to Pinho Chiozzotto [71], an empirical mass factor of 1.45, that is multiplied with the obtained wing box masses, delivers a reliable estimate for the total wing box mass. Hence, with a mass factor of 1.45, the wing mass difference between the active and passive aircraft would be 1.45·90 kg = 130.5 kg, assuming that the secondary masses comprising the systems remain unchanged.

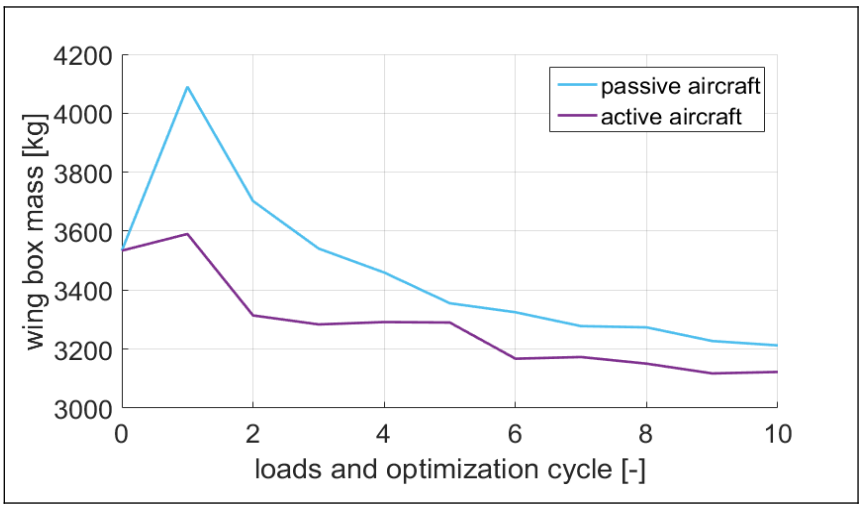

Figure 6.9. Wing box mass trend in the loads and optimization process of D150

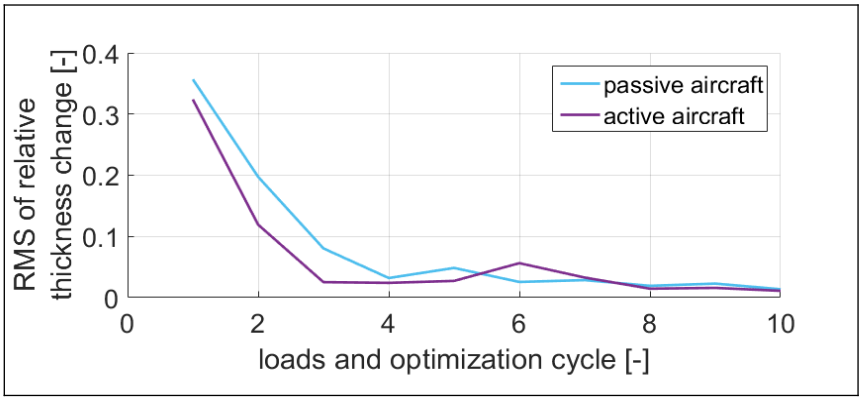

Figure 6.10. RMS of material thickness change of D150 wing box

Figure 6.11 visualizes the difference of 2.8% in the wing box mass. Judging by the load envelopes in Figure 6.8, the mass decrease of the active aircraft is explained by the lower wing bending moment M_x. On the upper skin of the passive aircraft, the area with a thickness around 6.5 mm in the middle wing section is larger compared to the active aircraft. On the lower skin, a larger patch with thicknesses around 5.0 mm is visible on the passive aircraft. Near the wing root, the lower skin of the passive aircraft is approx. 0.2 mm thicker which is also explained by the higher wing bending moment compared to the active aircraft. Near the wing tip, the area with the minimum thickness on the lower skin of the passive aircraft is also smaller. On the other hand, the spars and ribs have similar thicknesses. On the HTP, there is hardly any difference between the active and passive aircraft, as Figure 6.12 shows, and the mass difference between both HTP boxes is below 1 kg.

Concerning the structural dynamics, Table A-1 in the Appendix lists the frequencies of several selected modes. The wing mode frequencies of the active aircraft are up to 2% lower compared to the passive counterpart, otherwise the differences are negligible.

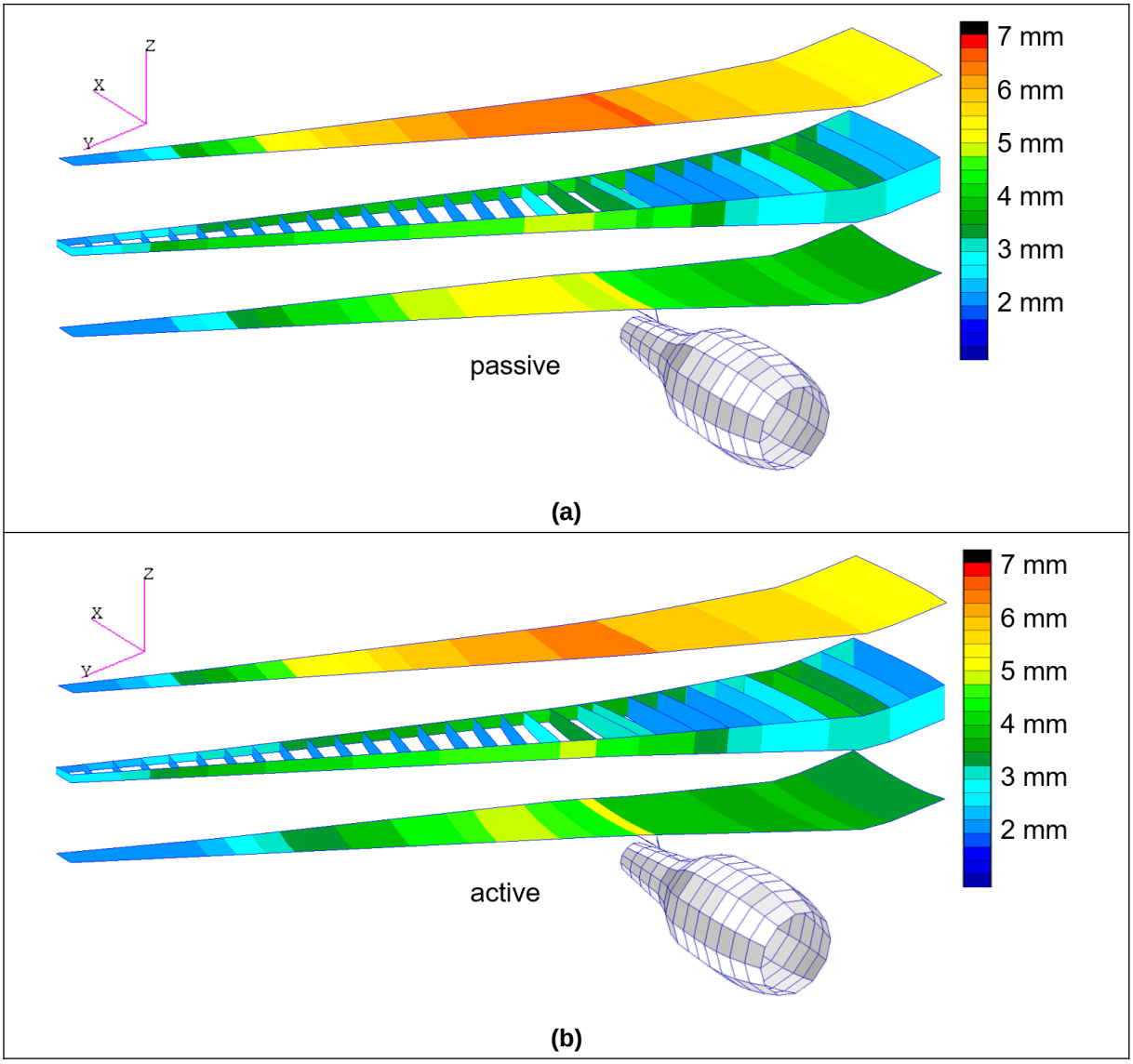

Figure 6.11. Wing material thickness distribution of D150

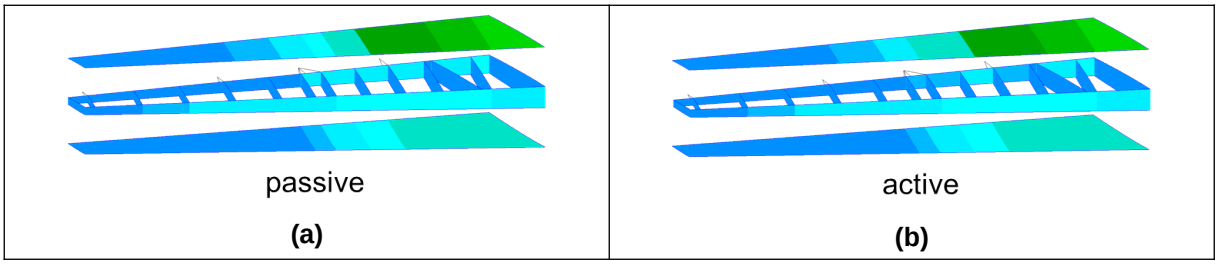

Figure 6.12. HTP material thickness distribution of D150

6.2.3 Aeroelastic parameters

According to CS25.629, aeroelastic stability calculations have to be conducted in the whole flight envelope and with speeds up to V_D+15%. Figure 6.13 shows the aeroelastic stability envelope for the D150 configuration. The investigated aeroelastic stability requirements comprise the aileron effectiveness and the flutter speed.

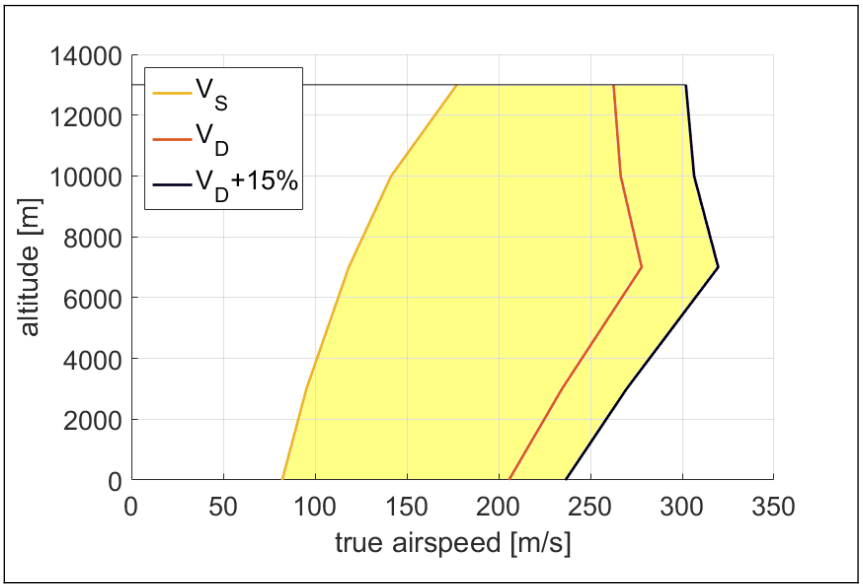

Figure 6.13. Design envelope for aeroelastic stability of D150

Aileron effectiveness

Since aileron effectiveness problems occur at high dynamic pressures, the speed V_D+15% is considered. Furthermore, with DLM aerodynamics, an increase in altitude only results in an increase in the Mach number and thus a magnification of stability and control derivatives since no transonic effects are considered. Therefore, the altitude is set to sea level. This flight condition yields parameters listed in Table 6.4.

Table 6.4. Parameters of aileron effectiveness calculation on D150

Parameter	Value
Mach number	0.6948
Air density	1.225 kg/m³
Dynamic pressure	34240 Pa

The flight mechanic derivative monitored in this analysis is the rolling moment coefficient due to aileron deflection $c_{l\xi}$. In this case, the derivative of the elastic aircraft $c_{l\xi}(\mathrm{elastic})$ is compared to that of the rigid aircraft $c_{l\xi}(\mathrm{rigid})$ and the ratio is the defined aileron effectiveness. The mathematical formulation of the aileron effectiveness is shown in Equation (3.8) and Table 6.5 shows the results of aileron effectiveness analysis of the D150 configuration.

Table 6.5. Aileron effectiveness values of D150

Aircraft model	Aileron effectiveness value
Passive aircraft	0.131
Active aircraft	0.101

With both values being positive, no aileron reversal occurs at any speed up to V_D+15%. However, the active aircraft has a lower aileron effectiveness value since the wing material thickness is generally lower than for the passive aircraft, hence the wing stiffness is also lower. Nevertheless, no modification is needed to comply with the static aeroelastic requirements.

Flutter speed

Another aeroelastic parameter to compare between the active and passive aircraft is the flutter speed. For this aim, a subsonic flutter calculation is conducted using MSC.Nastran. Table 6.6 lists the parameters for the reference flight condition in the flutter calculation. The reference Mach number is set to the equivalent of V_D at sea level to achieve a subsonic reference flow condition, and the air density is set accordingly. The selection of the Mach number is based on the assumption that transonic flow conditions emerge at Mach 0.7. Moreover, the 50 Eigenmodes included in the calculation are assumed as sufficient since the potential flutter-critical modes such as the first wing torsion, the second and third wing bending as well as HTP torsion and bending are included. As derived in Section 2.3, a maximum reduced frequency of 3.0 is considered.

Table 6.6. Parameters of flutter calculation on D150

Parameter	Value
Reference Mach number	0.6042
Air density	1.225 kg/m³
Number of Eigenmodes	50
Considered reduced frequencies	0.01 to 3.0 with 300 sampling points

Figure 6.14 shows the damping curves of the flutter mode, and Figure 6.15 visualizes the dominant vacuum mode shape involved in the flutter mode which is the symmetric HTP torsion. This dominant mode shape is identified through a manual mode tracking toward the low speeds of the frequency curve where no more changes in the mode sequence occur.

Complete diagrams of the damping and frequency curves are attached in Figure A-2 in the Appendix. As mentioned in Section 3.6, no complex flutter modes corresponding to the flutter curves can be obtained using the KE-method.

In Figure 6.14, a threshold line at -3% structural damping is drawn (a critically damped system has a structural damping value of 200% [66]). Since the flutter calculation with the KE-method does not consider structural damping and a value of 3% may be taken into account, the aircraft is assumed to flutter if a damping curve passes the -3% line. It is apparent that the flutter speed is significantly higher than V_D+15%. Hence, there is no risk of flutter in the subsonic regime. Besides, there is almost no difference in the flutter speeds of the active and passive aircraft. At the flutter points, the flutter frequencies of both aircraft range between 17.6 and 17.8 Hz.

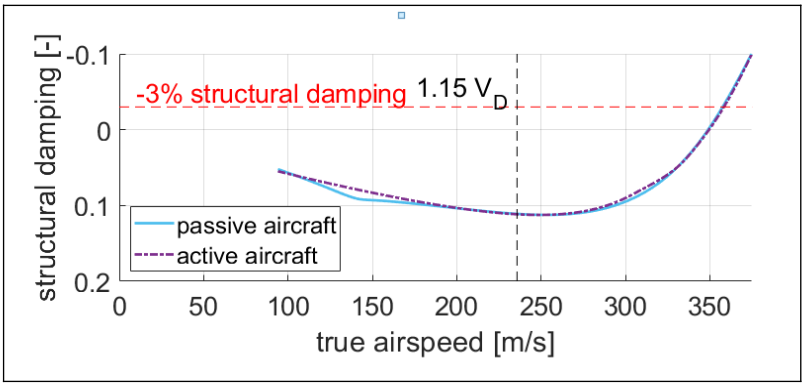

Figure 6.14. Curves of the flutter point of D150

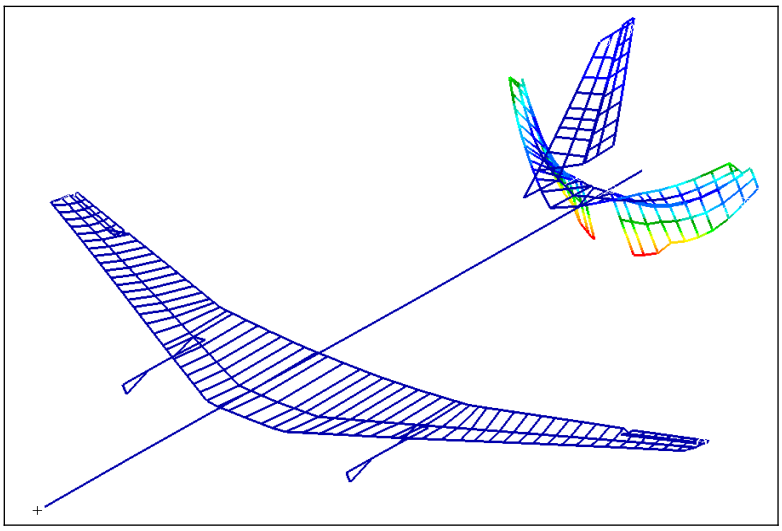

Figure 6.15. Dominant Eigenmode involved at the flutter speed of D150

6.3 Turbulence loads and fatigue analysis

This section begins with a listing of the parameters of the reference flight mission considered in the turbulence loads and fatigue calculations. With these parameters, cut load and stress collectives caused by the atmospheric turbulence are calculated. Furthermore, stresses due to a ground-air-ground cycle are also taken into account. Using reference S-N curves, the total fatigue damage values for one flight cycle are derived. The resulting differences between the active and passive aircraft are then discussed.

6.3.1 Reference parameters

According to the considerations in Section 5.1, Table 6.7 defines the selected flight mission for the D150 configuration.

Table 6.7. Reference flight route and masses for D150

Parameter	Value
Origin	Berlin Tegel (EDDT)
Destination	Porto (LPPR)
Great circle distance	2076 km
Zero fuel mass	60548 kg
Take-off fuel	10450 kg
Trip fuel	7736 kg
Take-off mass	70998 kg
Landing mass	63262 kg

The payload considered is taken from the mass configuration MZmMe in Table 6.1 that brings the empty aircraft to MZFM. Table 6.8 lists the derived reference flight conditions for the turbulence and fatigue analysis. The altitude for the reference climb phase is set larger than 10000 ft (3048 m) to be able to have airspeeds higher than 250 kts EAS (128.6 m/s EAS) without air traffic control (ATC) permission. The selection of the high airspeed is intended to evoke large turbulence loads. For the reference descent, the airspeed is set to 250 kts EAS and the altitude to 4000 ft (1219 m) that is assumed to be the lowest altitude before the deceleration for the final approach is initiated. The combination of the airspeed and the altitude during descent is expected to induce large turbulence loads. Figure 6.16 visualizes the reference flight mission and the altitudes of the reference flight phases are marked. Table 6.9 lists the parameters for the reference ground-air-ground cycle as described in Section 5.5.

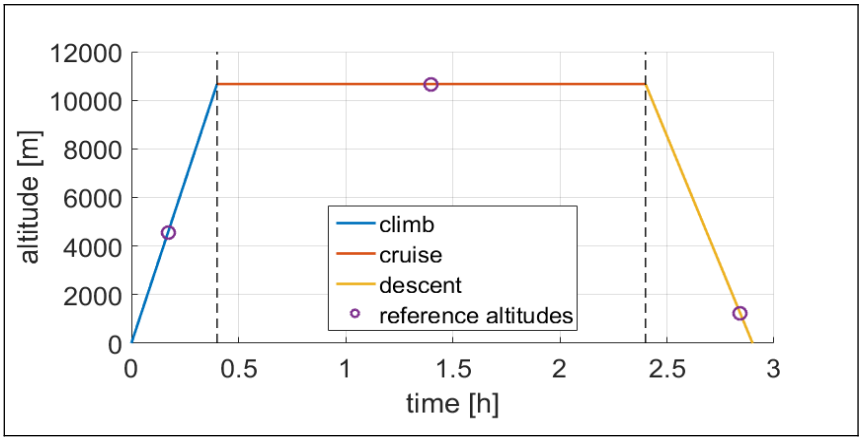

Figure 6.16. Visualization of the reference flight mission of D150

Table 6.8. Reference parameters for each flight phase – D150

Flight phase	Reference parameter	Value
Climb	Altitude	4572 m (FL150)
	Airspeed	181.6 m/s TAS (280 kts EAS)
	Fuel mass	10086 kg
	Turbulence RMS	2.743 m/s TAS
	Duration per flight	0.4 hours
Cruise	Altitude	10668 m (FL350)
	Airspeed	231.3 m/s TAS (Mach 0.78)
	Fuel mass	6456 kg
	Turbulence RMS	1.372 m/s TAS
	Duration per flight	2.0 hours
Descent	Altitude	1219 m (FL 040)
	Airspeed	136.5 m/s TAS (250 kts EAS)
	Fuel mass	2826 kg
	Turbulence RMS	3.048 m/s TAS
	Duration per flight	0.5 hours

Table 6.9. Reference parameters for the ground-air-ground cycle – D150

Reference parameter	Value
Altitude	4572 m (FL150)
Airspeed	181.6 m/s TAS (280 kts EAS)
Fuel mass	10450 kg
Load factor	1.3
MLA deflection (active aircraft)	-2.5°

6.3.2 Cut load and stress collectives

Figure 6.7 shows the monitoring stations observed in the turbulence analysis. Figure 6.17 visualizes the selected structural shell elements for the fatigue analysis. A comparison between the elements at the wing root, outer section and HTP is seen as relevant in gaining insight into the fatigue behavior at different positions of the aircraft structure.

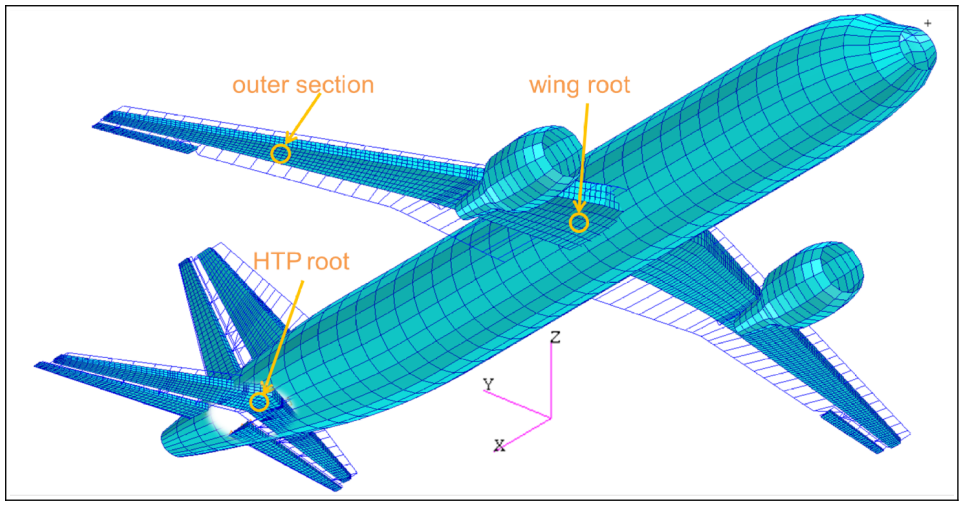

Figure 6.17. Selected structure elements for strain response of D150

To discuss the differences in the turbulence loads between the active and passive aircraft, the climb phase is chosen since it provides higher levels of loads compared to the cruise phase due to the turbulence RMS value and high equivalent airspeed, see Table 6.8. The wing cut load collectives of Figure 6.18(a) to (d) show that the active aircraft experiences smaller amplitudes of bending moment M_x, while the torsion amplitudes M_y are larger, analogous to the differences in the design loads. The largest difference between both aircraft is found in the bending moment M_x at the outer section, where the maximum amplitude experienced by the active aircraft is 41% lower compared to the passive aircraft. This occurs due the fact that the aileron covers a larger percentage of area monitored at the outer section compared to that monitored at the root – analogous to the effects of load alleviation on design loads. Hence, the change of lift from the load alleviation using the aileron has a larger relative contribution to the cut loads at the outer section of the wing. On the HTP however, there are no significant differences in the loads between the active and passive aircraft, see Figure 6.18(e) and (f).

Furthermore, Schwochow [87] states that the symmetrical deflection of ailerons on ATTAS (VFW-614) evokes large lateral accelerations on the engines. On that aircraft, the engines are attached above the wing and the lateral accelerations are mainly caused by the wing bending. On the D150 configuration, the engines are attached underneath the wing, however they can still be affected by wing bending movements. Section 6.4 addresses this aspect.

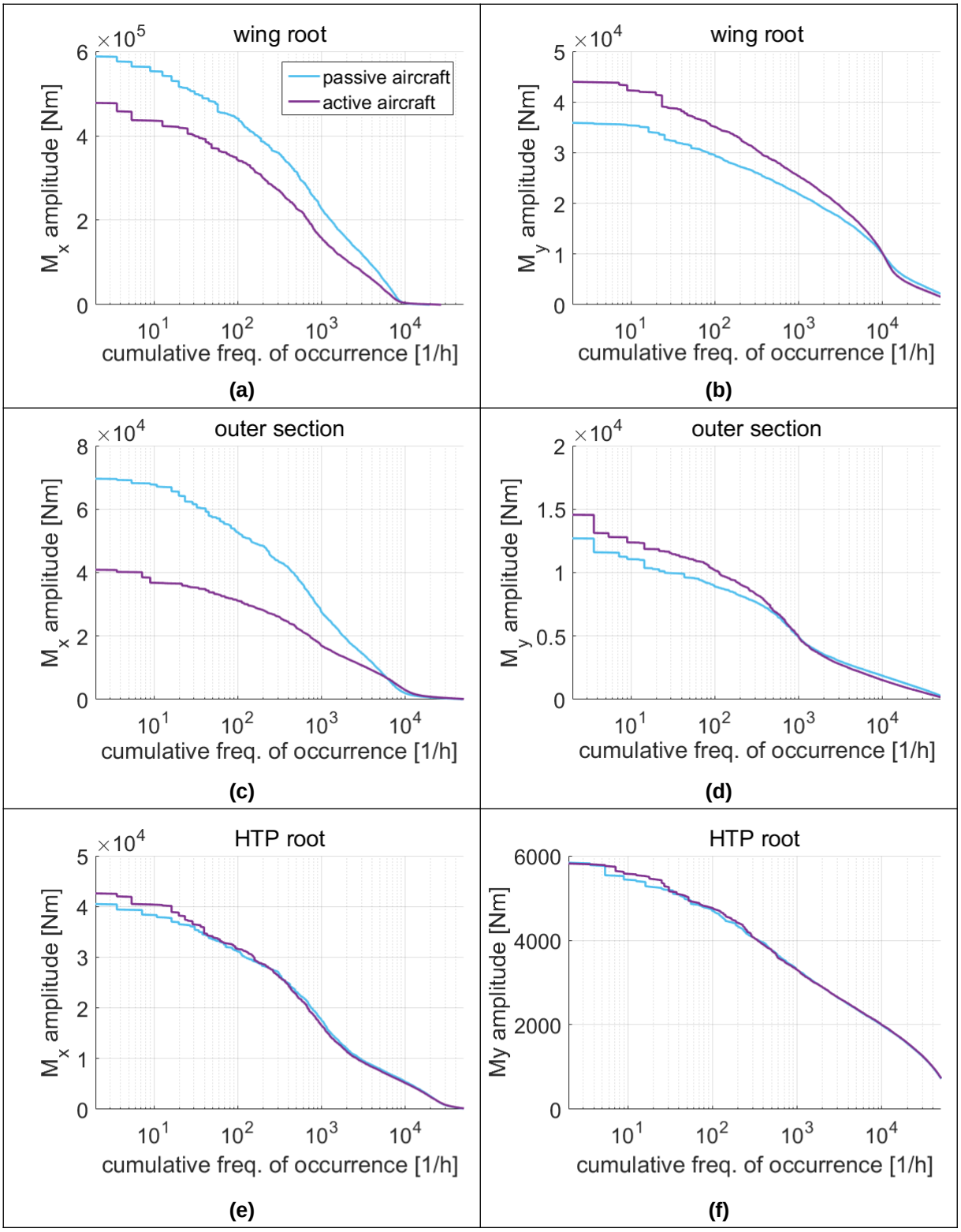

Figure 6.18. Cut load collectives during the climb phase of D150

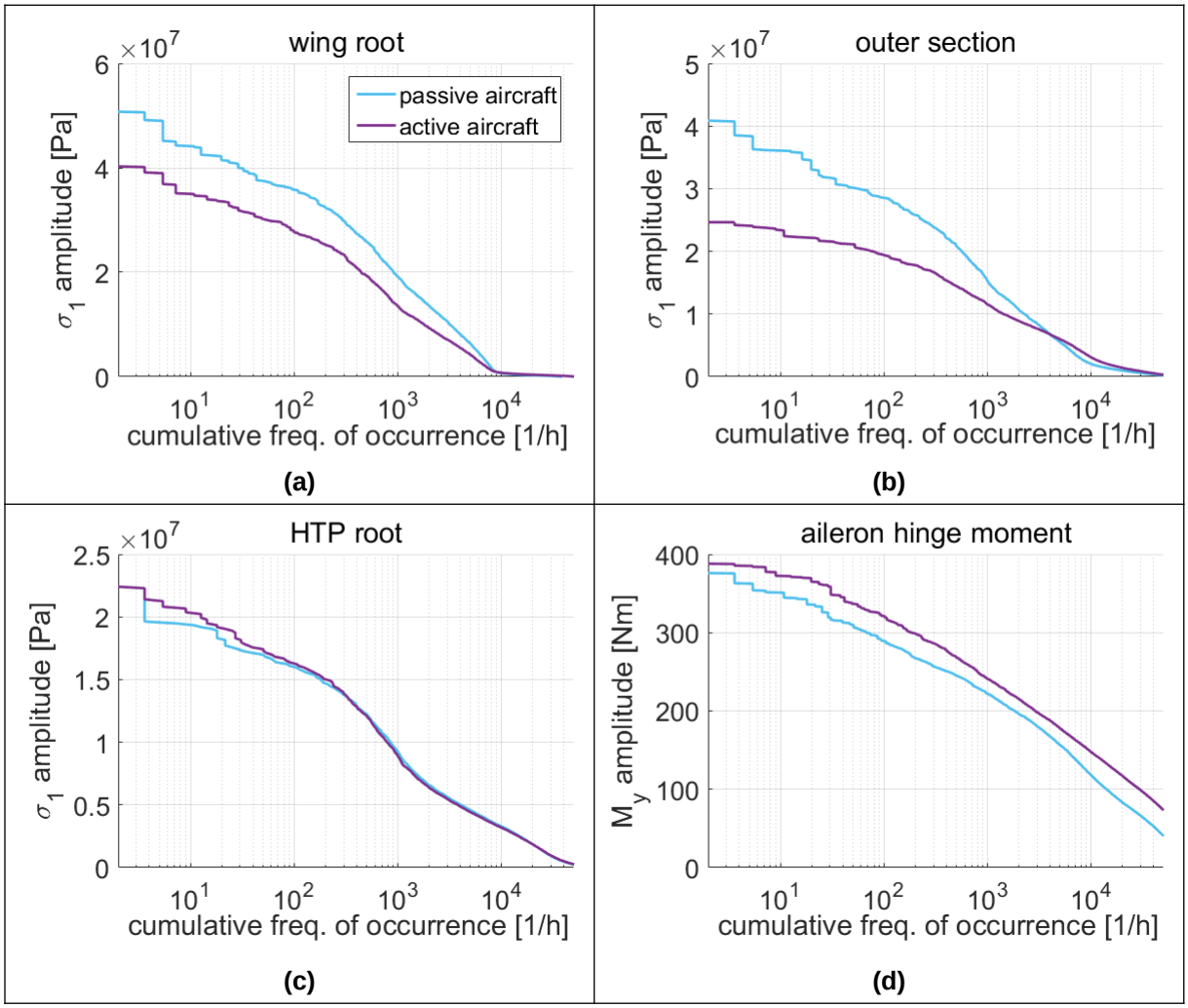

Figure 6.19. Stress and hinge moment collectives during the climb phase of D150

To investigate the differences in the fatigue behavior between the active and passive aircraft, selected shell elements on the wing box and HTP box are observed as well. In this case, the reference quantity is the major principal stress σ_1 of the selected elements. As apparent in Figure 6.19(a) and (b), the active aircraft has lower cumulative frequencies of occurrence in general, except at the outer section below 7 MPa. On the HTP (Figure 6.19(c)), the active aircraft generally has larger numbers of cumulative stress-cycles, and the maximum stress amplitude is at the same level as the passive aircraft.

In the aileron hinge moment $M_y(\mathrm{ail})$ (Figure 6.19(d)), the active aircraft generally has higher cumulative frequencies of occurrence, and its maximum amplitude is 3.6% larger than on the passive aircraft. Nevertheless, with a maximum hinge moment during the design maneuvers of 3152 Nm on the passive aircraft and 3355 Nm on the active aircraft as stated in Subsection 6.2.1, the maximum hinge moment amplitude of approx. 400 Nm during turbulence (Figure 6.19(d)) is seen as uncritical, at least for the fatigue aspect. As an example: if the maximum hinge moment represents the yield strength of the actuation system made of metals, then loading cycles with amplitudes of less than 20% of the maximum value would inflict practically negligible fatigue damage.

6.3.3 Fatigue damage accumulation

To quantify the structural fatigue damage according to Palmgren-Miner based on the generated stress collectives, reference S-N curves from a fatigue experiment campaign by Mayer et al. [60] are taken into account. Before the damage accumulation is calculated, the following assumptions are made:

- S-N curves with a stress ratio – ratio between the minimum and maximum stress in a load cycle – of 0.1 are taken as reference. This assumption is based on the following: during the 1g-flight, the static major principal stress at the observed element at the root is 88 MPa. According to Figure 6.19(a), the maximum amplitude of the major principal stress during turbulence is 50 MPa. This yields a stress ratio of (88 MPa-50 MPa)/(88 MPa+50 MPa)=0.28. Furthermore, the stress ratio for ground-air-ground cycles elaborated in Section 5.5 is assumed to be 0.0. For these reasons, S-N curves with a stress ratio of 0.1 are seen as an acceptable compromise.
- Since the stress amplitudes in the derived collectives are below 70 MPa, the respective S-N curve approximation function derived by Mayer et al. for amplitudes below 70 MPa is selected and extrapolated.
- A fatigue limit is not considered. This means, there is a finite number of cycles to failure for every stress amplitude.
- Since a scatter of cycle numbers, at which failure occurs, is observed in the fatigue experiments, a safety factor of 10 is assumed for the stress cycles to failure.
- Stress amplifications due to structural discontinuities are not taken into account since the FE-models are also optimized without considering those aspects.

With those assumptions, the approximation function for the S-N curve is:

$$N_f = C \cdot \left(\frac{\sigma_{1,a}}{1\,\mathrm{Pa}}\right)^{-n} \cdot \frac{1}{F_S}, \tag{6.13}$$

with:

N_f : cycles to failure [-],
C : S-N curve constant ($1.31 \cdot 10^{66}$) [-],
$\sigma_{1,a}$: major principal stress amplitude [MPa],
F_S : safety factor [-],
n : S-N curve exponent (30.69) [-].

Figure 6.20 shows the S-N curve used in the analysis, and Table 6.10 lists the accumulated fatigue damage values of the observed shell elements for one flight according to Table 6.8. For every observed shell element, the highest fatigue damage value is highlighted. A more detailed list of fatigue damage per hour of flight in the respective phases can be found in Table A-3 in the Appendix.

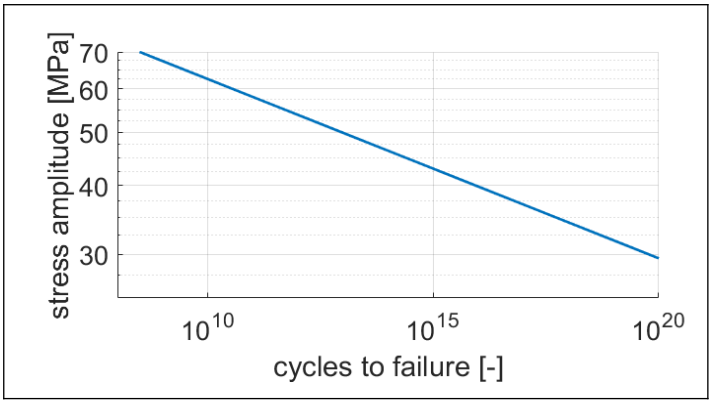

Figure 6.20. S-N curve for the turbulence analysis of D150

Table 6.10. Turbulence fatigue damage per flight on D150

Observed shell element	Damage per flight – passive aircraft	Damage per flight – active aircraft
Wing root	$2.15 \cdot 10^{-12}$	$9.97 \cdot 10^{-15}$
Outer wing section	$1.05 \cdot 10^{-15}$	$4.19 \cdot 10^{-21}$
HTP root	$2.67 \cdot 10^{-21}$	$4.58 \cdot 10^{-21}$

In addition to the turbulence loads, a simplified ground-air-ground cycle according to Section 5.5 is considered in the fatigue calculation. For the ground-air-ground cycle, the aircraft is assumed to have zero stress on the ground, and the stresses during flight are taken from a reference +1.3g maneuver calculation. During that maneuver, the MLA of the active aircraft is deflected by -2.5° (trailing edge up) according to Equation (5.7).

To calculate the fatigue damage, the stress amplitudes are half of the stresses during the +1.3g maneuver. Table 6.11 lists the resulting stresses on the observed elements and the respective fatigue damage per flight cycle.

Table 6.11. Fatigue damage per ground-air-ground cycle on D150

Observed shell element	Passive aircraft		Active aircraft	
	Major principal stress amplitude	Damage per cycle	Major principal stress amplitude	Damage per cycle
Wing root	56.9 MPa	$5.48 \cdot 10^{-12}$	57.0 MPa	$5.93 \cdot 10^{-12}$
Outer wing section	55.9 MPa	$3.25 \cdot 10^{-12}$	56.9 MPa	$5.70 \cdot 10^{-12}$
HTP root	16.8 MPa	$3.10 \cdot 10^{-28}$	17.9 MPa	$2.10 \cdot 10^{-27}$

To acquire the total fatigue damage in one flight, the values from Table 6.10 and Table 6.11 are added, and Table 6.12 shows the results.

Table 6.12. Total fatigue damage per flight on D150

Observed shell element	Damage per flight – passive aircraft	Damage per flight – active aircraft
Wing root	$7.62 \cdot 10^{-12}$	$5.94 \cdot 10^{-12}$
Outer wing section	$3.25 \cdot 10^{-12}$	$5.70 \cdot 10^{-12}$
HTP root	$2.67 \cdot 10^{-21}$	$4.58 \cdot 10^{-21}$

With the fatigue damage values in Table 6.12, and with the probability of exceedance of the turbulence intensity of approx. 0.1% mentioned in Section 5.2, it is concluded that:

- On both aircraft, the wing receives more fatigue damage from the ground-air-ground cycle compared to turbulence.
- In turbulence, there is a clear trend that the wing of the passive aircraft shows significantly more fatigue damage compared to the active aircraft. On the other hand, the HTP of the active aircraft exhibits slightly more damage. This is caused by the GLA creating a small amount of additional pitching moment due to the aileron deflections. Hence, the RMS of pitch acceleration of the active aircraft is up to 8.4% higher. This induces additional vertical movements and also loads on the HTP.
- One ground-air-ground cycle tends to cause more wing fatigue damage to the active aircraft than to the passive aircraft.
- In general, the wing root gets more fatigue damage compared to the outer wing section.
- Judging by the highest damage values of each aircraft (the largest numbers in every column in Table 6.12) with $7.62 \cdot 10^{-12}$ on the passive and $5.94 \cdot 10^{-12}$ on the active aircraft, the expected fatigue life of the active aircraft is 1.28 times longer than that of the passive aircraft.

If the fatigue damage values listed in Table 6.12 are extrapolated to e.g. 40000 flight cycles, those are still significantly below 1.0 – assuming that the turbulence intensity is equal to the values in Table 6.8 and there is no stress amplification due to structural discontinuities.

6.4 Further results

Uncertainties in the stress amplifications

If fatigue loads are to be included in the design process, the areas prone to fatigue damage have to be known and modeled – together with the respective stress amplification factors and the material reinforcements. The stress amplification factor is defined as the ratio between the maximum near-field stress and the far-field stress, see Figure 6.21.

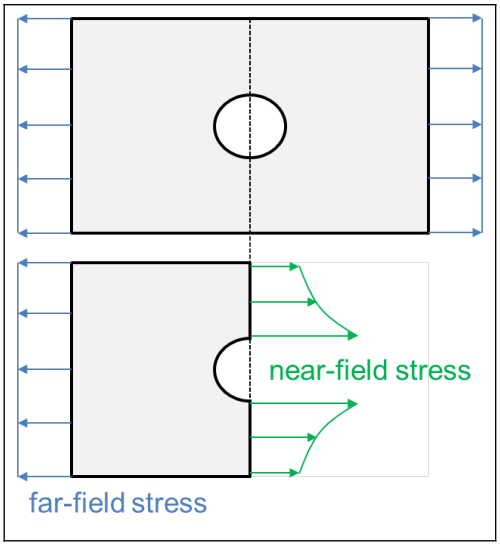

Figure 6.21. Illustration of stress amplification near a hole

In wing box structures that are optimized with strength and buckling stability constraints, the limit stress is unlikely to be reached since buckling can occur at considerably lower stresses. In that case, a stress amplification factor can exist to a certain degree without the structure having to be reinforced.

However, if such stress amplification exists, the fatigue life can be affected in a negative way. As an example: if the passive aircraft had an exemplary stress amplification factor of 2.0 at the root section, the fatigue damage would increase by a factor of $2.0^{30.69}$ based on Equation (6.13), namely from $7.62 \cdot 10^{-12}$ to $1.32 \cdot 10^{-02}$, assuming that the same S-N curve is still valid. This means, the active aircraft is expected to be able to retire way before the intended 40000 flight cycles. This huge degradation of the fatigue life is caused by the large exponent n in the formula for the S-N curve. With local material reinforcements, the increase in near-field stress can be reduced. As a conclusion, stress amplification factors and the local material reinforcements play a crucial role in the fatigue life prediction of aluminum aircraft.

Engine lateral accelerations on the D150 configuration

On aircraft configurations with engines attached under the wing such as the D150 configuration, the engine modes and the wing bending movement can affect each other. With additional excitation from the ailerons, the interaction between the engines and wing bending movements can be influenced in a negative way, as shown by the following phenomenon:

For an experiment of vortex decay investigation, the DLR research aircraft ATTAS should perform oscillatory, symmetric trailing edge surface and aileron deflections. A technical report by Schwochow [87] however states that the symmetrical deflection of ailerons on ATTAS (VFW-614) evokes large lateral accelerations on the engines. On that aircraft, the engines are attached above the wing and the lateral accelerations are mainly caused by the wing bending.

To investigate the relevance of the described phenomenon on the D150 configuration, the engine's lateral accelerations during turbulence are analyzed. For this aim, the reference flight conditions as well as the parameters listed in Section 6.3 are considered.

Table 6.13 shows the RMS values of the engine's lateral acceleration in the respective flight phases, for the active and passive aircraft each. It is apparent that the RMS values of the passive aircraft are larger, except during the descent phase. However, if averaged per flight, the passive aircraft has a slightly higher RMS value of the engine lateral acceleration. As a conclusion, the symmetric aileron deflection on the active D150 configuration does not increase the engine lateral loads.

Table 6.13. Engine lateral acceleration RMS on D150

Flight phase	Duration	Passive aircraft	Active aircraft
Climb	0.4 hours	1.59 m/s²	1.32 m/s² (-17.0%)
Cruise	2.0 hours	0.69 m/s²	0.55 m/s² (-20.2%)
Descent	0.5 hours	1.35 m/s²	1.41 m/s² (+4.4%)
Average per flight	2.9 hours	0.93 m/s²	0.80 m/s² (-14.0%)

7 Loads, optimization and fatigue results of ALLEGRA configuration

This chapter sums up the analysis parameters and results for the ALLEGRA configuration. The analysis of the ALLEGRA configuration is of great relevance from the aircraft design point of view: it has a forward swept wing and is made of composite materials. Not only its aeroelastic characteristics are expected to be different compared to conventional configurations, but also its fatigue behavior is different compared to aluminum.

The first section of this chapter defines the parameter space for the loads analysis and structural optimization. With the parameters, the process explained in Section 3.7 is run iteratively. The design loads, structural masses and aeroelastic parameters resulting from the final cycle are shown, and a discussion regarding the differences between the active and passive aircraft follows.

Subsequently, the turbulence loads and fatigue analysis along with the reference flight mission are described. For each reference flight phase, the turbulence loads are calculated and their collectives are acquired using the rainflow-counting algorithm. Collectives of the major principal strain on selected structural elements on the lower skin of the wing and HTP are derived. Furthermore, strains caused by a reference ground-air-ground cycle are calculated. With those results, strain collectives for the reference flight cycle are derived, and the fatigue damage values are calculated for the active and passive aircraft with the methodology elaborated in Chapter 5. At the end of this chapter, a discussion regarding the fatigue results follows.

7.1 Parameter space for loads analysis and structural optimization

This section gives an overview of the parameters for the loads analysis and structural optimization. These comprise the mass configurations, flight conditions, gust and maneuver cases considered in the simulations as well as the objective function, design variables and constraints in the structural optimization.

7.1.1 Mass configurations

For the ALLEGRA configuration, the same nine mass configurations are selected as for the D150 configuration (see Subsection 6.1.1). As a remark: the nominal mass values and the respective mass distributions are slightly different due to the different aircraft geometry and design masses. Figure 7.1 and Table 7.1 give an overview of the mass configurations. The mass labels are defined according to Pinho Chiozzotto [72].

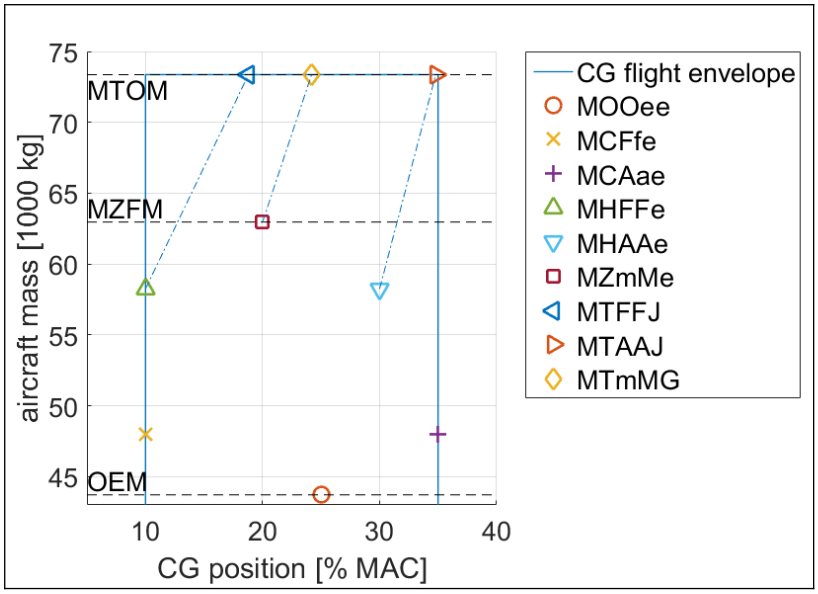

Figure 7.1. Mass and balance diagram of considered configurations – ALLEGRA

Table 7.1. Overview of the mass configurations – ALLEGRA

Label	Mass [kg]	CG [% MAC]	Notes
MOOee	43712	25.0	Operating empty mass
MCFfe	48000	10.0	Forward CG, light payload
MCAae	48000	35.0	Rear CG, light payload
MHFFe	58250	10.0	Forward CG, heavy payload
MHAAe	58250	30.0	Rear CG, heavy payload
MZmMe	62962	20.0	Middle CG, maximum zero fuel mass
MTFFJ	73365	18.8	MHFFe with 15.1 t fuel
MTAAJ	73365	34.8	MHAAe with 15.1 t fuel
MTmMG	73365	24.2	MZmMe with 10.4 t fuel

7.1.2 Flight conditions within the design envelope

Analogous to the D150 configuration, the three altitudes selected for the loads analysis range from sea level to 7000 m. At 7000 m, the design cruise speed V_C coincides with the design cruise Mach number M_C. At each altitude, the speeds V_A, V_C and V_D are considered based on the ALLEGRA report [85], see Table 7.2. The report [85] also documents the discontinuities of V_C and V_D at the altitude of 3000 m. The labels for the flight conditions are based on Pinho Chiozzotto [72]. Figure 7.2 visualizes the flight envelope.

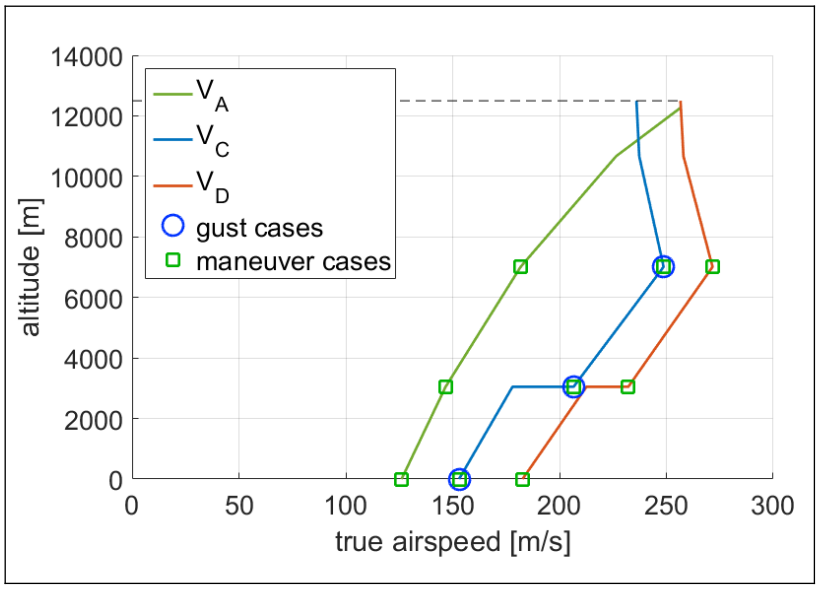

Figure 7.2. Flight conditions in the design envelope – ALLEGRA

Table 7.2. Overview of the flight conditions – ALLEGRA

Altitude [m]	V_A [m/s TAS]	Label	V_C [m/s TAS]	Label	V_D [m/s TAS]	Label
0	126.1	OA000	153.0	OC000	182.7	OD000
3000	146.7	OA100	206.6	OC100	212.5	OD100
7000	181.8	OA230	248.7	OC230	271.6	OD230

7.1.3 Gust and maneuver load conditions

The load conditions for the ALLEGRA configuration are based on those for the D150 configuration, except that the gust alleviation factor as described in Equation (6.4) and the design speeds at the respective flight conditions are different. The considered gust cases cover seven gust gradients as listed in Table 6.3. For the maneuvers, the edges of the maneuver envelope stated in Section 6.1.4 and illustrated in Figure 6.4 are taken into account.

7.1.4 Overview of the optimization task

With the mass configurations and flight conditions listed in Subsection 7.1.1 and 7.1.2, maneuver and gust loads are calculated as described in Subsections 6.1.3 and 6.1.4. The resulting loads are filtered according to Section 3.3 and are input into the structural optimization. The objective in the structural optimization is the minimization of the structural mass while considering the constraints explained in Subsection 7.1.5.

The design variable in the optimization is the material thickness. On a composite wing box, the lamination parameters can be varied in addition to the thickness. However, since aeroelastic tailoring is not in the scope this thesis, the ply angle distributions of the wing box are kept constant, see Section 2.1. Furthermore, the skin laminates are rotated by 30° as elaborated in Section 2.5.

On the ALLEGRA configuration, one design field – in which the design variable is constant – covers either the skin area between two ribs, spar area between two ribs or one rib. Each component – in this case the wing and HTP – is optimized separately. In the optimization run, only the starboard half of the wing box or HTP box is included, and the resulting properties are mirrored onto the corresponding port half. A wing box half has 28 ribs which results in 136 design fields for the wing whereas an HTP half has 12 ribs and a total of 56 design fields.

7.1.5 Constraints in the structural optimization

On composite structures, the strength analysis is based on strains, in contrast to stress-based strength analysis of aluminum structures. For the composite ALLEGRA configuration, the constraints considered in the structural optimization are von-Mises strain and buckling stability. According to [21], von-Mises strain is defined by:

$$\epsilon_m = \frac{2}{3}\left({\epsilon_{xx}}^2 + {\epsilon_{yy}}^2 - \epsilon_{xx}\epsilon_{yy} + 3{\epsilon_{xy}}^2\right)^{\frac{1}{2}}, \tag{7.1}$$

with:

ϵ_m : von-Mises strain [-],
ϵ_{xx} : tensile strain in x-direction [-],
ϵ_{yy} : tensile strain in y-direction [-],
ϵ_{xy} : shear strain [-].

A von-Mises strain allowable of $5.0 \cdot 10^{-3}$ is assumed based on IJsselmuiden (Appendix A in his thesis) [44] and with a safety factor of 1.5 according to CS25, strain limits of $3.3 \cdot 10^{-3}$ are considered in the structural optimization.

For the buckling constraints, the composite elements on the wing are assumed to be a homogeneous material with an anisotropic stiffness matrix according to Tetlow [91]. With this approach, the influence of the stacking sequence on the bending stiffness of the composite plate is neglected, and the compressive buckling stress is calculated with:

$$\sigma_{bcT} = \frac{\pi}{6\lambda}\left(\sqrt{E_{11}E_{22}} + \frac{1}{2}\nu_{12}E_{22} + \frac{1}{2}\nu_{21}E_{11} + 2\lambda G_{12}\right)\left(\frac{t}{b}\right)^2, \tag{7.2}$$

with:

$$\lambda = 1 - \nu_{12}\nu_{21}, \tag{7.3}$$

and:

σ_{bcT} : compression buckling stress according to Tetlow [Pa],
E_{11} : longitudinal tensile modulus [Pa],
E_{22} : lateral tensile modulus [Pa],
ν_{12}, ν_{21} : Poisson ratios [-],
G_{12} : shear modulus [Pa],
t : material thickness [m],
b : buckling field width [m].

The shear buckling constraints for the ribs and spars – which are used for the aluminum aircraft – are replaced with the compressive buckling constraints.

Furthermore, a minimum thickness of 2 mm is selected for every design field. For a realistic design, the material thicknesses should be equal to integer multiples of the single ply thickness of approx. 0.125 mm and a stacking sequence to reach the intended ply angle distributions should be feasible. In this thesis however, the restrictions concerning the discrete thickness values and the stacking sequence are not applied.

7.2 Comparison of design loads, structural masses and aeroelastic parameters

With the parameters from Section 7.1, the design process explained in Section 3.7 is run. The following subsections describe the resulting design loads, structural masses and aeroelastic parameters.

7.2.1 Design loads

After seven cycles of loads analysis and structural optimization, the resulting wing bending moment envelopes are shown in Figure 7.3 and Figure 7.4. On the passive aircraft, gusts evoke the largest positive bending moments M_x, whereas in the negative range both gusts and maneuvers are generally at the same level. On the active aircraft, maneuver loads are dominant in the wing bending moment envelope, it also has 10.7% less wing root bending moment. At the outer section (y=12 m), the decrease of wing bending moment on the active aircraft is 17.8%. At this point, a more aggressive setting for the MLA seems to be a plausible measure to match the maximum bending moments due to maneuvers and gusts. However, analogous to the D150 configuration, the aerodynamic feasibility of larger MLA deflections at high Mach numbers and the additional increase in the maximum torsion have to be checked first.

The 1D envelopes of Figure 7.3 and Figure 7.4 mainly show the global trend of the cut loads. The 2D envelopes give insight into the correlation between the load components at the observed positions. For this aim and for the turbulence analysis, reference monitoring stations at the wing root, wing outer section and HTP root along with the local coordinate systems are defined, see Figure 7.5.

Figure 7.6 visualizes 2D load envelopes of the wing. The envelopes of the active aircraft are visibly rotated counter-clockwise which indicates a reduction of maximum bending moment M_x along with a noticeable increase in torsion M_y. At the outer section, the increase in the maximum torsion is 26.2%. At the root, the maximum torsion increases by 5.9%, and the rotation of the envelope is less distinct since the relative effect of the load alleviation is smaller compared to the wing outer section.

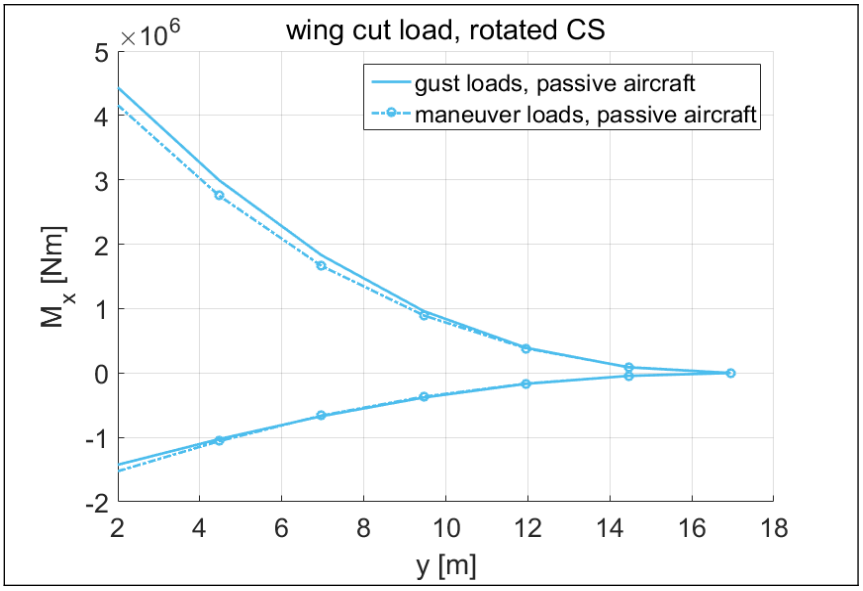

Figure 7.3. Wing bending moment of passive ALLEGRA

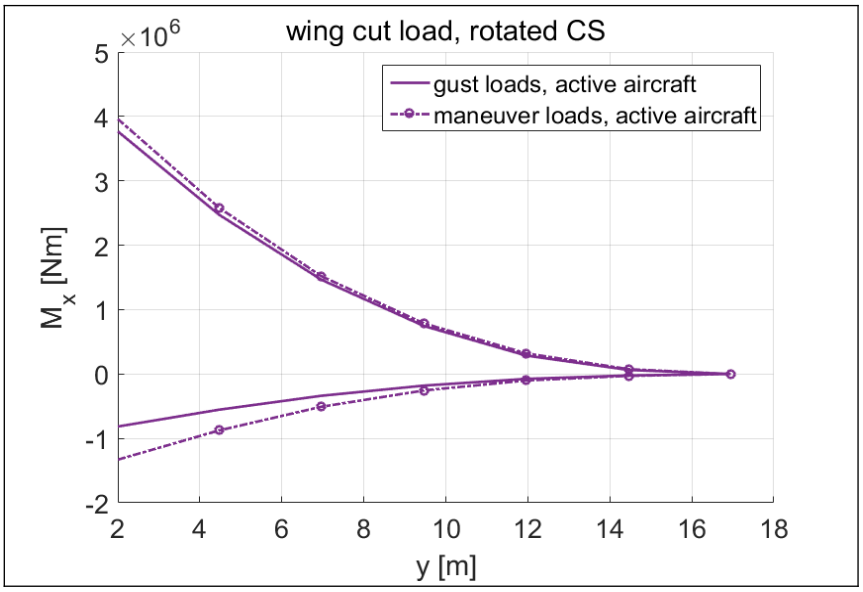

Figure 7.4. Wing bending moment of active ALLEGRA

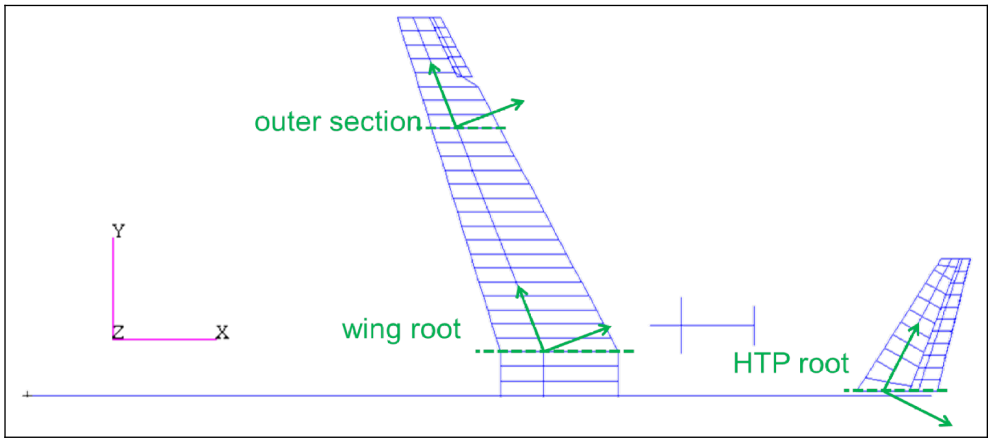

Figure 7.5. Selected cut load monitoring stations on ALLEGRA

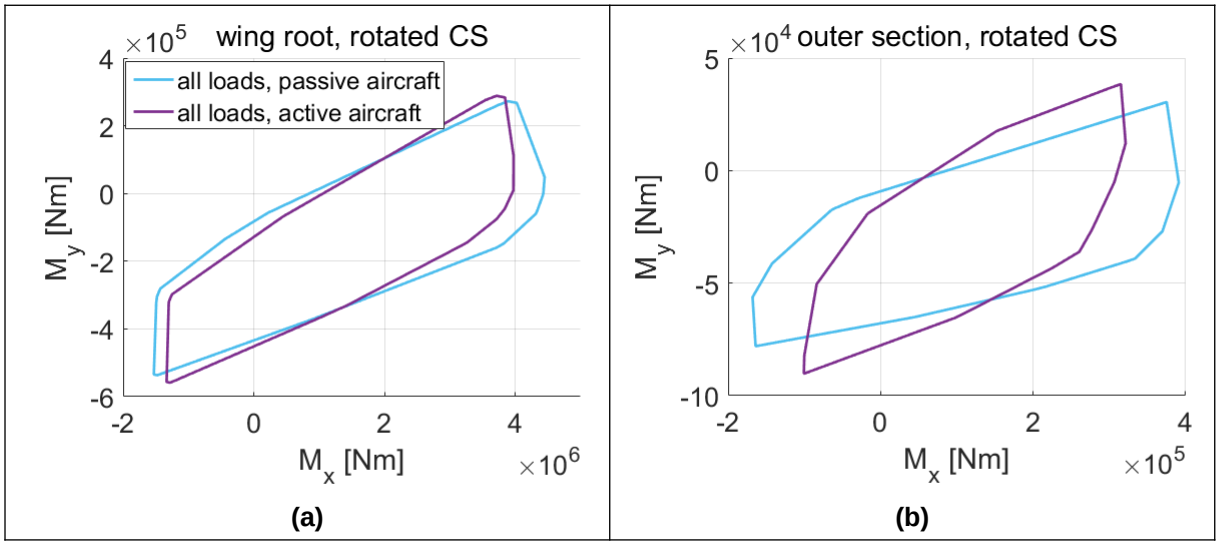

Figure 7.6. 2D load envelope comparison on ALLEGRA

On the passive aircraft, the maximum bending moment is reached during gusts with the mass configuration MTmMG (MTOM with mid CG, Table 7.1) that has the heaviest payload. This implies that a heavy fuselage induces large bending moments during gust encounters. The maximum torsion is reached during maneuvers with the mass configuration MTFFJ (MTOM with forward CG, Table 7.1). On the active aircraft, the maximum bending moment and torsion is reached during maneuvers, predominantly with the mass configuration MTFFJ. Compared to the D150 configuration, the maneuver loads form comparably round envelopes, see Figure A-1(b) in the Appendix whereas the maneuver load envelope of the D150 configuration is more slender as visible in Figure A-1(a). This indicates a larger torsion fluctuation of the ALLEGRA configuration during maneuvers which is explained by the following aspects:

- During high-speed pull-ups (at V_D), the angle of attack is moderate, and the center of pressure is relatively far backward since the camber has a large contribution to the lift. This backward center of pressure lies relatively near to the LRA. Hence, the torsion is relatively low.
- During low-speed pull-ups (at V_A), the angle of attack is relatively large, and the center of pressure shifts forward – toward the 25% chord line. This causes the wing to have a larger torsion and a more pronounced nose-up twist.
- The nose-up twist induces a larger local angle of attack that in turn amplifies the lift. Due to the bending-torsion-coupling of the forward swept wing, the amplified lift increases the nose-up twist and the torsion further. Hence, the torsion difference between a high-speed and low-speed pull-up is relatively large. The load case selection algorithm described in Section 3.3, the number of load cases for the structural optimization ranges between 46 and 55.

Concerning the aileron hinge moments, the passive aircraft shows a maximum magnitude of 4220 Nm during design maneuvers, while the active aircraft has to withstand a maximum of 3520 Nm during design gust encounters that is 16.6% lower. In this case, the aileron actuators of the active aircraft do not have to be reinforced with regards to maximum power or torque.

7.2.2 Structural masses

Figure 7.7 shows the convergence history of the ALLEGRA wing box mass. To gain a more detailed insight into the convergence, Figure 7.8 visualizes RMS values of the relative change in material thicknesses between each cycle according to Equation (6.12). After seven cycles of loads analysis and structural optimization, the wing box of the active aircraft is 6.1% or 283 kg lighter compared to the passive aircraft. Concerning the material thickness convergence, the RMS values of thickness change between the last two cycles are 3.58% for the passive and 2.91% for the active aircraft.

Compared to the D150 configuration, the convergence of the wing box mass is relatively fast. E.g. between cycle 5 and 7, the wing box mass fluctuation is always under 0.3%. The faster convergence is possible because of the characteristic bending-torsion-coupling of forward swept wings. As an example: If the wing becomes lighter and softer in one optimization run, the subsequent loads analysis would result in higher loads due to its bending-torsion-coupling and load amplification effect around the wingtip. Hence, the wing would tend to become heavier and stiffer in the next optimization run. This in turn reduces the loads in the next analysis. This interdependency increases the convergence gradient and brings the forward swept wing to a comparable level of mass convergence in fewer cycles compared to backward swept wings.

Compared to the loads and optimization process of Klimmek [54] however, the mass convergence of the ALLEGRA configuration is still slower. This is caused by the significantly higher number of load cases and their selection algorithm as explained in Subsection 6.2.2.

Judging by the bending moment envelopes, the ALLEGRA configuration tends to be sized rather by dynamic gust loads than by quasi-steady maneuver loads, see Figure 7.3, or at least they are on similar levels, as visible in Figure 7.4. The RMS values of thickness change between cycle 3 and 7 as apparent in Figure 7.8 are generally higher compared to the D150 configuration. These phenomena indicate that dominant dynamic gust loads – combined with the applied load case selection algorithm – correlate with a higher fluctuation in the material thicknesses between each loads analysis and structural optimization cycle. As an example: in a particular cycle, a certain set of snapshots from the dynamic simulations is used for the optimization, and the structure is optimized with those dominant dynamic loads. Following that, the loads analysis of the next cycle is run. In the post-processing, the resulting set of snapshots (see Figure 3.2) and the corresponding spanwise load distributions for the optimization might differ from the previous cycle. These differences are expected to be larger compared to those resulting from quasi-steady maneuver simulations. In the worst case, the optimizer might find a significantly different optimum that would lead to a large RMS of the change in the material thicknesses.

The wing box masses shown in Figure 7.7 refer only to ideal load-carrying masses. With an empirical mass factor of 1.45 as mentioned in Subection 6.2.2, the wing mass difference between the active and passive aircraft would be 1.45·283 kg = 410.35 kg, assuming that the secondary masses comprising systems remain unchanged.

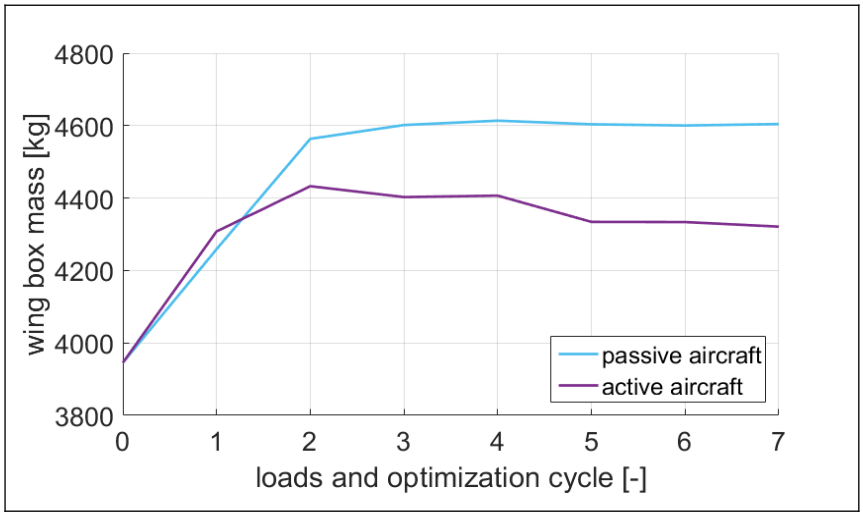

Figure 7.7. Wing box mass trend in the loads and optimization process of ALLEGRA

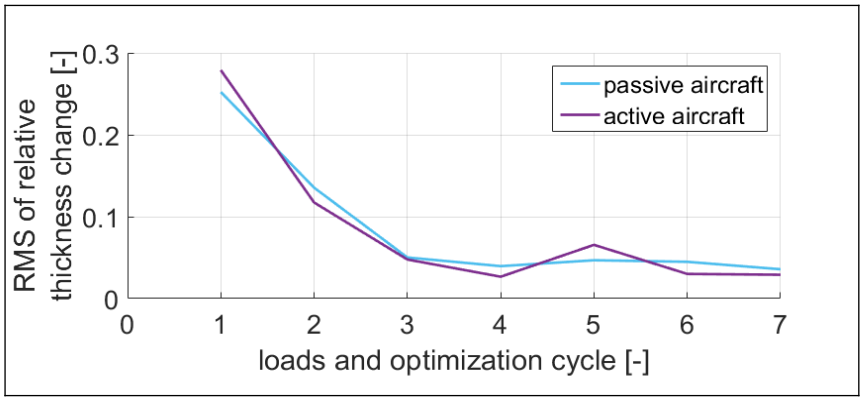

Figure 7.8. RMS of material thickness change of ALLEGRA wing box

Figure 7.9 visualizes the wing box mass difference of 6.1%. On the upper and lower skin of the passive aircraft, the areas with 18 mm thickness around the root are larger compared to the active aircraft. In the outer part, the skin areas with the minimum thickness are smaller on the passive aircraft. This indicates that the outer wing section of the passive aircraft is more heavily loaded due to the absence of load alleviation. On the other hand, the spars and ribs have similar thicknesses, except at the root where the rib of the passive aircraft is thicker. On the HTP, there is almost no difference between the active and passive aircraft, and the mass difference between both HTP boxes is below 1 kg, see Figure 7.10.

Regarding the structural dynamics, Table A-2 in the Appendix shows an overview of selected modes. The wing mode frequencies of the active aircraft are up to 5% lower than those of the passive aircraft. Those differences are larger compared to D150 (<2% between the active and passive aircraft). Hence, it can be concluded that an implementation of load alleviation on ALLEGRA has a larger impact on the wing stiffness reduction compared to D150.

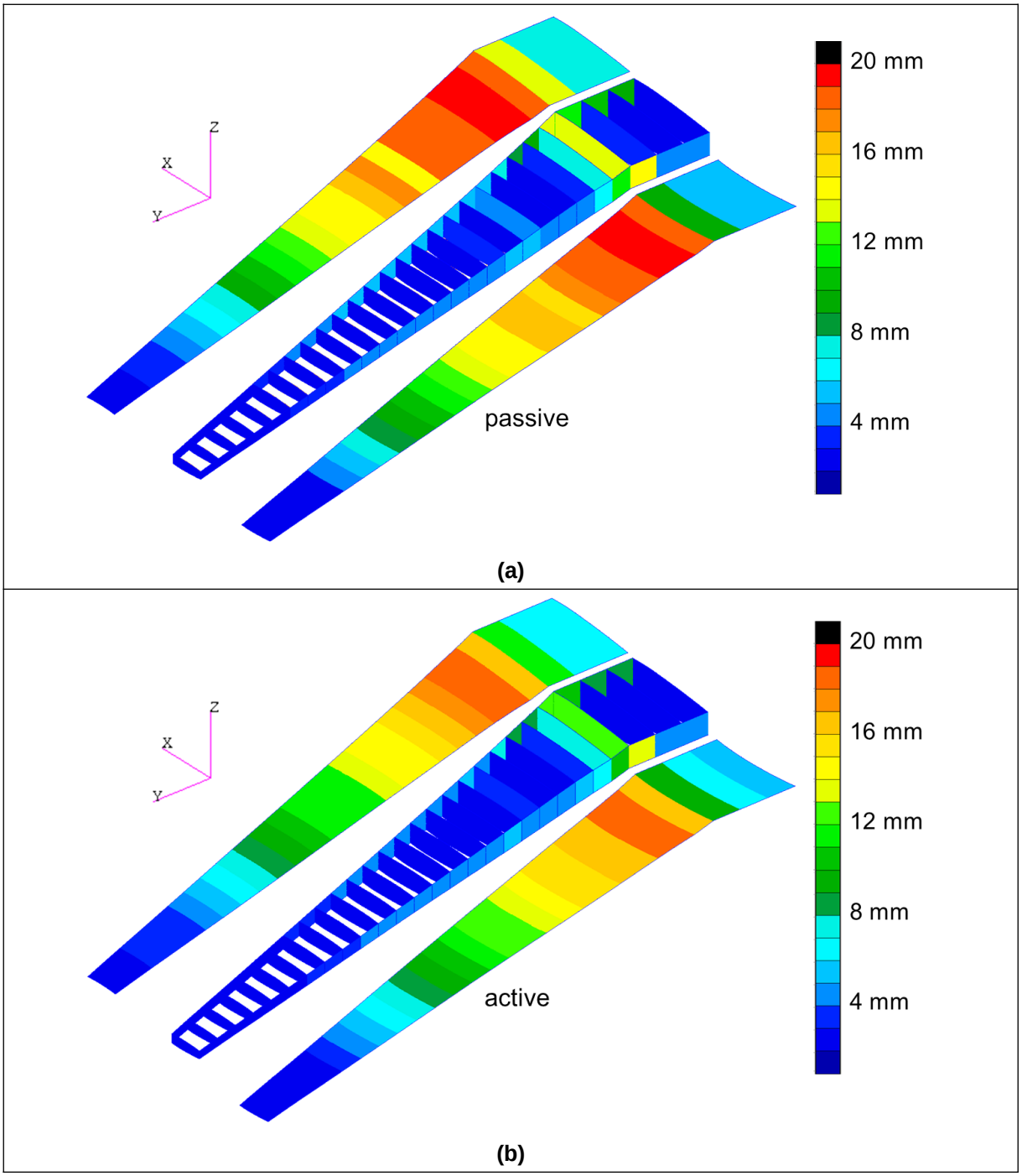

Figure 7.9. Wing material thickness distribution of ALLEGRA

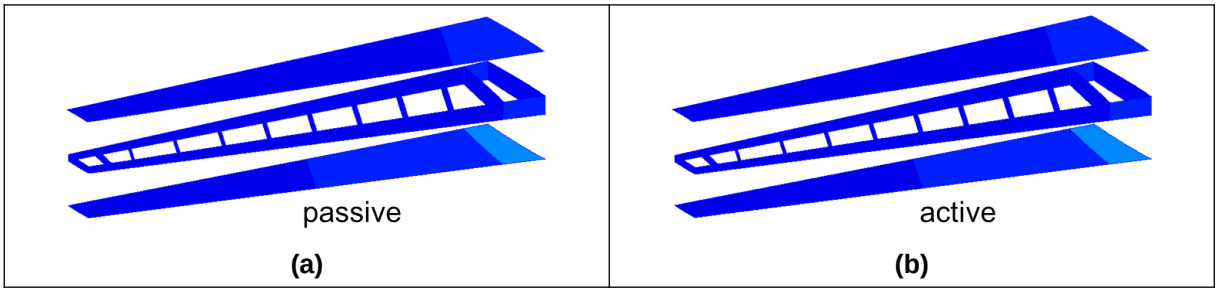

Figure 7.10. HTP material thickness distribution of ALLEGRA

7.2.3 Aeroelastic parameters

According to CS25.629, calculations concerning aeroelastic stability are to be conducted in the whole flight envelope and speeds up to V_D+15% have to be covered. Figure 7.11 shows the design envelope for aeroelastic stability of the ALLEGRA configuration. In this case, the torsional divergence and the flutter speed are considered.

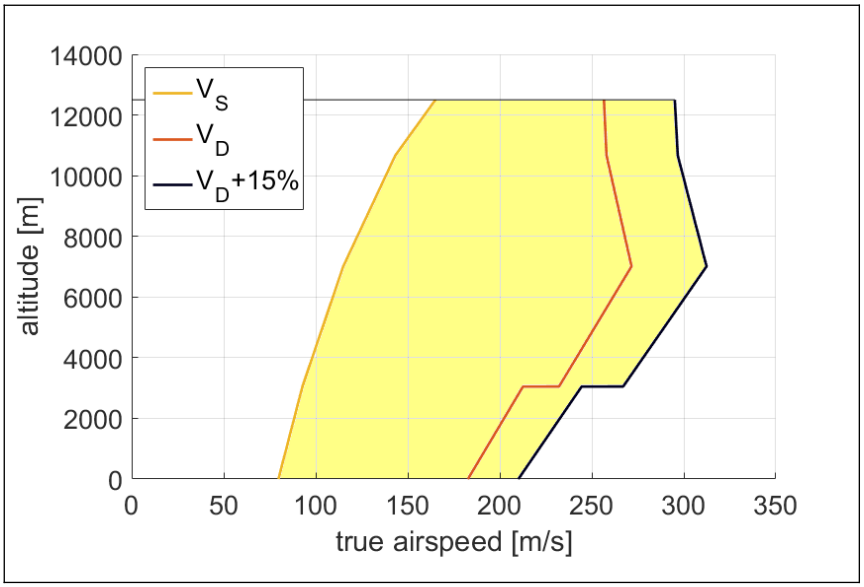

Figure 7.11. Design envelope for aeroelastic stability of ALLEGRA

Torsional divergence

For the divergence calculation, the reference altitude is set to sea level to enable having high dynamic pressures at relatively low Mach numbers, since the expected divergence dynamic pressure corresponds to a Mach number that is significantly higher than the design dive Mach number M_D. Since the DLM is only valid for Mach numbers smaller than 1.0, the reference Mach number is set to 0.95. With the DLM, local supersonic areas on the wing cannot be modeled, nevertheless, the Mach number of 0.95 is selected to take the magnification of the lift slope due to the air compressibility into account.

Table 7.3. Parameters of divergence calculation on ALLEGRA

Parameter	Value
Reference Mach number	0.95
Air density	1.225 kg/m³

To meet the requirements defined in CS25.629, the dynamic pressure, at which the divergence sets on, has to be larger than the dynamic pressure at V_D+15% that is 32254 Pa for the ALLEGRA configuration. Table 7.4 lists the results of the divergence calculations.

Table 7.4. Divergence dynamic pressures of ALLEGRA

Aircraft model	Divergence dynamic pressure
Passive aircraft	102038 Pa
Active aircraft	91743 Pa

With both values being approx. three times larger than 32254 Pa, no torsional divergence occurs at any speed up to V_D+15%. However, the active aircraft has a 10.1% lower divergence dynamic pressure since the wing material thickness is generally lower than for the passive aircraft, hence the wing stiffness is also lower, as mentioned in Subsection 7.2.2.

Flutter speed

For dynamic aeroelastic stability, the parameter to compare between the active and passive aircraft is the flutter speed. For this aim, a subsonic flutter calculation using MSC.Nastran is run. Table 7.5 lists the parameters for the reference flight condition of the flutter calculation. The reference Mach number is set to the equivalent of V_D (203 m/s CAS) at sea level to ensure a subsonic reference flow condition – with the assumption that a transonic flow condition emerges at Mach 0.7. The mass density of the air is set accordingly to the condition at sea level. The flutter calculation considers 50 Eigenmodes. This number of modes is assumed as sufficient since the potential dominant modes such as VTP torsion and bending as well as HTP torsion and bending are included. As mentioned in Section 2.3, a maximum reduced frequency of 3.0 is selected.

Table 7.5. Parameters of flutter calculation on ALLEGRA

Parameter	Value
Reference Mach number	0.5970
Air density	1.225 kg/m³
Number of Eigenmodes	50
Considered reduced frequencies	0.01 to 3.0 with 300 sampling points

Figure 7.12 shows the damping curves of the dominant mode involved at the flutter point and Figure 7.13 visualizes its mode shape that is the first VTP bending mode. This mode shape is identified through manual mode tracking of the frequency curve toward the low speeds where changes in the sequence of the modes are not anymore expected. Complete diagrams with all damping and frequency curves are shown in Figure A-4 in the Appendix. As mentioned in Section 3.6, with the applied KE-method, no complex modes corresponding to the flutter curves can be obtained.

Analogous to Subsection 6.2.3, a threshold line at -3% structural damping is drawn in Figure 7.12. It is apparent that the flutter speed is higher than V_D+15% and therefore there is no risk of flutter according to the subsonic calculations. The flutter speeds of the active and passive aircraft as well as the frequencies (2.87 Hz) at the flutter points are almost identical.

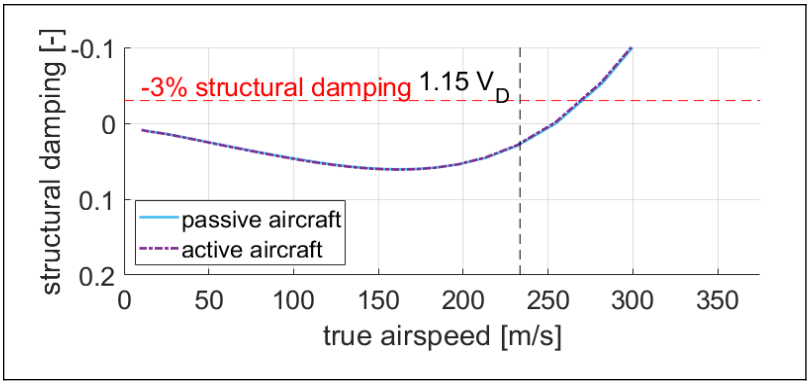

Figure 7.12. Curves of the flutter point of ALLEGRA

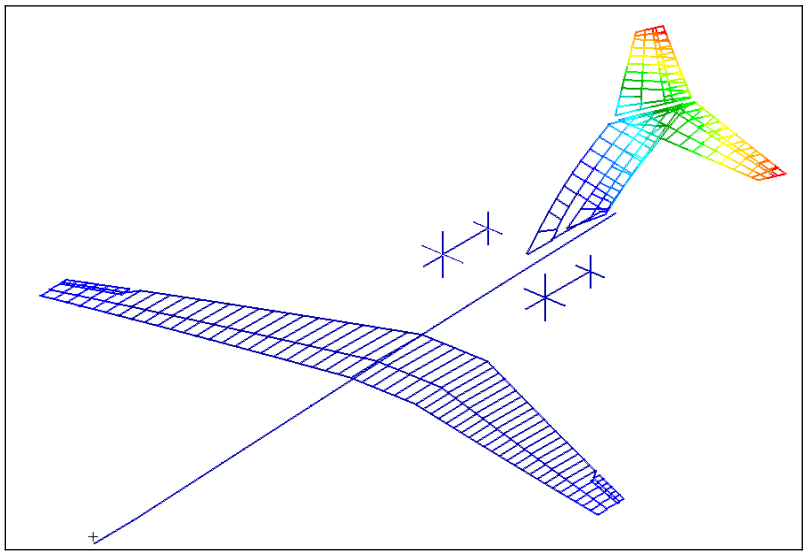

Figure 7.13. Dominant Eigenmode involved at the flutter speed of ALLEGRA

7.3 Turbulence loads and fatigue analysis

This section explains the parameters of the reference flight used in the turbulence loads and fatigue calculations. From those calculations, cut load and and strain collectives caused by atmospheric turbulence are extracted. To obtain a more global overview of the cyclic aircraft loads, strains resulting from a ground-air-ground cycle are considered as well. Using derived reference S-N curves, the total fatigue damage values for one flight cycle are accumulated. The differences between the active and passive aircraft are then discussed.

7.3.1 Reference parameters

Table 7.6 lists the reference flight route for the ALLEGRA configuration according to the considerations in Section 5.1.

Table 7.6. Reference flight route for ALLEGRA

Parameter	Value
Origin	Berlin Tegel (EDDT)
Destination	Athens International (LGAV)
Great circle distance	1823 km
Zero fuel mass	62962 kg
Take-off fuel	9598 kg
Trip fuel	6910 kg
Take-off mass	72560 kg
Landing mass	65650 kg

Analogous to the D150 configuration, the payload from the mass configuration MzmMe in Table 7.1 is taken. The payload brings the empty aircraft to MZFM. Table 7.7 shows the reference flight conditions with the same altitudes, airspeeds and turbulence RMS as for the D150 configuration, see Subsection 6.3.1. Figure 7.14 illustrates the reference flight mission, along with markers for the reference flight conditions for each phase. Table 7.8 lists the parameters for the ground-air-ground cycle according to Section 5.5.

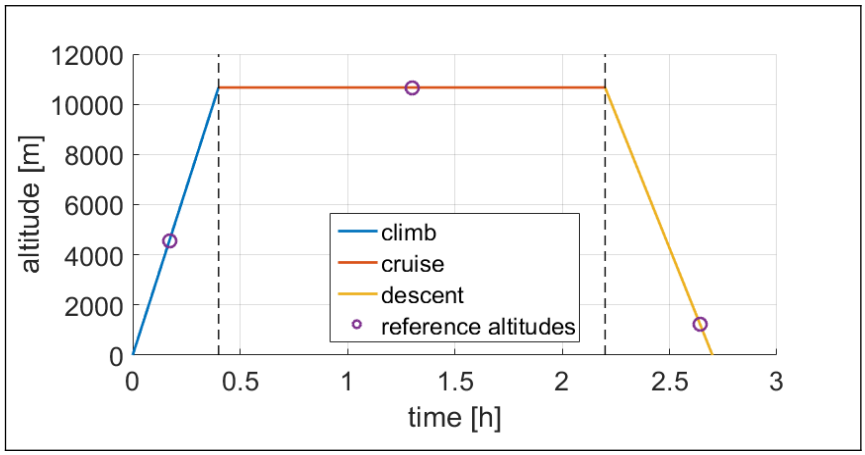

Figure 7.14. Visualization of the reference flight mission of ALLEGRA

Table 7.7. Reference parameters for each flight phase – ALLEGRA

Flight phase	Reference parameter	Value
Climb	Altitude	4572 m (FL150)
	Airspeed	181.6 m/s TAS (280 kts EAS)
	Fuel mass	9010 kg
	Turbulence RMS	2.743 m/s TAS
	Duration per flight	0.4 hours
Cruise	Altitude	10668 m (FL350)
	Airspeed	231.3 m/s TAS (Mach 0.78)
	Fuel mass	5892 kg
	Turbulence RMS	1.372 m/s TAS
	Duration per flight	1.8 hours
Descent	Altitude	1219 m (FL 040)
	Airspeed	136.5 m/s TAS (250 kts EAS)
	Fuel mass	2810 kg
	Turbulence RMS	3.048 m/s TAS
	Duration per flight	0.5 hours

Table 7.8. Reference parameters for the ground-air-ground cycle – ALLEGRA

Reference parameter	Value
Altitude	4572 m (FL150)
Airspeed	181.6 m/s TAS (280 kts EAS)
Fuel mass	9598 kg
Load factor	1.3
MLA deflection (active aircraft)	-2.5°

7.3.2 Cut load and strain collectives

Figure 7.5 visualizes the monitoring stations used in the turbulence analysis. Figure 7.15 shows the selected structural shell elements for the fatigue analysis. An observation of the wing root, outer section and HTP is relevant for understanding the fatigue behavior at different positions of the structure.

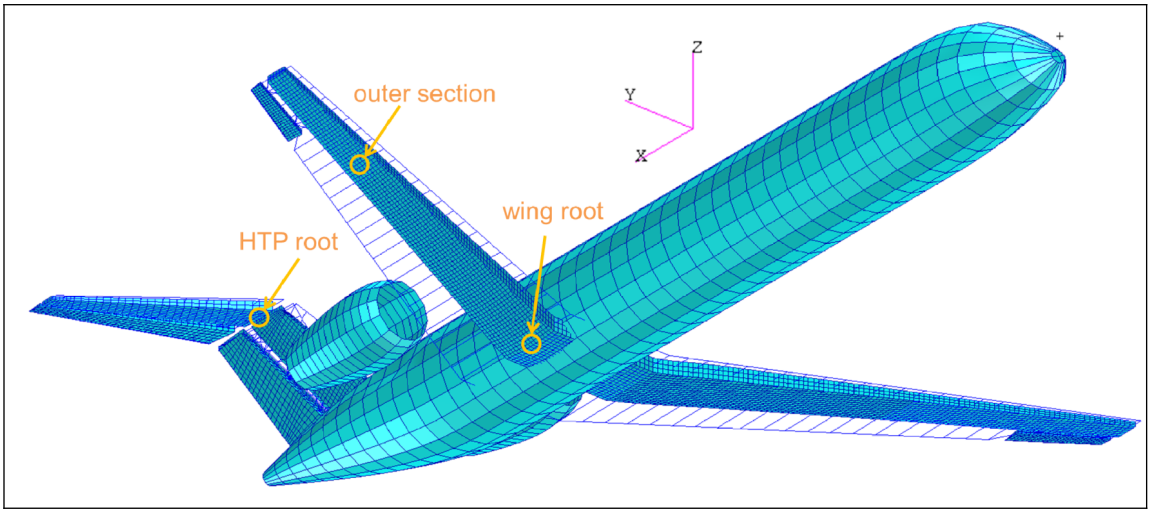

Figure 7.15. Selected structure elements for strain response of ALLEGRA

Analogous to the D150 configuration, the climb condition is investigated since it evokes higher levels of loads compared to the cruise phase due to the turbulence RMS value and high equivalent airspeed, see Table 7.7. The wing cut load collectives are shown in Figure 7.16(a) to (d). At the wing root, it is apparent that the bending moment M_x on the active aircraft is lower while the torsion M_y are at the same level. At the outer wing section, the differences in the amplitudes of bending moment and the torsion of both aircraft are more pronounced. There, the maximum amplitude of bending moment on the active aircraft is 36% smaller compared to the passive aircraft. The more pronounced differences occur due the fact that the aileron covers a larger percentage of area monitored at the outer section compared to that monitored at the root, analogous to the D150 configuration. On the HTP, there are no significant differences in the turbulence loads between the active and passive aircraft, see Figure 7.16(e) and (f).

To investigate the differences of fatigue behavior between the active and passive aircraft, selected shell elements on the wing box and HTP box are observed as well. In this case, the reference quantity to assess the fatigue behavior is the major principal strain ϵ_1 of the selected elements. As shown by the strain collectives in Figure 7.17(a) and (b), the active aircraft has lower cumulative frequencies of occurrence in general. On the HTP (Figure 7.17(c)), both aircraft practically have the same trend of load collectives. For the aileron hinge moment $M_y(\mathrm{ail})$ (Figure 7.17(d)), the active aircraft generally has higher cumulative frequencies of occurrence, and its maximum amplitude is 30.2% larger than that of the passive aircraft. Analogous to the D150 configuration, these hinge moment amplitudes up to 400 Nm are – at least from the fatigue point of view – uncritical since they are significantly smaller compared to those found in the design load calculations (4220 Nm on the passive aircraft and 3520 Nm on the active aircraft, see Subsection 7.2.1).

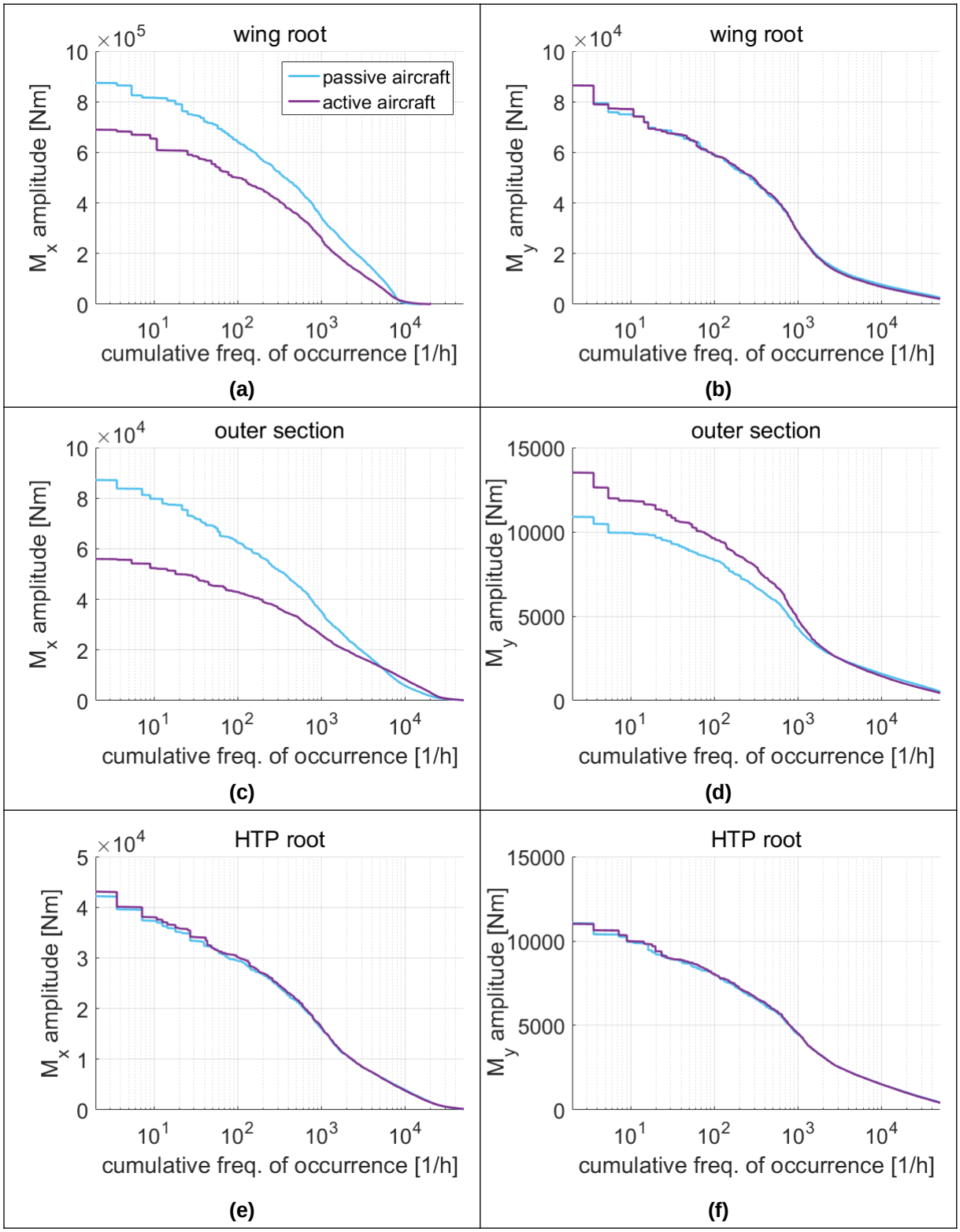

Figure 7.16. Cut load collectives during the climb phase of ALLEGRA

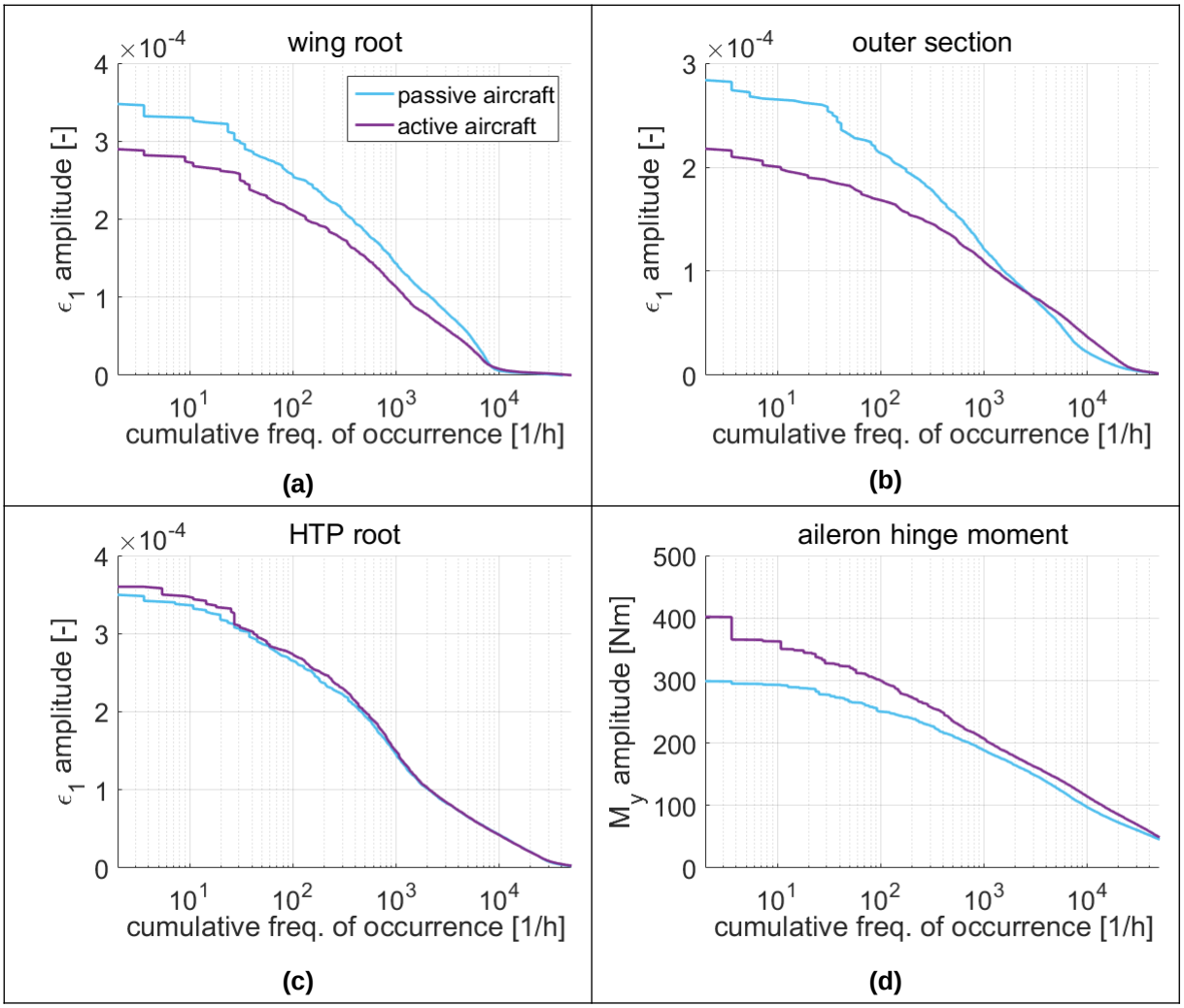

Figure 7.17. Strain and hinge moment collectives during the climb phase of ALLEGRA

7.3.3 Fatigue damage accumulation

To quantify the structural fatigue damage based on the generated strain collectives, reference S-N curves of IM7 composite approximated by Tan et al. [90] are applied. The approximation function considered is:

$$\frac{\sigma_{max}}{\sigma_{ult}} = 1.037 \cdot {N_f}^{-0.03269}, \tag{7.4}$$

with:

$\frac{\sigma_{max}}{\sigma_{ult}}$: ratio between maximum stress and ultimate tensile strength [-],

N_f : number of cycles to failure [-].

Before the damage accumulation is calculated, the following assumptions are made:

- The ratio between actual stress and ultimate stress is replaced by the ratio between actual strain and allowable strain.
- The allowable strain is set to $5 \cdot 10^{-3}$.
- There is no fatigue limit; the S-N curve is monotonously decreasing.

- S-N curves with a stress ratio – the ratio between the minimum and maximum stress in a load cycle – of 0.1 are taken as reference. This assumption is supported by the following points: the strain ratio during a ground-air-ground cycle is 0.0, analogous to the stress ratio of the D150 configuration. During the 1g-flight, the major principal strain of the observed element at the root is $6.2 \cdot 10^{-4}$. With a maximum amplitude of the major principal strain of $3.5 \cdot 10^{-4}$ during turbulence – as shown in Figure 7.17(a) – the resulting strain ratio is 0.28. Therefore, a strain ratio of 0.1 is seen as an acceptable compromise.
- Since a scatter of cycle numbers, at which failures occur, is observed in the fatigue experiments, a safety factor of 10 is assumed for the strain cycles to failure.
- Strain amplifications due to structural discontinuities are not taken into account, since the FE-models are also optimized without considering those aspects.

With those assumptions and after converting Equation (7.4) to a function of strain amplitude, the approximation for the S-N curve is:

$$N_f = \left(\frac{\epsilon_{rel}}{C}\right)^n \cdot \frac{1}{F_S}, \tag{7.5}$$

with:

$$\epsilon_{rel} = \frac{\epsilon_{1,max}}{\epsilon_{ult}} = \frac{2\epsilon_{1,a}}{\epsilon_{ult}\,(1 - r_s)}, \tag{7.6}$$

and:

N_f : cycles to failure [-],
ϵ_{rel} : relative strain [-],
C : coefficient (1.037) [-],
n : exponent (-30.59 = 1/-0.03269) [-],
F_S : safety factor [-],
$\epsilon_{1,max}$: maximum major principal strain [-],
ϵ_{ult} : ultimate strain ($5 \cdot 10^{-3}$) [-],
$\epsilon_{1,a}$: major principal strain amplitude [-],
r_s : strain ratio [-].

Figure 7.18 shows the S-N curve used in the analysis. According to Rosenfeld et al. [83], the Palmgren-Miner's rule is indeed not conservative for compressive stresses in composites. In that case however, the Palmgren-Miner's rule is applied with regards to the static failure stresses of the composite materials. On the ALLEGRA configuration however, the rule is applied with regards to the allowable strain. Since the failure stress is not reached yet at the allowable strain, the Palmgren-Miner's rule is assumed to be acceptable. Furthermore, since structural elements on the lower skin are observed, tensile strains are expected to be more dominant.

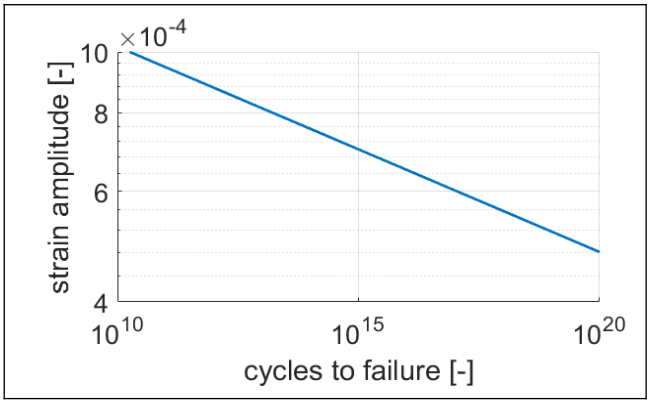

Figure 7.18. S-N curve for the turbulence analysis of ALLEGRA

Table 7.9 lists the accumulated fatigue damage values of the observed shell elements for one flight cycle according to Table 7.2. For every observed shell element, the aircraft with the higher fatigue damage is highlighted. A more detailed list of fatigue damage per hour of flight in the respective phase can be found in Table A-4 in Appendix.

Table 7.9. Turbulence fatigue damage per flight on ALLEGRA

Observed shell element	Damage per flight – passive aircraft	Damage per flight – active aircraft
Wing root	$2.74 \cdot 10^{-23}$	$4.49 \cdot 10^{-26}$
Outer wing section	$2.83 \cdot 10^{-26}$	$9.36 \cdot 10^{-30}$
HTP root	$6.24 \cdot 10^{-34}$	$2.26 \cdot 10^{-33}$

In addition to the turbulence loads, a simplified ground-air-ground cycle as derived in Section 5.5 is included in the fatigue calculation. In this case, the aircraft is assumed to have zero strain on the ground whereas the strains while airborne are obtained from a reference +1.3g maneuver simulation. According to Equation (5.7), the MLA of the active aircraft is deflected by 2.5° trailing edge up during that maneuver.

To derive the fatigue damage, the strain amplitudes are half of the strains during the +1.3g maneuver. Table 7.10 lists the strains on the observed elements and the corresponding fatigue damage for one flight cycle.

Table 7.10. Fatigue damage per ground-air-ground cycle on ALLEGRA

Observed shell element	Passive aircraft		Active aircraft	
	Major principal strain amplitude	Damage per cycle	Major principal strain amplitude	Damage per cycle
Wing root	$3.76 \cdot 10^{-4}$	$5.77 \cdot 10^{-24}$	$3.97 \cdot 10^{-4}$	$2.97 \cdot 10^{-23}$
Outer wing section	$3.23 \cdot 10^{-4}$	$5.18 \cdot 10^{-25}$	$3.58 \cdot 10^{-4}$	$1.24 \cdot 10^{-24}$
HTP root	$1.29 \cdot 10^{-4}$	$3.40 \cdot 10^{-38}$	$1.30 \cdot 10^{-4}$	$4.31 \cdot 10^{-38}$

To acquire the total fatigue damage in one flight, the values from Table 7.9 and Table 7.10 are added, and Table 7.11 lists the results.

Table 7.11. Total fatigue damage per flight on ALLEGRA

Observed shell element	Damage per flight – passive aircraft	Damage per flight – active aircraft
Wing root	$3.32 \cdot 10^{-23}$	$2.97 \cdot 10^{-23}$
Outer wing section	$8.01 \cdot 10^{-25}$	$1.24 \cdot 10^{-24}$
HTP root	$6.24 \cdot 10^{-34}$	$2.26 \cdot 10^{-33}$

With the fatigue damage values in Table 7.11, and with the probability of exceedance of the turbulence intensity of 0.1%, it is concluded that:

- In turbulence, there is a clear tendency that the wing of the active aircraft shows significantly less fatigue damage compared to the passive aircraft. However, the HTP of the active aircraft receives slightly more damage. This is caused by the GLA evoking a small amount of pitching moments due to the aileron deflections. This results in the pitch acceleration of the active aircraft being up to 2.2% higher. This in turn causes additional vertical movements and also loads at the HTP.
- One ground-air-ground cycle causes higher fatigue damage values on the wing of the active aircraft compared to the passive aircraft.
- In general, the wing root receives more fatigue damage compared to the outer wing section.
- Judging by the highest damage values of each aircraft (the largest numbers in every column in Table 7.11) which are $3.32 \cdot 10^{-23}$ on the passive and $2.97 \cdot 10^{-23}$ on the active aircraft, the expected fatigue life of the active aircraft is 1.12 times longer than the passive counterpart.

If the fatigue damage values in Table 7.11 are accumulated for e.g. 40000 flight cycles, those are still significantly below 1.0 – assuming that the turbulence RMS is equal to the values in Table 7.2 and there is no strain amplification due to structure discontinuities.

7.4 Further results

Uncertainties in the strain amplification and composite fatigue

If fatigue loads are to be considered in the design process, the potentially relevant areas have to be identified and modeled – together with the respective strain amplification factors. The definition of strain amplification is analogous to stress amplification illustrated in Figure 6.21. Since the wing box of the ALLEGRA configuration is also optimized with buckling stability constraints, a strain amplification factor can exist to a certain degree without exceeding the strain allowable. However, if the passive aircraft had an exemplary strain amplification factor of 2.0 at the root, the fatigue damage would increase by a factor of $2.0^{30.59}$ based on Equation

(7.5), namely from from $3.32 \cdot 10^{-23}$ to $5.35 \cdot 10^{-14}$, assuming that the same S-N curve still applies. This means, the passive aircraft could still complete 40000 flight cycles, however the fatigue damage increases by an order of magnitude of 9.2. This huge decrease in the fatigue life is induced by the large exponent n in the equation for the S-N curve. Furthermore, on composite wings, local material reinforcements are not as easily applicable as on aluminum wings, so that strain amplifications cannot be suppressed easily. As a conclusion, strain amplification factors play a huge role in the fatigue life prediction of composite aircraft.

For a more detailed composite fatigue analysis, an investigation using the fatigue model by Kassapoglou [51] and the Tsai Wu first ply failure criterion [14] can be considered, as shown by Rajpal et al. [76].

8 Investigations of load alleviation variations and practical aspects

This section addresses the parameter selection for the load alleviation functions as well as practical aspects for the flight operation. For the first aspect, the effect of a fixed MLA deflection is investigated. A fixed MLA deflection implies that the MLA algorithm is not a function of the airspeed. Subsequently, the variation of the GLA delay time is analyzed. The objective of varying the delay time lies in minimizing the wing root bending moment during gust encounters.

Concerning operational aspects, a fatigue damage of a retrofitted aircraft is calculated. The term retrofit means that a passive aircraft – that is produced or in operation – is equipped with load alleviation. A further investigation deals with a load factor threshold for MLA deflection. For any commanded load factor below that certain threshold, the MLA is assumed to be passive. This is potentially beneficial e.g. during take-off where a high maximum lift coefficient is desirable, since an MLA deflection practically reduces that coefficient.

8.1 Fixed MLA deflection

The MLA design in Section 4.2 defines the maximum MLA deflection as a function of the dynamic pressure, unlike the MLA of the Lockheed L-1011 [77]. As stated in Section 4.2, the dependency on the dynamic pressure is expected to cause the 2D load envelopes to be more slender which is seen to be beneficial as explained by the following example.

Figure 8.1 shows 2D load envelopes of the mid wing section (41% half span) of the D150. In the graphs, all load cases mentioned in Section 6.1 are included and all maneuver loads are visualized with scatter markers. The maneuver loads shown in Figure 8.1(a) are obtained using an MLA implemented according to Equation (4.2). The loads in Figure 8.1(b) result when the MLA is fixed to the maximum value of 15° (trailing edge up during pull-ups, trailing edge down during push-downs). The maximum bending moment M_x is indeed in both cases equal. With the variable MLA deflection however, the maneuver load envelope in Figure 8.1(a) is more slender. Furthermore, the area in the dashed square – around the maximum bending moment M_x and torsion moment M_y – requires special attention since load cases with the largest cut loads have a large influence on the structural mass. As apparent, with the variable MLA deflection, there is only one load case within the dashed square. With the fixed MLA deflection on the other hand, there are four load cases found in the dashed square. This means that fewer load cases are considered in the structural optimization for the MLA with variable maximal deflection. From the optimization point of view, this means that the wing structure has to be optimized for fewer loading conditions, so that a potentially lower structural mass would result.

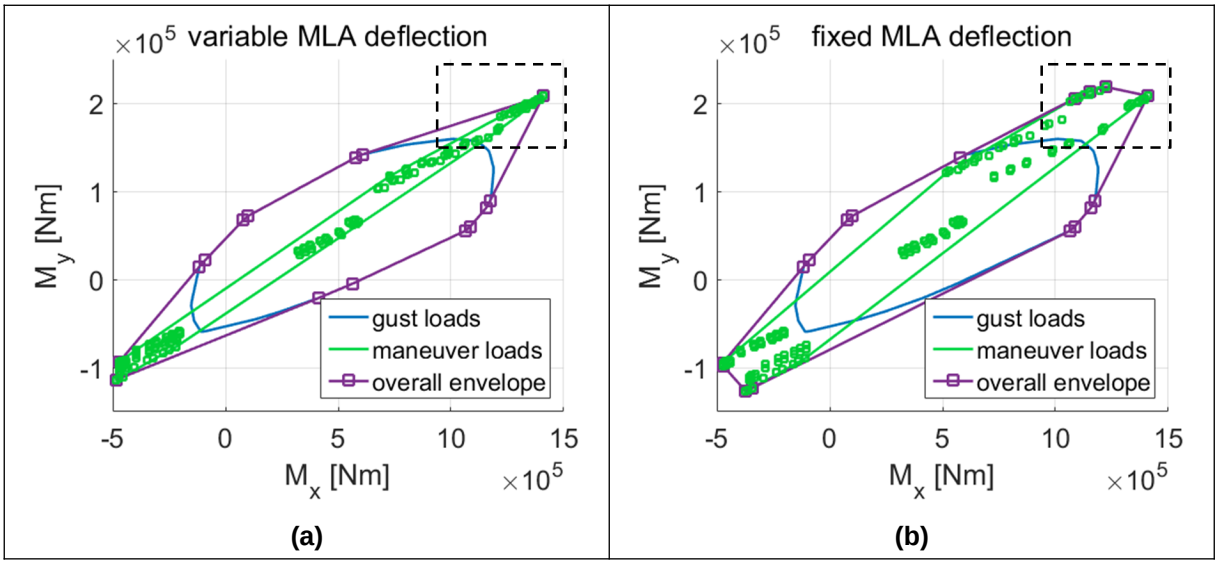

Figure 8.1. 2D load envelope on D150 with variable (a) and fixed (b) deflection

8.2 Variation of GLA delay time

As stated in Section 4.3, the delay time is calculated using the buffer distance x_{wing} shown in Equation (4.5). With this approach, the relative delay with regards to the gust penetration is constant at any airspeed. Otherwise, if a constant buffer time instead of a buffer distance is used, the GLA would likely deflect too early at low speeds and too late at high speeds.

However, by using a buffer distance, its value is still to be defined. In this case, the objective of the selection of the buffer distance is to minimize the root bending moment M_x. For this purpose, gust simulations with different buffer distances are carried out for each reference aircraft, and those evoking the lowest bending moment values are selected for the investigations in Section 6 and 7.

D150 configuration

The investigation on the D150 configuration is carried out with the maximum take-off mass configuration MTmMG (Table 6.1), at 256.0 m/s TAS and 7000 m above sea level. In the gust loads analysis according to Section 6.1, this combination of parameters yields the highest wing root bending moment M_x. Gust simulations are run with a variation of the buffer distance x_{wing} between 12 m and 24 m. For this study, the minimum delay time of 60 ms is neglected that corresponds to the assumption of an ideally fast flight control computer (FCC). Figure 8.2 visualizes the resulting envelopes of the incremental gust loads at the wing root. The wing root bending moment is chosen as the reference parameter since it has a larger impact on the wing box mass compared to e.g. a bending moment at other positions on the wing.

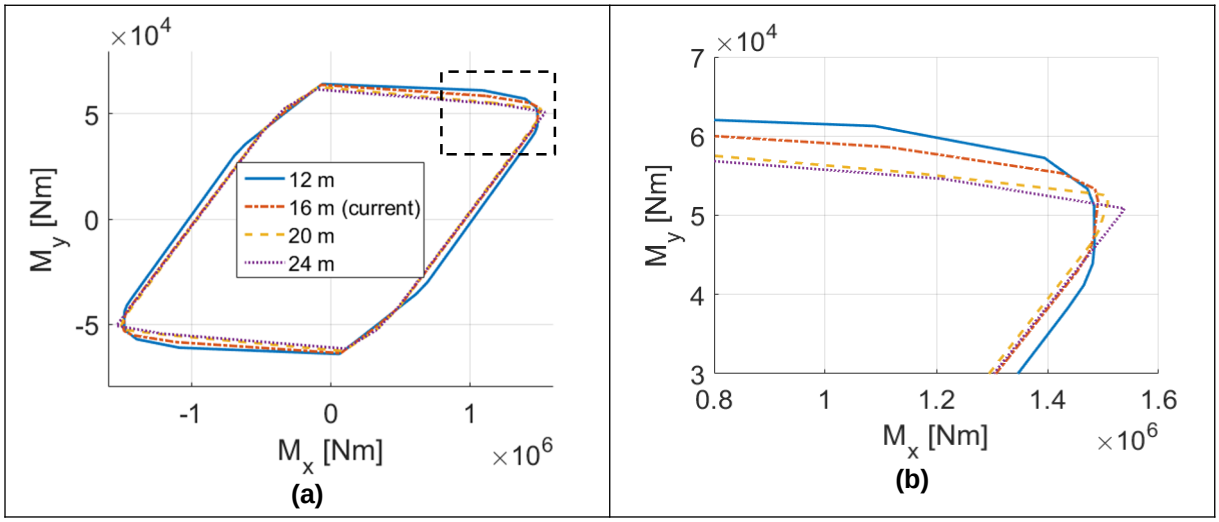

Figure 8.2. Incremental gust load envelope with variation of GLA buffer – D150

It is apparent that the sooner the aileron deflects, the smaller the wing root bending moment becomes. However, a buffer distance of 12 m is not feasible as the effective delay time at 256 m/s TAS would be 47 ms, and it is below the minimum of 60 ms. Compared to the current design with a buffer distance of 16 m, its increase to 24 m would raise the bending moment by 3.2%. On the other hand, the torsion M_y occurring together with the maximum bending moment is decreased by 1.9%. Moreover, with a buffer distance of 24 m, the load envelope has a more pronounced corner at the maximum bending moment.

ALLEGRA configuration

Similar to the D150 configuration, the investigation for the ALLEGRA configuration is conducted with the maximum take-off mass configuration MTmMG (Table 7.1), at 248.7 m/s TAS and 7000 m above sea level. The buffer distance x_{wing} is varied between 14 m and 26 m and the minimum delay time of 60 ms is neglected. Figure 8.3 visualizes the resulting envelopes of the incremental gust loads at the wing root.

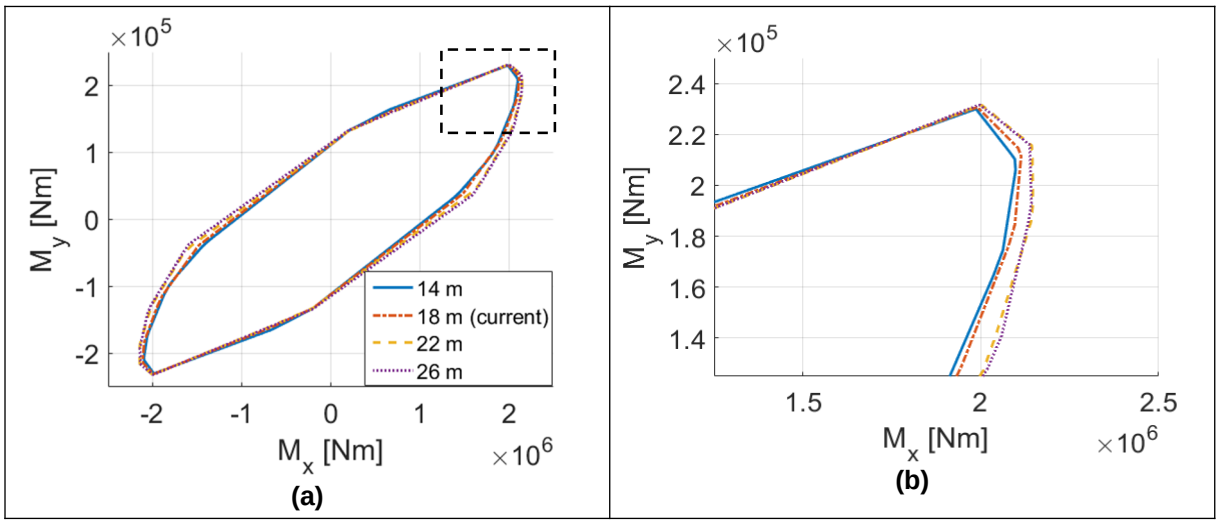

Figure 8.3. Incremental gust load envelope with variation of GLA buffer – ALLEGRA

A similar tendency compared to the D150 configuration is visible: the wing root bending moment M_x is in general smaller with decreasing buffer distance. However, a buffer distance of 14 m is not feasible since the effective delay time at 248.7 m/s TAS would be 56 ms, and it is below the minimum of 60 ms. Compared to the current design with a buffer distance of 18 m, its increase to 22 m or 26 m would cause the bending moment to rise by 1.6% and 1.4% respectively. On the other hand, the increase in maximum torsion M_y is under 0.4% in both cases. Toward the wing tip however, the spread in the bending moment due to the buffer distance variation is expected to be larger since the relative influence of the aileron deflection on the cut loads becomes larger.

8.3 Retrofit of passive aircraft with load alleviation

Another investigation is a so-called retrofit of a passive reference aircraft. The retrofit is defined as implementation of MLA and GLA on a passive aircraft without further structure re-optimization. The benefit of a retrofit is seen in the fatigue life extension of an existing aircraft, especially if high turbulence loads are expected due to flights at low altitudes, e.g. during coast patrol, research or firefighting missions. It is assumed that the aileron actuators do not need to be significantly reinforced, as shown in Subsection 6.2.2 and 7.2.2. The effect of the retrofit on fatigue damage is estimated for both reference aircraft. The fatigue loads are assumed to emerge due to one reference flight cycle with the turbulence and the ground-air-ground cycle described in Subsection 6.3.1 and 7.3.1 respectively.

D150 configuration

Figure 8.4 visualizes the stress σ_1 and aileron hinge moment $M_y(\mathrm{ail})$ collectives of the retrofitted aircraft during the climb phase. On the wing, the stress collectives of the retrofitted aircraft have similar trends to those of the active aircraft, see Figure 8.4(a) and (b). This is marked by the lower stress amplitudes in general. Concerning the collectives on the HTP, the retrofitted aircraft has slightly higher stress levels than the passive aircraft, and the graph lies closer to that of the active aircraft. However, the aileron hinge moment graph of the retrofitted aircraft lies closer to that of the passive aircraft.

Table 8.1 lists the accumulated fatigue damage values due to turbulence in one reference flight. In turbulence, a retrofit of the passive aircraft would significantly increase the fatigue life of the wing, whereas the HTP would have a slightly shorter fatigue life. To obtain the total fatigue damage evoked in one reference flight cycle, the fatigue damage from a ground-air-ground cycle with MLA according to Subection 6.3.1 is added, and Table 8.1 shows the resulting fatigue damage values. With the maximum damage value on the retrofitted aircraft of $2.71 \cdot 10^{-12}$, its overall fatigue life is expected to be 2.81 times longer compared to the passive aircraft which has the largest damage value of $7.62 \cdot 10^{-12}$. This fatigue life extension to 281% is significantly larger than the fatigue life benefit on the active aircraft (28%). This results from the lower stress levels on the retrofitted aircraft in general compared to the active aircraft due to its higher material thicknesses.

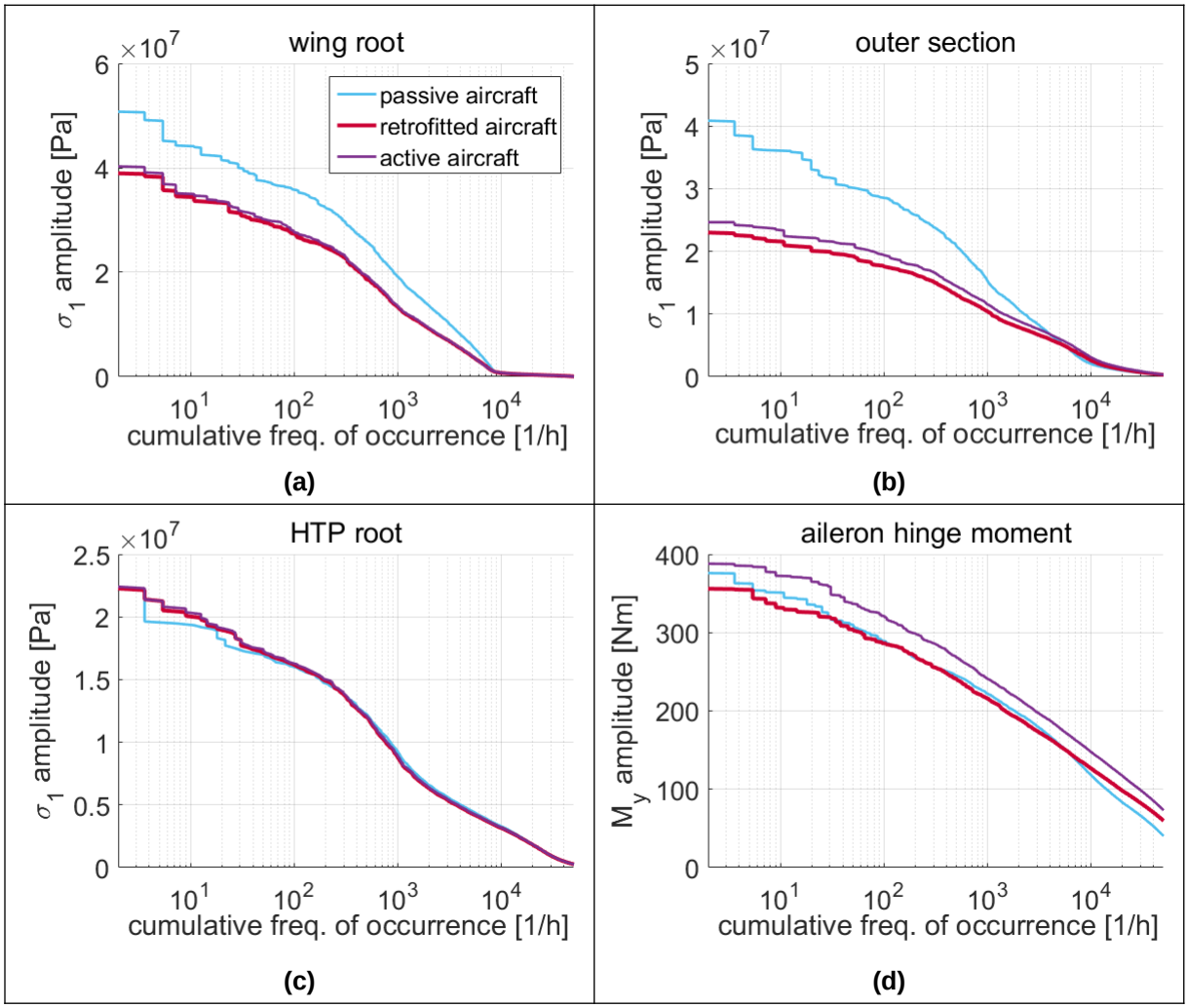

Figure 8.4. Stress and hinge moment collectives during the climb phase of D150

Table 8.1. Fatigue damage overview of retrofitted D150

Observed shell element	Turbulence damage		Total fatigue damage	
	Retrofitted aircraft	Passive aircraft	Retrofitted aircraft	Passive aircraft
Wing root	$6.34 \cdot 10^{-15}$	$2.15 \cdot 10^{-12}$	$2.71 \cdot 10^{-12}$	$7.62 \cdot 10^{-12}$
Outer wing section	$2.12 \cdot 10^{-22}$	$1.05 \cdot 10^{-15}$	$3.91 \cdot 10^{-13}$	$3.25 \cdot 10^{-12}$
HTP root	$1.85 \cdot 10^{-20}$	$2.67 \cdot 10^{-21}$	$1.85 \cdot 10^{-20}$	$2.67 \cdot 10^{-21}$

ALLEGRA configuration

Figure 8.5 shows the strain ϵ_1 and aileron hinge moment $M_y(\mathrm{ail})$ collectives of the retrofitted aircraft during the climb phase. As apparent in Figure 8.5(a) and (b), the strain collectives of the wing of the retrofitted aircraft show similar shapes to those of the active aircraft. However, the strain levels of the retrofitted aircraft are lower in general. On the HTP, the collective of the retrofitted aircraft shows slightly higher strain levels than the passive aircraft,

and the agreement with the curve of the active aircraft is higher. Analogous to the strain amplitudes on the wing, the aileron hinge moment collective of the retrofitted aircraft shows a trend more similar to that of the of the active aircraft.

Table 8.2 lists the accumulated fatigue damage values due to turbulence during one reference flight. In turbulence, a retrofit of the passive aircraft would extend the fatigue life of the wing significantly, whereas the fatigue life of the HTP would slightly decrease. To acquire the total fatigue damage caused in one reference flight cycle, the fatigue damage emerging from a ground-air-ground cycle with MLA according to Subection 7.3.1 is superposed, and Table 8.2 shows the results. With the maximum damage value on the retrofitted aircraft of $2.78 \cdot 10^{-24}$, its overall fatigue life is expected to be 11.9 times longer compared to the passive aircraft with the largest damage value of $3.32 \cdot 10^{-23}$. This fatigue life improvement to 1190% is significantly larger than the fatigue life benefit on the active aircraft (12%). In practice however, the factor 11.9 is unlikely to be realized since other components such as control surfaces might reach the end of their service life earlier. Analogous to the D150 configuration, this difference results from the lower strain levels on the retrofitted aircraft in general compared to the active aircraft due to its higher material thicknesses.

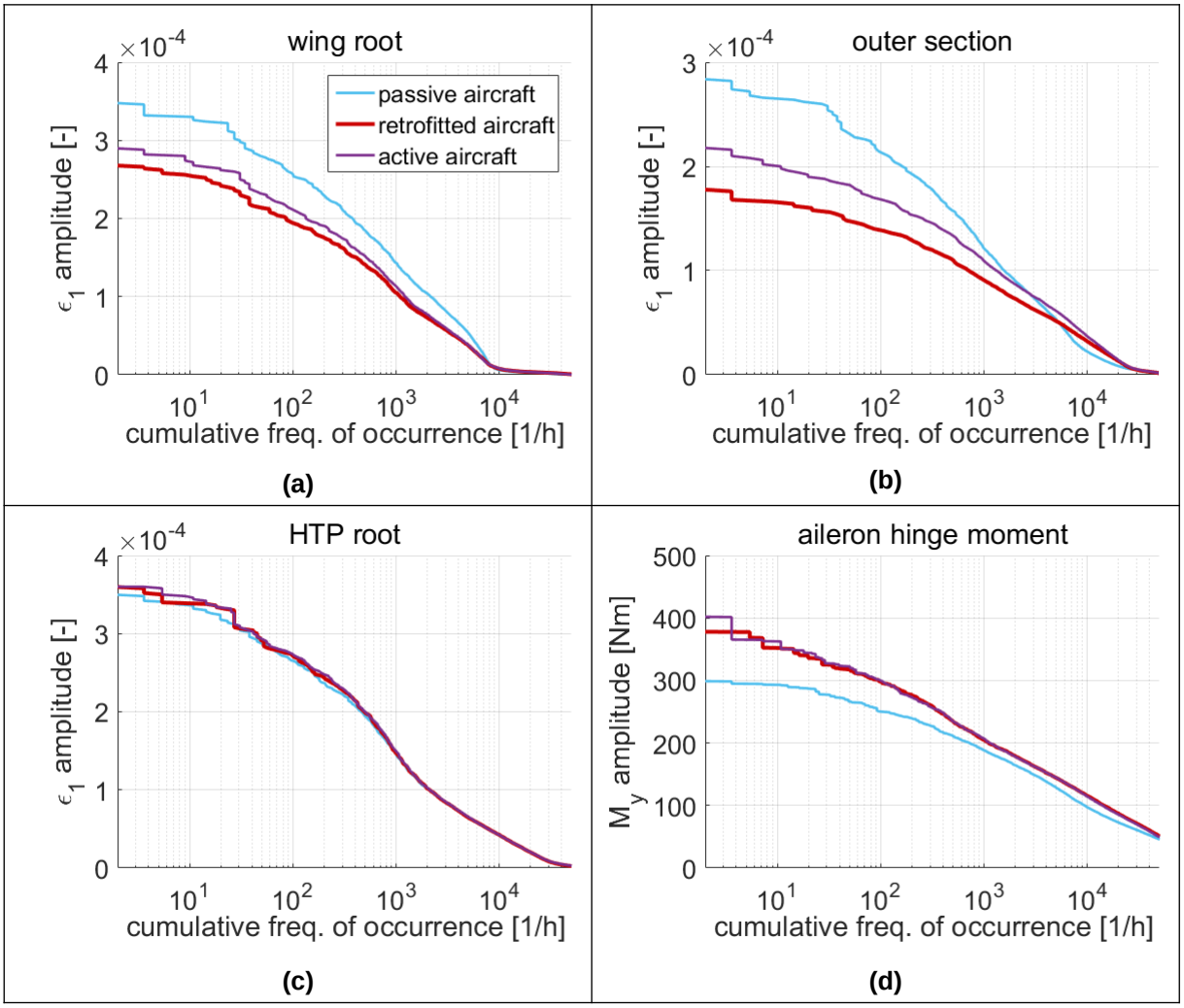

Figure 8.5. Strain and hinge moment collectives during the climb phase of ALLEGRA

Table 8.2. Fatigue damage overview of retrofitted ALLEGRA

Observed shell element	Turbulence damage		Total fatigue damage	
	Retrofitted aircraft	Passive aircraft	Retrofitted aircraft	Passive aircraft
Wing root	$4.05 \cdot 10^{-27}$	$2.74 \cdot 10^{-23}$	$2.78 \cdot 10^{-24}$	$3.32 \cdot 10^{-23}$
Outer wing section	$5.36 \cdot 10^{-32}$	$2.83 \cdot 10^{-26}$	$4.24 \cdot 10^{-27}$	$8.01 \cdot 10^{-26}$
HTP root	$9.87 \cdot 10^{-34}$	$6.24 \cdot 10^{-34}$	$9.87 \cdot 10^{-34}$	$6.24 \cdot 10^{-34}$

In general, the maximum benefit of a retrofit is gained if it is implemented on newly delivered aircraft. Depending on the logistics and effort to implement the retrofit, it can still be beneficial for aircraft that have been in operation. The terms logistics and effort implies whether the aircraft has to be flown to the manufacturer's site to undergo the retrofit, and how extensive the update of the FCC as well as the subsequent tests are expected to be.

8.4 Load factor threshold for MLA activation

In the fatigue damage accumulations described in Subsection 6.3.3 and 7.3.3, the MLA is assumed to always be active. This means that for every commanded vertical load factor other than 1.0, the ailerons are deflected by MLA. However, if there is a load factor threshold for the MLA, below which it should remain inactive, the effects on the fatigue life of the active aircraft are negative. This is because small fluctuations in the load factor below the threshold would evoke larger fluctuations in the stresses compared to an aircraft without the MLA threshold. Nevertheless, an implementation of such an MLA threshold is potentially beneficial in the flight operation. As an example: during take-off, a high maximum lift coefficient is desirable since it helps in reducing the take-off roll distance and the take-off speed. However, an MLA deflection during take-off means that the lift on a fraction of the lifting surface is reduced, and this reduces the overall lift coefficient.

As reference, the ground-air-ground cycle with a maximum load factor of 1.3 is considered, as defined in Subsection 6.3.1 and 7.3.1 respectively. For this study, it is assumed that the load factor threshold for MLA is higher than 1.3, so that the ailerons of the active aircraft are not deflected yet. Without MLA threshold, the ailerons are deflected by -2.5° (trailing edge up) according to Equation (5.7). To obtain the total fatigue damage evoked in one reference flight cycle, turbulence damage values of the active aircraft from Table 6.10 and Table 7.9 are added respectively. Table 8.3 and Table 8.4 list the fatigue damage values resulting from the ground-air-ground cycle and the resulting total fatigue damage.

Table 8.3. Fatigue damage on active D150 with MLA threshold

Observed shell element	Ground-air-ground cycle damage		Total fatigue damage	
	With MLA threshold	No MLA threshold	With MLA threshold	No MLA threshold
Wing root	$1.20 \cdot 10^{-11}$	$5.93 \cdot 10^{-12}$	$1.20 \cdot 10^{-11}$	$5.94 \cdot 10^{-12}$
Outer wing section	$4.63 \cdot 10^{-11}$	$5.70 \cdot 10^{-12}$	$4.63 \cdot 10^{-11}$	$5.70 \cdot 10^{-12}$
HTP root	$5.50 \cdot 10^{-28}$	$2.10 \cdot 10^{-27}$	$4.58 \cdot 10^{-21}$	$4.58 \cdot 10^{-21}$

Table 8.4. Fatigue damage on active ALLEGRA with MLA threshold

Observed shell element	Ground-air-ground cycle damage		Total fatigue damage	
	With MLA threshold	No MLA threshold	With MLA threshold	No MLA threshold
Wing root	$6.10 \cdot 10^{-23}$	$2.97 \cdot 10^{-23}$	$6.10 \cdot 10^{-23}$	$2.97 \cdot 10^{-23}$
Outer wing section	$1.50 \cdot 10^{-23}$	$1.24 \cdot 10^{-24}$	$1.50 \cdot 10^{-23}$	$1.24 \cdot 10^{-24}$
HTP root	$4.21 \cdot 10^{-38}$	$4.31 \cdot 10^{-38}$	$2.26 \cdot 10^{-33}$	$2.26 \cdot 10^{-33}$

As apparent, with an MLA threshold, the fatigue damage values on both reference aircraft increase significantly. On the D150 configuration, an implementation of an MLA threshold would lead to a shorter fatigue life by a factor of 7.79, resulting from the highest damage values of $5.94 \cdot 10^{-12}$ without MLA threshold and $4.63 \cdot 10^{-11}$ with the threshold.

On the ALLEGRA configuration, the aircraft with MLA threshold would have a fatigue life that is 2.05 times shorter compared to the aircraft with no threshold. For detailed calculations, the effect of the high lift devices on the spanwise lift distribution as well as the element stresses or strains need to be considered.

9 Evaluations, conclusions and outlook

9.1 Evaluations

Evaluation of method

An aircraft pre-design method to investigate the influence of load alleviation on structural mass and fatigue has been developed and discussed. The method has been applied on two reference aircraft: the conventional D150 configuration and the ALLEGRA configuration with forward swept wing.

The developed method enables calculations of differences in the structural masses and fatigue behaviors between the active and passive aircraft. In the structural optimization, the masses converge according to the criteria defined in Section 3.7. In the last optimization cycle, the RMS of change in the material thicknesses is below 4.0%. This change is a residual uncertainty in the material thickness convergence. This uncertainty correlates with the load case selection algorithm, especially if the dynamic gust loads are dominant. Nevertheless, the uncertainty is accepted in order to reduce the number of load cases for the structural optimization to approximately 60. Moreover, a mass convergence to the last kilogram is not practicable either. Hence, at a certain point of the design process, a freeze of the structural layout and a definition of target loads are advisable.

In the fatigue analysis, damage due to turbulence and ground-air-ground cycles in a reference flight mission is obtained. Although the fatigue analysis method cannot provide a quantitative result (e.g. the aircraft can survive x flight cycles), it enables a comparison between the active and passive aircraft. With a discretization of the flight mission into three phases (climb, cruise and descent), an insight into the severeness of turbulence damage in each phase is gained. A factor of uncertainty in the turbulence damage lies in the random phase distribution during the generation of the vertical wind speed in the time domain. This means, a different phase distribution yields another time history of the vertical wind speed that in turn results in different load collectives. To eliminate this uncertainty in the comparison between the active and passive aircraft, the time history of the vertical wind speed in each flight phase is identical for the active and passive aircraft.

The total computing time for the loads and optimization process of the D150 configuration is 40.2 hours for ten cycles, or 4.02 hours per cycle in average. In each cycle, an average of 2.52 hours fall into the gust load calculations. On the ALLEGRA configuration, the computing time is 35.6 hours for seven cycles, or 5.09 hours per cycle in average. The gust load calculations make up 3.47 hours per cycle that is longer compared to D150 due to the larger number of aerodynamic elements (1176 instead of 939). The loads analysis with MSC.Nastran is run on one processor with 2600 MHz clock frequency. The structural optimization is carried out using eight processors and 16 GB of allocated RAM. The computing time of the turbulence and fatigue analysis is relatively short with 10 minutes.

Although the dynamic gust analysis requires the majority of the computing time, it is worth considering since gust loads always appear among the load cases selected for the structural optimization, see Figure 3.4. This is also the case if the largest bending moments are reached during maneuvers. In addition, the developed method provides a first insight into how large the alleviated gust loads are compared to the alleviated maneuver loads. The findings might help in the decisions of how to retune the control algorithm in the pre-design phase, e.g. to maximize the mass benefit, that is more cost-efficient compared to doing so at a later stage.

Evaluation of results

As described in Chapter 6 and 7, the consideration of load alleviation within the aircraft pre-design process can simultaneously yield a reduction of wing structural mass and an overall fatigue life extension. Concerning the wing structural mass reduction on the backward swept D150 configuration, 130.5 kg (0.18% of MTOM, 0.32% of OEM) can be saved in total. On the forward swept ALLEGRA configuration, the wing mass decrease is 410.4 kg (0.56% of MTOM, 0.94% of OEM). As a comparison: Wildschek et al. [100] stated in 2013 that on a large blended wing-body configuration, load alleviation using a feed-forward L_∞-optimal control can yield a mass reduction by 0.5% of the maximum take-off mass. An aspect to be remarked on is that Wildschek used the elevators, inner, outer spoilers and the ailerons as free parameters for the controller synthesis. Hence, there were more degrees of freedom available in tuning the control algorithm. Besides, the deflection rate of the control surfaces were significantly higher with up to 300°/s that would eliminate potential phase shifts due to a rate limitation. A further reference is the active load alleviation system on the Lockheed C-5A [80] documented in 1976. The system was initially developed to extend the fatigue life of the structure, however it was discarded and a structural modification was introduced. The structural modification increased the empty mass of the aircraft by 5.5%. However, it cannot be concluded that the active load alleviation can yield that mass reduction since the structure of the C-5A is not likely to be completely re-optimized after discarding the load alleviation.

Concerning fatigue, a comparison with literature results is only possible between the retrofitted and passive aircraft since no data of fatigue comparisons with a separate optimization of the active aircraft could be found. The retrofitted D150 aircraft is expected to have a fatigue life improvement by a factor of 2.81 compared to the passive counterpart. For the ALLEGRA configuration, the fatigue life is expected to increase by a factor of 11.9 through retrofit. However, with the assumptions made, these fatigue results are obtained using S-N curves with very flat slopes, so that small differences in the load amplitudes result in huge differences in the fatigue damage accumulation. If S-N curves with steeper slopes are used, these differences are expected to be smaller. As a comparison, on the Lockheed C-5A the active load alleviation yields a fatigue life improvement of 25-50%, according to Disney [17] in 1977. On a business jet configuration investigated by Paletta [69] in 2011, the fatigue life is extended by 44-67%. Such fatigue life extensions are expected to be more beneficial if the aircraft undergo many flight cycles on short routes. Otherwise, the benefit of a service life extension from 30 to e.g. 40 years might be limited due to the availability of newer, more profitable aircraft.

9.2 Conclusions

The investigations featuring the design process serve to gain an insight into the benefits of load alleviation for a given aircraft in the pre-design phase before it advances to the next design stage. The analyses cover multiple disciplines (loads, aeroelasticity, aerodynamics, structure, flight mechanics, control theory, fatigue) and range from loads analysis, structural optimization to fatigue analysis. The consideration of load alleviation in an early design stage would also lower the risk of having to change the structure extensively in later stages. Moreover, dynamic gusts with GLA are worth considering since they give an insight into how large the alleviated gust loads are compared to the alleviated maneuver loads.

During the investigations, the following aspects emerge and are seen as worth mentioning:

- An implementation of load alleviation can reduce the flight loads, wing structural mass and extend the wing's fatigue life in turbulent weather. For ground-air-ground cycles, the wing of the active aircraft tends to receive more fatigue damage than a passive one. Overall however, the active aircraft show fatigue life improvement compared to the passive counterpart. For the reference missions, the fatigue life of the active aircraft increases by 28% (D150) and 12% (ALLEGRA) respectively – in addition to the mass benefit.
- The passive aircraft reaches the highest aileron hinge moments during maneuvers. Gust encounters evoke the largest hinge moments on the active aircraft.
- To maintain the fatigue life improvement of the active aircraft, there must be no threshold for the MLA. This implies that the MLA has to deflect the ailerons at every commanded load factor other than 1.0. Otherwise, the active aircraft with MLA threshold would have a shorter fatigue life compared to the passive counterparts.
- Compared to the passive aircraft, a retrofit yields additional fatigue life – as long as the passive structure can withstand the alleviated design loads. These alleviated design loads might evoke new stress peaks due to slightly different ratios between the bending and torsion moments.
- A fatigue life improvement at one observed position as a result from any measure can occur simultaneously with a deterioration at another position. Thus, for a global analysis, several positions should be observed simultaneously, and the highest fatigue damage value determines the aircraft's fatigue life.
- A quantitative fatigue prediction in aircraft pre-design is only sensible if the fatigue relevant parts on the wing are known and modeled – together with the corresponding stress/strain amplification factors, otherwise the result would practically be infinite fatigue life.
- On forward swept wing configurations, the short period mode becomes unstable long before aeroelastic divergence occurs. This is caused by a shift of the aerodynamic center resulting from the bending-torsion-coupling, and the shift becomes larger with increasing dynamic pressure. The most effective countermeasure to this would be to

build the wing as stiff as possible to avoid the wingtip nose-up twist due to bending-torsion-coupling. Otherwise, aeroelastic tailoring can help in reducing the nose-up twist to a certain degree by trading bending stiffness against coupling stiffness.

9.3 Discussion of contribution

As elaborated in Section 1.3, the main objective of this thesis it to develop a method that considers load alleviation in aircraft pre-design and its influence on design loads, structural mass and fatigue. At this point, it can be concluded that the load alleviation functions for the aircraft preliminary design stage have been implemented successfully. On one hand, the algorithms for the MLA and GLA are simple so that they are easily understandable and transferable to other aircraft configurations. On the other hand, the load alleviation effectively reduces the wing bending moments without excessively increasing the torsions compared to the passive counterpart. With load alleviation, a clear trend of decrease in the wing box mass is obtained. While the mass decrease can be estimated accurately, there are residual fluctuations in the material thickness distributions between the iteration cycles. Furthermore, the effect of load alleviation on the fatigue life of the aircraft has also been analyzed successfully using a reference flight mission. For a more comprehensive investigation however – e.g. for one aircraft throughout its service life – a distribution of various flight missions, the turbulence intensities as well as more detailed S-N curves are necessary. Compared to the state of the art, the developed design process provides an insight into the influence of load alleviation on the fatigue behavior of the aircraft – alongside its effect on the wing box mass.

Beside the main objective, several minor aspects have been addressed:

- The developed design process has successfully been applied to a forward swept wing configuration. It is shown that the forward swept wing configuration has different sizing load cases and that load alleviation has a larger impact on its wing box mass as well as fatigue life. Moreover, the potential flight mechanic instability of forward swept wing configurations due to its aeroelasticity has been investigated, and a solution to prevent the instability in the flight envelope has been developed.
- In the analyses, elastic aircraft, unsteady aerodynamics, active control as well as continuous turbulence have been considered. Especially for the fatigue analysis, the consideration of those aspects gives a more accurate insight into the load collectives of the particular aircraft compared to standardized load spectra.
- A retrofit of passive aircraft has been investigated successfully. This aspect serves as comparison of fatigue life extension to literature since no references dealing with separately optimized active aircraft were found.

9.4 Outlook

There are several potential aspects that could be considered in the future. The first one concerns the design load calculations. In this aspect, the load case variety can be extended to reproduce the design load cases of a certified aircraft as close as possible. For the wing, this includes landing, roll and asymmetric load cases as well as gust cases with extended airbrakes. For the empennage optimization, checked maneuvers and loads caused by airbrake wake turbulence during landing deceleration can also be considered. However, the latter cannot be modeled with DLM aerodynamics anymore.

The airbrakes – or spoilers – play a relevant role and can improve the effectiveness of MLA and GLA. To consider the effect of spoiler deflections with a reliable aerodynamic modeling, the DLM has to be corrected e.g. based on CFD calculations. CFD can also be used to better determine the aerodynamic effectiveness of trailing edge control surfaces that is assumed to be 0.7 in this thesis. For transonic Mach numbers, a DLM correction based on CFD is also worth considering since e.g. the torsion moments are expected to be affected by local supersonic areas on the lifting surfaces.

For the proposed GLA, the measured angle of attack increment at the nose exactly represents the change in angle of attack that will hit the wing since 1D turbulence is assumed. However, in case of a 2D turbulence where the vertical wind changes in lateral direction, the wingtip does not necessarily experience the same turbulence profile as the aircraft nose. At this point, a correlation function between the angle of attack increment at the nose and e.g. at the wingtip should be introduced. Besides, a more sophisticated GLA can be synthesized by optimization, as described by Wildschek et al. [101]. The optimization objectives can be minimization of overall stress/strain amplitudes, minimization of wing box mass or minimization of hinge moments. However, the methods optimizing such control algorithms require that the aircraft's dynamics with all possible mass configurations and flight conditions are considered.

Another gust and turbulence sensor that can be used is a light detection and ranging (LIDAR) sensor. A LIDAR system can detect the wind field up to 300 m ahead of the aircraft [26]. This gives the GLA an additional reaction time of approx. 1 s depending on the weather that affects the LIDAR signal quality. This additional second opens up further possibilities in the development of GLA algorithms.

As described in Section 4.3, the GLA in this thesis does not consider feedback quantities of the structural elasticity. If those are included in the control algorithm however, the damping of elastic modes can be increased [9] that is beneficial for the fatigue life. Therefore, an inclusion of a mode damper based on a feedback control algorithm is worth considering – as long as the turbulence fatigue damage is not significantly outbalanced by the fatigue damage from ground-air-ground cycles.

In the structural optimization, aeroelastic tailoring can be considered as well, as described by Dillinger [16] and by Handojo et al. [37]. However, the simultaneous consideration of a large number of load cases, dynamic loads and aeroelastic/flight mechanical constraints in one optimization run with aeroelastic tailoring would create a challenge in computing time and random-access memory (RAM) requirements.

Concerning fatigue analysis in turbulence, the scenario is that the +1g flight loads stay constant in the observation period of time, and the turbulence loads are added to the steady flight loads. This means, load cycles with higher amplitudes have a lower stress/strain ratio compared to the cycles with lower amplitudes. To take those changes of stress/strain ratios into account, comprehensive data of S-N curves are necessary, so that an interpolation between the different stress ratios for the various amplitudes is possible. This will likely result in steeper slopes of the S-N curves, with it a larger contribution of turbulence loads (high cycles, low amplitudes) and a smaller contribution of ground-air-ground loads (low cycles, high amplitudes). Besides, further flight missions as well as a probability distribution of turbulence intensities can be taken into account. For composite aircraft, a more detailed fatigue models as applied by Rajpal et al [76] can be considered.

For airlines, one important cost factor is the aircraft inspection interval. However, the resulting fatigue life extension of active aircraft does not ensure the possibility to increase the inspection interval yet. For this aspect, further analyses of aircraft systems such as control surface actuators are necessary, especially since the active aircraft deflect the control surfaces significantly more often.

Moreover, the potential benefit through fatigue life extension also needs to be assessed while considering the expected distribution of the flight mission duration. As an example: if an aircraft only flies long distances, the expected service life can be extended from 30 to 40 years. Within 40 years however, there might be newer, more profitable aircraft so that the benefit of the longer service life is reduced. On the other hand, if an aircraft only flies short distances, the initial expected service life might be e.g. 15 years, and its extension to 20 years might be more beneficial.

For the pre-design stage, a consideration of a more comprehensive design load spectrum and aerodynamic modeling is expected to have the largest impact on the design. For the fatigue analysis, it is advisable to take probability distributions of turbulence intensities and various flight missions into account.

Bibliography

[1] Airbus, “Orders and Deliveries,” *Order and Deliveries*. [Online]. Available: https://www.airbus.com/aircraft/market/orders-deliveries.html. [Accessed: 14-May-2019].

[2] Alam, M., “Gust Load Alleviation System for BWB (Blended Wing Body) Flexible Aircraft,” Master’s Thesis, Czech Technical University, Prague, 2013.

[3] Albano, E., and Rodden, W., “A Doublet Lattice Method for Calculating Lift Distributions on Oscillating Surfaces in Subsonic Flows,” *AIAA Journal*, vol. 7, no. 2, 1968.

[4] Bramsiepe, K., Handojo, V., Meddaikar, Y. M., Schulze, M., and Klimmek, T., “Loads and Structural Optimisation Process for Composite Long Range Transport Aircraft Configuration,” presented at the AIAA Aviation Forum, Multidisciplinary Analysis and Optimization Conference, Atlanta, Georgia, USA, 2018.

[5] Bramsiepe, K., Voß, A., and Klimmek, T., “Parametrische Aeroelastische Modellierung einer Nurflügelkonfiguration,” Internal Report DLR-IB-AE-GO-2016-241, DLR, Institute of Aeroelasticity, Göttingen, 2016.

[6] Britt, R., Jacobson, S., and Arthurs, T., “Aeroservoelastic Analysis of the B-2 Bomber,” *Journal of Aircraft*, vol. 37, no. 5, pp. 745–752, 2000.

[7] Brockhaus, R., Alles, W., and Luckner, R., *Flugregelung*. Heidelberg: Springer, 2011.

[8] Burlion, L., Poussot-Vassal, C., Vuillemin, P., Leitner, M., and Kier, T., “Longitudinal Manoeuvre Load Control of Flexible Large-Scale Aircraft,” *Preprints of the 19th World Congress - The International Federation of Automatic Control, Cape Town, South Africa*, 2014.

[9] Burris, P., and Bender, M., “Aircraft Load Alleviation and Mode Stabilization,” Technical Report AFFDL-TR-68-161, Air Force Flight Dynamics Laboratory, Wright-Patterson Air Force Base, Ohio, 1969.

[10] Capello, E., Guglieri, G., and Quagliotti, F., “A Comprehensive Robust Adaptive Controller for Gust Load Alleviation,” *The Scientific World Journal*, 2014.

[11] Cheung, R. C. M., Castrichini, A., Rezgui, D., Cooper, J. E., and Wilson, T., “Wind Tunnel Testing of Folding Wingtip Devices for Gust Loads Alleviation,” presented at the International Forum on Aeroelasticity and Structural Dynamics, Como, Italy, 2017.

[12] Cooper, J., “Introduction to Aeroelasticity and Loads - Short Course for DLR,” Göttingen, 2015.

[13] Crimaldi, J., Britt, R., and Rodden, W., “Response of B-2 Aircraft to Nonuniform Spanwise Turbulence,” *Journal of Aircraft*, vol. 30, no. 5, pp. 652–659, 1993.

[14] Daniel, I. M., and Ishai, O., *Engineering Mechanics of Composite Materials*. Oxford University Press, 2006.

[15] Dean, J., Clifton, J., Bodkin, D., and Ratcliff, C., “High Resolution CFD Simulations of Maneuvering Aircraft Using the CREATE-AV/Kestrel Solver,” presented at the 49th AIAA Aerospace Sciences Meeting including the New Horizons Forum and Aerospace Exposition, Orlando, Florida, USA, 2011.

[16] Dillinger, J. K. S., “Static Aeroelastic Optimization of Composite Wings with Variable Stiffness Laminates,” Doctoral Thesis, Delft University of Technology, Delft, 2014.

[17] Disney, T., “C-5A Active Load Alleviation System,” *Journal of Spacecraft*, vol. 14, no. 2, 1977.

[18] Ekberg, A., “Palmgren - Miner’s Rule,” Chalmers University of Technology, Göteborg, 1998.

[19] European Aviation Safety Agency, “CS23 - Certification Specifications for Normal, Utility, Aerobatic, and Commuter Category Aeroplanes - Amendment 4.” 2015.

[20] European Aviation Safety Agency, “CS25 - Certification Specifications and Acceptable Means of Compliance for Large Aeroplanes - Amendment 23.” 2019.

[21] FEA cluster, “CalculiX USER’S MANUAL - Von Mises Equivalent Strain,” 2016. [Online]. Available: http://www.feacluster.com/CalculiX/cgx_2.11/doc/cgx/node194.html. [Accessed: 12-Oct-2018].

[22] Federal Aviation Administration, “Determining the Fatigue Life of Composite Aircraft Structures Using Life and Load-Enhancement Factors,” Technical Report DOT/FAA/AR-10/6, U.S. Department of Transportation, 2011.

[23] Federal Aviation Administration, “FAR Part 25 Sec. 25.341 effective as of 03/11/1996,” *Code of Federal Regulations*, 11-Mar-1996. [Online]. Available: http://rgl.faa.gov/Regulatory_and_Guidance_Library/rgFAR.nsf/0/156CCF55583A0AC985256672004EC0D4?OpenDocument. [Accessed: 09-Sep-2019].

[24] Federal Aviation Administration, “FAR Part 25 Sec. 25.341 effective as of 08/20/1990,” *Code of Federal Regulations*, 20-Aug-1990. [Online]. Available: http://rgl.faa.gov/Regulatory_and_Guidance_Library/rgFAR.nsf/0/D60119A72A57DF4585256672004EBDDA?OpenDocument. [Accessed: 09-Sep-2019].

[25] Federal Aviation Administration, “Statistical Loads Data for the Airbus A-320 Aircraft in Commercial Operations,” Technical Report DOT/FAA/AR-02/35, 2002.

[26] Fezans, N., and Joos, H. D., “Combined Feedback and LIDAR-based Feedforward Active Load Alleviation,” presented at the AIAA Atmospheric Flight Mechanics Conference, AIAA AVIATION Forum, 2017.

[27] Fidkowski, K., Engelsen, F., Willcox, K., and Kroo, I., “Stochastic Gust Analysis Techniques for Aircraft Conceptual Design,” presented at the 12th AIAA/ISSMO Mulidisciplinary Analysis and Optimization Conference, 2008.

[28] Fonte, F., Ricci, S., and Mantegazza, P., “Gust Load Alleviation for a Regional Aircraft Through a Static Output Feedback,” *Journal of Aircraft*, vol. 52, no. 5, 2015.

[29] Fuelplanner, “Fuelplanner.” [Online]. Available: http://fuelplanner.com/index.php. [Accessed: 31-Jul-2018].

[30] Fuller, J., “Evolution of Airplane Gust Loads Design Requirements,” *Journal of Aircraft*, vol. 32, no. 2, 1995.

[31] Giesing, J. P., Kálmán, T. P., and Rodden, W. P., “Subsonic Steady and Oscillatory Aerodynamics for Multiple Interfering Wings and Bodies,” *Journal of Aircraft*, vol. 9, no. 10, 1972.

[32] Giesseler, H.-G., Kopf, M., Faulwasser, T., Varutti, P., and Findeisen, R., “Gust Load Alleviation Based on Model Predictive Control,” presented at the International Forum on Aeroelasticity and Structural Dynamics (IFASD), Bristol, UK, 2013.

[33] Grover, H. J., *Fatigue of Aircraft Structures*. Naval Air Systems Command - Department of the Navy, 1966.

[34] Handojo, V., and Klimmek, T., “ALLEGRA M 3.3.2 Bericht: Böensimulation des elastischen Flugzeugs mit Basisverfahren,” Internal Report IB232-2015 J06, DLR - Institut für Aeroelastik, Göttingen, 2015.

[35] Handojo, V., and Klimmek, T., “Böenlastanalyse der vorwärts gepfeilten ALLEGRA-Konfiguration,” presented at the Deutscher Luft- and Raumfahrtkongress, Rostock, Germany, 2015.

[36] Handojo, V., Klimmek, T., Quero-Martin, D., and Voß, A., “ALLEGRA M 3.3.3 Bericht: Böensimulation des elastischen Flugzeugs mit ROM-Verfahren,” Internal Report DLR-IB-AE-GO-2016-52, DLR - Institut für Aeroelastik, Göttingen, 2016.

[37] Handojo, V., Lancelot, P., and De Breuker, R., “Implementation of Active and Passive Loads Alleviation Methods on a Generic Mid-Range Aircraft Configuration,” presented at the AIAA Aviation Forum, Multidisciplinary Analysis and Optimization Conference, Atlanta, Georgia, USA, 2018.

[38] Harlow, F. H., and Welch, J. E., “Numerical Calculation of Time-Dependent Viscous Incompressible Flow of Fluid with Free Surface,” *The Physics of Fluids*, vol. 8, no. 12, 1965.

[39] Hoblit, F., “Effect of Yaw Damper on Lateral Gust Loads in Design of the L-1011 Transport,” *AGARD-AG-175 - Active Control Systems for Load Alleviation, Flutter Suppression and Ride Control*, pp. 3–10, 1974.

[40] Hoblit, F., *Gust Loads on Aircraft: Concepts and Applications*. Washington, D.C.: AIAA, 1988.

[41] Hönlinger, H., and Zimmermann, H., “Structural Aspects of Active Control Technology,” presented at the Flight Mechanics Panel Symposium, Torino, Italy, 1994.

[42] Houbolt, J., “Design Manual for Vertical Gusts Based on Power Spectral Techniques,” Technical Report AFFDL-TR-70-106, Air Force Flight Dynamics Laboratory, Wright Patterson Airforce Base, Ohio, 1970.

[43] Hunsaker, J., and Wilson, E., “Report on Behavior of Aeroplanes in Gusts,” *NACA Report No. 1*, 1915.

[44] IJsselmuiden, S. T., “Optimal Design of Variable Stiffness Composite Structures Using Lamination Parameters,” Doctoral Thesis, Delft University of Technology, Delft, 2011.

[45] Joint Aviation Authorities, “JAR25 - Joint Aviation Requirements - Large Aeroplanes, Change 13.” 1989.

[46] Joint Aviation Authorities, “JAR25 - Joint Aviation Requirements - Large Aeroplanes, Change 14.” 1994.

[47] Joint Aviation Authorities, “JAR-OPS 1.” [Online]. Available: http://www.edkb.de/Download%20Angebote/JAR-OPS1.pdf. [Accessed: 31-Jul-2018].

[48] Jones, J., “Statistical-Discrete-Gust Method for Predicting Aircraft Loads and Dynamic Response,” *Journal of Aircraft*, vol. 26, no. 4, 1987.

[49] de Jonge, J. B., Schütz, D., Lowak, H., and Schijve, J., “A Standardized Load Sequence for Flight Simulation Tests on Transport Aircraft Wing Structures,” Technical Report NLR TR 73029 C, Nationaal Lucht- en Ruimtevaartlaboratorium, Amsterdam, 1973.

[50] Kaiser, C., “Alternative Querruderarchitekturen für Verkehrsflugzeuge und aeroelastische Untersuchungen zur Rollmomentenerzeugung,” Master’s Thesis, Universität Stuttgart, Stuttgart, 2013.

[51] Kassapoglou, C., “Fatigue model for composites based on the cycle-by-cycle probability of failure: implications and applications,” *Journal of Composite Materials*, vol. 45, no. 3, pp. 261–277, 2011.

[52] Khodaparast, H., Georgiou, G., Cooper, J., Riccobene, L., Ricci, S., Vio, G., and Denner, P., “Effective Worst Case ‘1-Cosine’ Gust Loads Prediction,” *ASD Journal*, vol. 2, no. 3, pp. 33–54, 2012.

[53] Klimmek, T., “Parametric Set-Up of a Structural Model for FERMAT Configuration for Aeroelastic and Loads Analysis,” *ASD Journal*, vol. 3, no. 2, pp. 31–49, 2014.

[54] Klimmek, T., “Statische aeroelastische Anforderungen beim multidisziplinären Strukturentwurf von Verkehrsflugzeugflügeln,” Doctoral Thesis, Technische Universität Braunschweig, Braunschweig, 2016.

[55] König, R., and Hahn, K. U., “Load Alleviation and Ride Smoothing Investigations Using ATTAS,” *Proceeding of the 17th ICAS*, 1990.

[56] König, R., Hahn, K. U., and Winter, J., “Advanced Gust Management Systems - Lessons Learned and Perspectives,” presented at the Flight Mechanics Panel Symposium, Torino, Italy, 1994.

[57] Krüger, W., Ciampa, P. D., Geier, M., Kier, T., Klimmek, T., Kohlgrüber, D., Ohme, P., Risse, K., and Schwinn, J., “A Comprehensive Load Process at the DLR - Definition, Analysis and Experimental Evaluation,” *Aerospace Lab Journal*, no. 14, Sep. 2018.

[58] Krüger, W., and Klimmek, T., “Definition of a Comprehensive Loads Process in the DLR Project iLOADS,” presented at the Deutscher Luft- and Raumfahrtkongress, 2016.

[59] Krüger, W., Klimmek, T., Liepelt, R., Schmidt, H., Waitz, S., and Cumnuantip, S., “Design and aeroelastic assesment of a forward-swept wing aircraft,” *CEAS Aeroenautical Journal*, vol. 5, pp. 419–433, 2014.

[60] Mayer, H., Schuller, R., and Fitzka, M., “Fatigue of 2024-T351 aluminium alloy at different load ratios up to 10^10 cycles,” *International Journal of Fatigue*, vol. 57, p. 2013.

[61] Miner, M. A., “Cumulative Damage in Fatigue,” *Journal of Applied Mechanics*, vol. 12, 1945.

[62] Molzow, M., and Zimmermann, H., “Influence of Active Controls on the Design Process of a Large Transport Aircraft,” *AGARD Report 794 - Integrated Airframe Design Technology*, 1993.

[63] Moulin, B., and Karpel, M., “Gust Loads Alleviation Using Special Control Surfaces,” *Journal of Aircraft*, vol. 44, no. 1, pp. 17–25, 2007.

[64] MSC Corporation, “MSC Nastran Version 68 - Aeroelastic Analysis User’s Guide,” 2014.

[65] MSC Corporation, “MSC.Nastran 2012 - Design Sensitivity and Optimization User’s Guide,” 2011.

[66] MSC Corporation, “MSC.Nastran 2012 - Quick Reference Guide,” 2011.

[67] Natke, H. G., *Einführung in Theorie und Praxis der Zeitreihen- und Modalanalyse*. Braunschweig: Friedr. Vieweg und Sohn, 1983.

[68] Nieslony, A., “Rainflow Counting Algorithm,” *Rainflow Counting Algorithm - File Exchange - MATLAB Central*, 2010. [Online]. Available: https://de.mathworks.com/matlabcentral/fileexchange/3026-rainflow-counting-algorithm. [Accessed: 05-Oct-2018].

[69] Paletta, N., “Maneuver Load Controls, Analysis and Design for Flexible Aircraft,” Doctoral Thesis, University of Naples Federico II, Napoli, 2011.

[70] Payne, A. O., “The Fatigue of Aircraft Structures,” *Engineering Fracture Mechanics*, vol. 8, 1976.

[71] Pinho Chiozzotto, G., “Improving Aircraft Conceptual Design with Methods for Wing Loads, Aeroelasticity and Mass Estimation,” Doctoral Thesis, Technische Universität Berlin, Berlin, 2017.

[72] Pinho Chiozzotto, G., “Kriterien für die Erstellung eines Lastenkatalogs,” Internal Report IB232-2014 J13, DLR - Institut für Aeroelastik, Göttingen, 2014.

[73] Pototzky, A., and Zeiler, T., “Calculating Time-Correlated Gust Loads Using Matched Filter and Random Process Theories,” *Journal of Aircraft*, vol. 28, no. 5, 1991.

[74] Pratt, K., and Walker, W., “A revised gust-load formula and a reevaluation of v-g data taken on civil transport airplanes from 1933 to 1950,” *NACA Report No. 1206*, 1954.

[75] Pusch, M., Knoblach, A., and Kier, T., “Integrated Optimization of Ailerons for Active Gust Load Alleviation,” *CEAS Aeronautical Journal*, 2019.

[76] Rajpal, D., Kassapoglou, C., and De Breuker, R., “Aeroelastic optimization of composite wings subjected to fatigue loads,” presented at the AIAA/ASCE/AHS/ASC Structures, Structural Dynamics, and Materials Conference, 2018.

[77] Ramsey, H. D., and Lewolt, J. G., “Design Maneuver Loads for an Airplane with an Active Control System,” presented at the 20th Structures, Structural Dynamics, and Material Conference, 1979.

[78] Raveh, D., “Gust-Response Analysis of Free Elastic Aircraft in the Transonic Flight Regime,” *Journal of Aircraft*, vol. 48, p. 4, 2011.

[79] Reckzeh, D., “Multifunctional Wing Moveables: Design of the A350 XWB and the Way to Future Concepts,” presented at the 29th Congress of the International Council of the Aeronautical Sciences, St. Petersburg, 2014.

[80] Regan, C., and Jutte, C., “Survey of Applications of Active Control Technology for Gust Alleviation and New Challenges for Lighter-weight Aircraft,” Technical Report, Dryden Flight Research Center, Edwards, California, 2012.

[81] Rhode, R., and Lundquist, E., “Applied Load Factors in Bumpy Air,” *Aircraft Engineering and Aerospace Technology*, vol. 3, no. 8, pp. 197–200, 1931.

[82] Ritter, M. R., and Quero-Martin, D., “CFD Based Multidisciplinary Maneuver Simulation of Transport Aircraft,” presented at the ECCM ECFD 2018 - 7th European Conference on Computational Fluid Dynamics (ECCOMAS), 2018.

[83] Rosenfeld, M. S., and Huang, S. L., “Fatigue Characteristics of Graphite/Epoxy Laminates under Compression Loading,” *Journal of Aircraft*, vol. 15, no. 5, pp. 264–268, 1978.

[84] Schlichting, H., and Truckenbrodt, E., *Aerodynamik des Flugzeuges, zweiter Band*. Berlin, Heidelberg, New York: Springer, 1969.

[85] Schmidt, H., and Klimmek, T., “ALLEGRA Design Airspeeds and Preliminary Loads,” Internal Report IB 232-2012 J 07, DLR, Institute of Aeroelasticity, Göttingen, 2012.

[86] Schön, J., and Blom, A., “Fatigue life prediction and load cycle elimination during spectrum loading of composites,” *International Journal of Fatigue*, vol. 24, 2002.

[87] Schwochow, J., and Kießling, F., “Aeroelastisches Verhalten mit symmetrisch oszillierenden Querrudern/DLC-Klappen und mit sowie ohne Rauchgenerator,” Technical Report G17-232.13-06–01, DLR, Institute of Aeroelasticity, Göttingen, 2006.

[88] Seitz, A., Kruse, M., Wunderlich, T., Bold, J., and Heinrich, L., “The DLR Project LamAiR: Design of a NLF Forward Swept Wing for Short and Medium Range Transport Application,” presented at the 29th AIAA Applied Aerodynamics Conference, 2011.

[89] Stauffer, W., and Hoblit, F., “Dynamic Gust, Landing and Taxi Loads Determination in the Design of the L-1011,” *Journal of Aircraft*, vol. 10, no. 8, pp. 459–467, 1973.

[90] Tan, X., and Armanios, E., “An Assessment of Fatigue Limit Predictors of Graphite/Epoxy Co-cured Composite Joints through Quasi-static Acoustic Emission Count Peaks,” *Fatigue of Composite Materials*, vol. 3, 2013.

[91] Tetlow, R., “Design Charts for Carbon Fibre Composites,” Technical Report, Cranfield Institute of Technology, Cranfield, 1970.

[92] Teufel, P., “Böenmodellierung and Lastabminderung für ein flexibles Flugzeug,” Doctoral Thesis, Universität Stuttgart, Stuttgart, 2003.

[93] Timoshenko, S. P., and Gere, J. M., *Theory of Elastic Stability*, 2nd ed. McGraw-Hill, 1961.

[94] Torenbeek, E., “Development and Application of a Comprehensive, Design-Sensitive Weight Prediction Method for Wing Structures of Transport Category Aircraft,” Technical Report, Delft University of Technology, Delft, 1992.

[95] University of Liverpool, Institute for Risk and Uncertainty, and Innovate UK, “Second Uncertainty Quantification & Management for High Value Manufacturing Study Group with Industry.” 2017.

[96] US Department of Defense, “MIL-STD-1797A - Flying Qualities of Piloted Aircraft Notice 3,” Technical Report, 2004.

[97] Voß, A., “Design and Structural Optimization of a Flying Wing of Low Aspect Ratio Based on Flight Loads,” Doctoral Thesis, Technische Universität Berlin, Berlin, 2020.

[98] Waszak, M. R., and Schmidt, D. K., “Flight Dynamics of Aeroelastic Vehicles,” *Journal of Aircraft*, vol. 25, no. 6, 1988.

[99] Wildschek, A., “An Adaptive Feed-Forward Controller for Active Wing Bending Vibration Alleviation on Large Transport Aircraft,” Doctoral Thesis, Technische Universität München, München, 2008.

[100] Wildschek, A., Hanis, T., and Stroscher, F., “L∞-optimal Feedforward Gust Load Alleviation Design for a Large Blended Wing Body Airliner,” *Progress in Flight Dynamics, GNC, and Avionics*, vol. 6, pp. 707–728, 2013.

[101] Wildschek, A., Prananta, B., Kanakis, T., van Tongeren, H., and Huls, R., “Concurrent Optimization of a Feed-Forward Gust Loads Controller and Minimization of Wing Box Structural Mass on an Aircraft with Active Winglets,” presented at the 16th AIAA/ISSMO Multidisciplinary Analysis and Optimization Conference, 2015.

[102] Wilson, T., Castrichini, A., Azabal, A., Cooper, J. E., Ajaj, R., and Herring, M., “Aeroelastic Behaviour of Hinged Wing Tips,” presented at the International Forum on Aeroelasticity and Structural Dynamics, Como, Italy, 2017.

[103] Woods-Vedeler, J., and Pototzky, A., “Rolling Maneuver Load Alleviation Using Active Controls,” *Journal of Aircraft*, vol. 32, no. 1, 1992.

[104] Wunderlich, T., “LamAiR - Laminar Aircraft Research UAP 1.1.2 - Flugzeugentwurf Projektbericht Version 3.0,” Technical Report, DLR - Institut für Aerodynamik und Strömungstechnik, Braunschweig, 2012.

[105] Xu, J., “Aircraft Design with Active Load Alleviation and Natural Laminar Flow, Stanford University,” Doctoral Thesis, Stanford University, Stanford, 2012.

[106] Zhao, Y., Yue, C., and Hu, H., “Gust Load Alleviation on a Large Transport Airplane,” *Journal of Aircraft*, vol. 53, no. 6, 2016.

[107] Zill, T., Ciampa, P. D., and Nagel, B., “Multidisciplinary Design Optimization in a Collaborative Distributed Aircraft Design System,” presented at the 50th AIAA Aerospace Sciences Meeting Including the New Horizons Forum and Aerospace Exposition, 2012.

Appendix

Visualization of gust and maneuver loads in the 2D envelopes

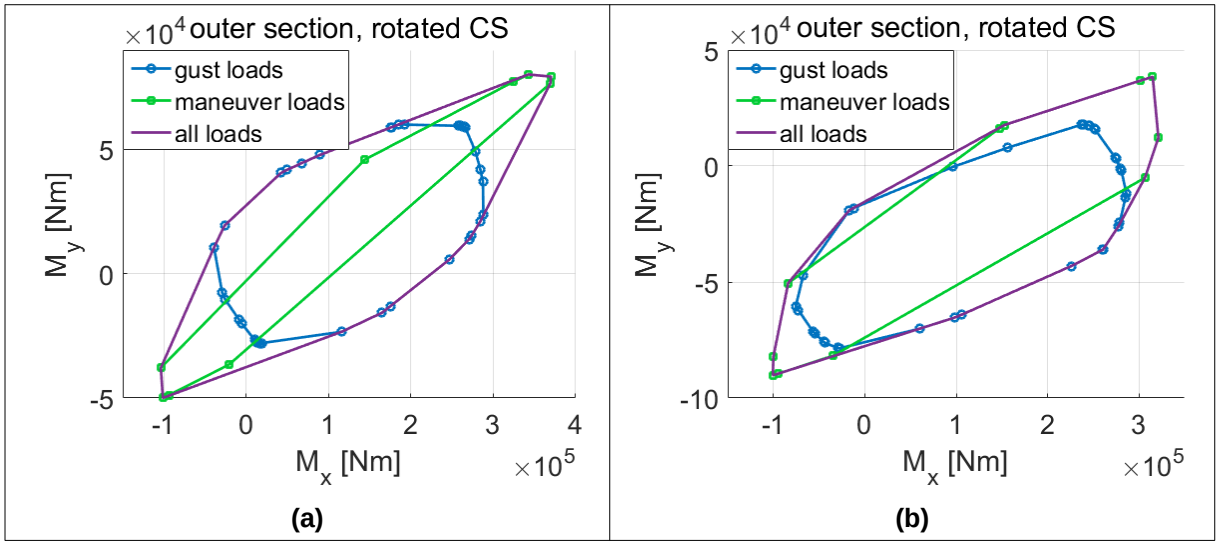

Figure A-1. 2D gust and maneuver load envelopes of active D150 (a) and active ALLEGRA (b)

Selected modes of the reference aircraft

Table A-1. Selected modes of the D150 configuration at operating empty mass

Mode	Frequency	
	Passive aircraft	Active aircraft
First symmetric wing bending	2.86 Hz	2.83 Hz
Second symmetric wing bending	9.32 Hz	9.16 Hz
First symmetric wing torsion	21.88 Hz	21.31 Hz
First symmetric HTP bending	8.41 Hz	8.41 Hz
First VTP bending	10.08 Hz	10.06 Hz
First vertical fuselage bending	5.46 Hz	5.45 Hz

Table A-2. Selected modes of the ALLEGRA configuration at operating empty mass

Mode	Frequency	
	Passive aircraft	Active aircraft
First symmetric wing bending	3.22 Hz	3.13 Hz
Second symmetric wing bending	9.86 Hz	9.41 Hz
First symmetric wing torsion	23.60 Hz	22.51 Hz
First symmetric HTP bending	8.57 Hz	8.55 Hz
First VTP bending	2.42 Hz	2.42 Hz
First vertical fuselage bending	4.58 Hz	4.57 Hz

Flutter curves of the D150 configuration

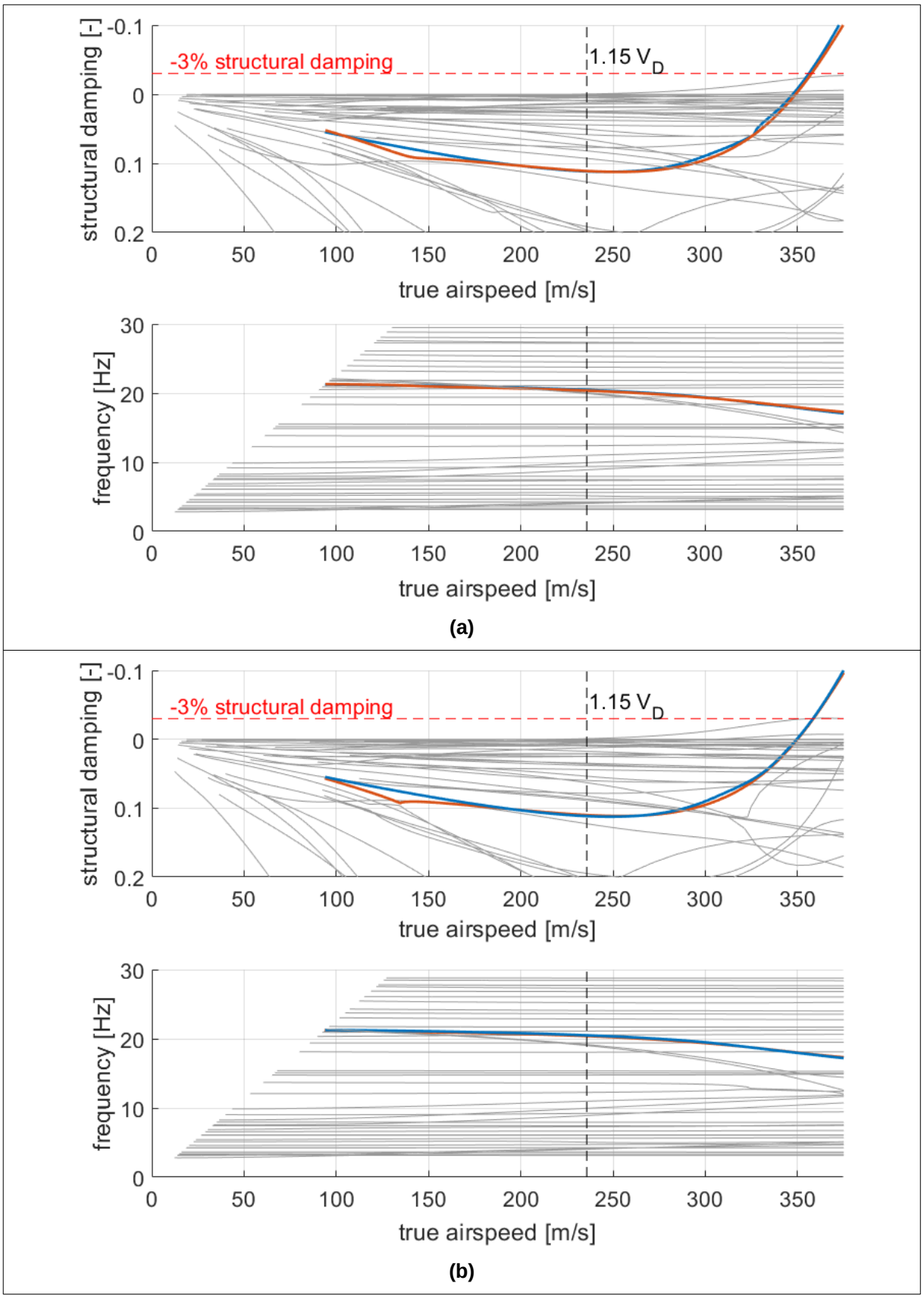

Figure A-2. Flutter curves of the passive (a) and active (b) D150 configuration

The flutter speed of the D150 configuration occurs between 356 and 358 m/s TAS. In Figure A-2, two highlighted flutter curves near each other are visible on both aircraft. Using a manual mode tracking, the dominant modes of the flutter phenomena are identified as the symmetric and antisymmetric HTP torsion, see Figure A-3. Under vacuum condition, those elastic modes have frequencies ranging from 21.2 to 21.3 Hz. At the flutter points, the flutter frequencies of both aircraft range between 17.6 and 17.8 Hz. Furthermore, as apparent in Figure A-3, the fuselage has no relevant participation in the modes.

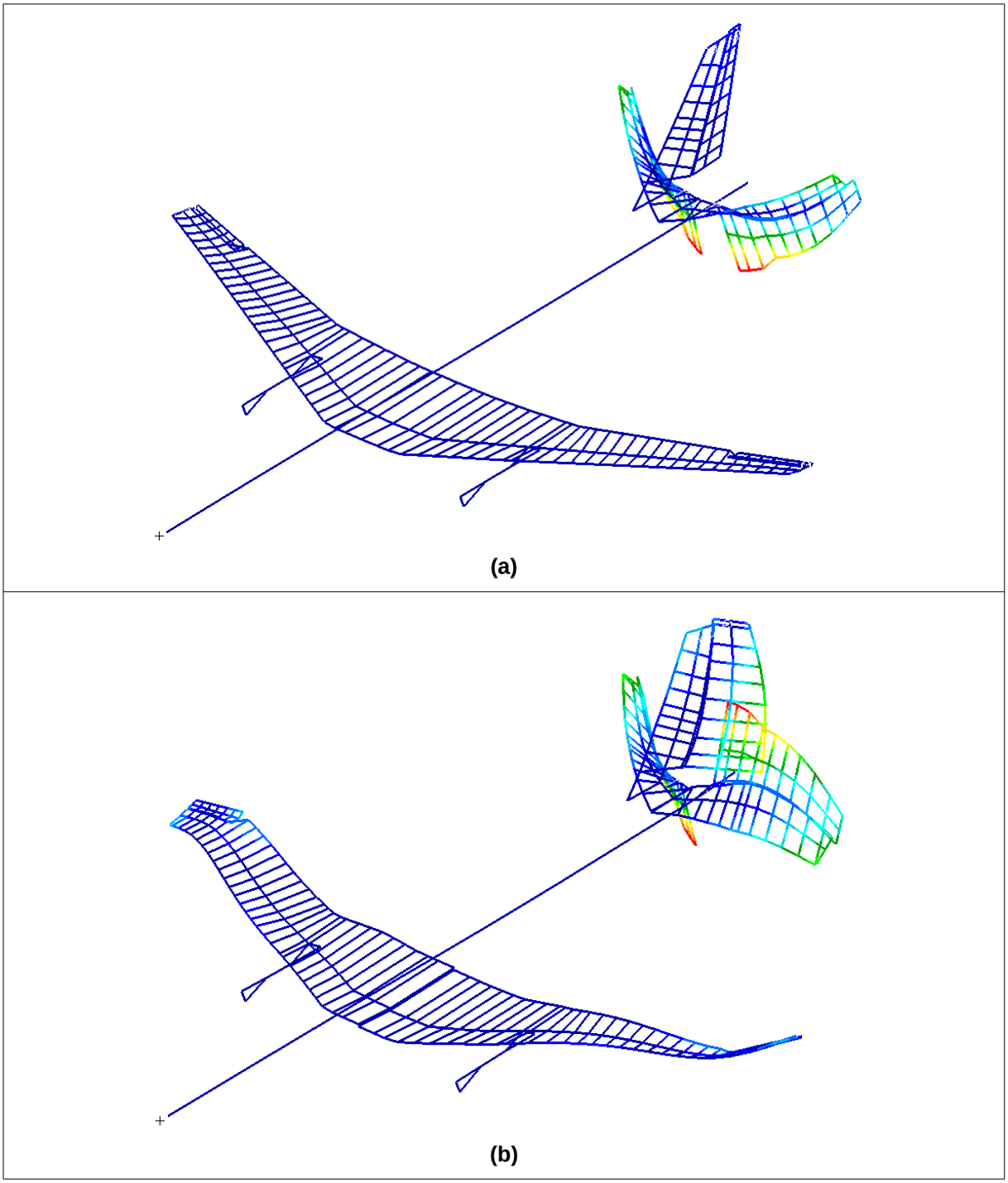

Figure A-3. Symmetric (a) and antisymmetric (b) HTP torsion mode of the D150 configuration

Flutter curves of the ALLEGRA configuration

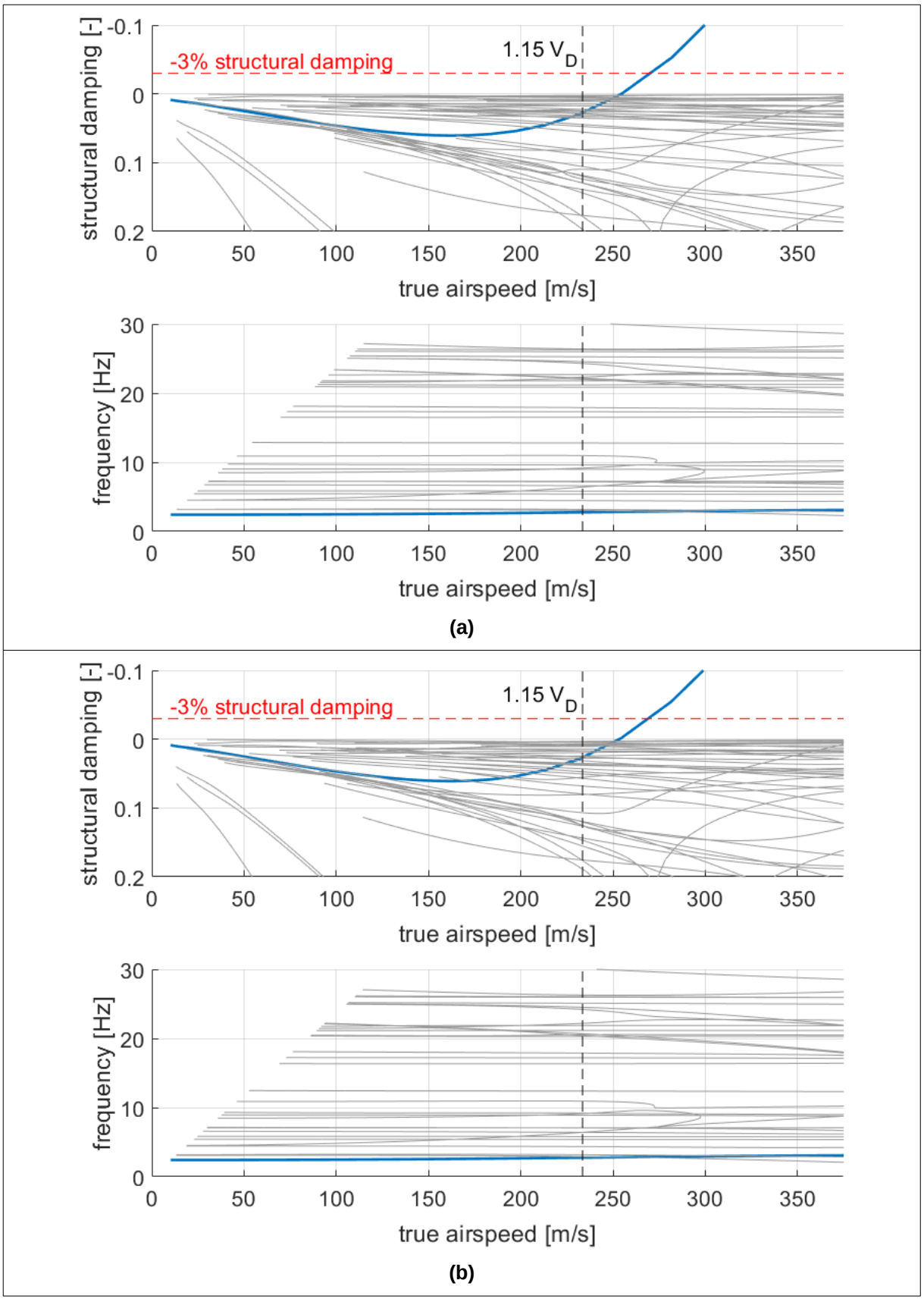

Figure A-4. Flutter curves of the passive(a) and active (b) ALLEGRA configuration

On the ALLEGRA configuration, the flutter point occurs between 269 and 270 m/s TAS. In Figure A-4, the curves leading to the flutter point on both aircraft are highlighted. Using a manual mode tracking, the dominant mode at the flutter speed is the VTP bending, see Figure A-5. Under vacuum condition, the frequency of the elastic mode is 2.42 Hz for both active and passive aircraft. At the flutter points, the flutter frequency of both aircraft is 2.87 Hz. Moreover, from Figure A-5 it is apparent that there is no coupling with the fuselage.

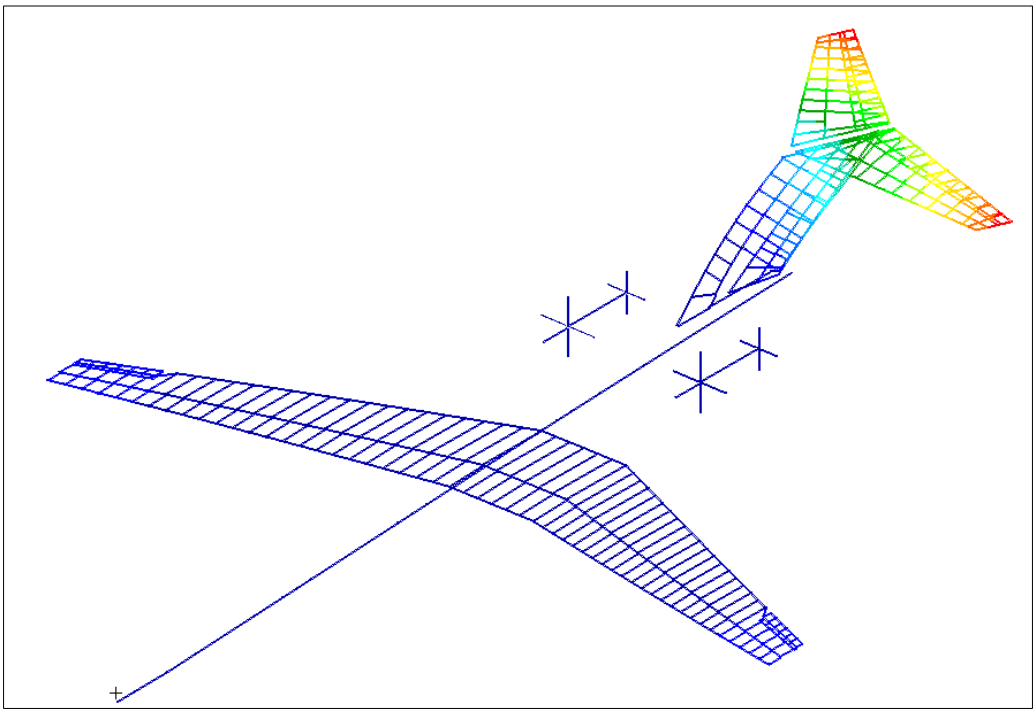

Figure A-5. VTP bending mode of the ALLEGRA configuration

Turbulence fatigue analysis of the D150 configuration

Table A-3. Turbulence fatigue damage per hour on D150

Flight phase	Observed shell element	Retrofitted aircraft	Passive aircraft	Active aircraft
Climb	Wing root	$1.09 \cdot 10^{-15}$	$1.54 \cdot 10^{-12}$	$2.56 \cdot 10^{-15}$
	Outer wing section	$2.76 \cdot 10^{-23}$	$8.59 \cdot 10^{-16}$	$2.68 \cdot 10^{-22}$
	HTP root	$1.15 \cdot 10^{-23}$	$3.17 \cdot 10^{-24}$	$1.41 \cdot 10^{-23}$
Cruise	Wing root	$3.19 \cdot 10^{-26}$	$6.23 \cdot 10^{-23}$	$1.03 \cdot 10^{-25}$
	Outer wing section	$2.33 \cdot 10^{-32}$	$2.65 \cdot 10^{-26}$	$4.14 \cdot 10^{-31}$
	HTP root	$8.27 \cdot 10^{-36}$	$3.71 \cdot 10^{-36}$	$1.22 \cdot 10^{-35}$
Descent	Wing root	$1.18 \cdot 10^{-14}$	$3.06 \cdot 10^{-12}$	$1.79 \cdot 10^{-14}$
	Outer wing section	$4.02 \cdot 10^{-22}$	$1.41 \cdot 10^{-15}$	$8.16 \cdot 10^{-21}$
	HTP root	$3.70 \cdot 10^{-20}$	$5.34 \cdot 10^{-21}$	$9.15 \cdot 10^{-21}$

Turbulence fatigue analysis of the ALLEGRA configuration

Table A-4. Turbulence fatigue damage per hour on ALLEGRA

Flight phase	Observed shell element	Retrofitted aircraft	Passive aircraft	Active aircraft
Climb	Wing root	$3.11 \cdot 10^{-27}$	$1.85 \cdot 10^{-23}$	$7.35 \cdot 10^{-26}$
	Outer wing section	$1.26 \cdot 10^{-31}$	$5.24 \cdot 10^{-26}$	$2.21 \cdot 10^{-29}$
	HTP root	$6.11 \cdot 10^{-24}$	$5.77 \cdot 10^{-34}$	$1.07 \cdot 10^{-33}$
Cruise	Wing root	$5.50 \cdot 10^{-38}$	$5.44 \cdot 10^{-35}$	$5.51 \cdot 10^{-37}$
	Outer wing section	$3.91 \cdot 10^{-43}$	$5.98 \cdot 10^{-38}$	$8.55 \cdot 10^{-41}$
	HTP root	$5.71 \cdot 10^{-46}$	$3.94 \cdot 10^{-46}$	$1.00 \cdot 10^{-45}$
Descent	Wing root	$5.61 \cdot 10^{-27}$	$4.00 \cdot 10^{-23}$	$3.09 \cdot 10^{-26}$
	Outer wing section	$6.49 \cdot 10^{-33}$	$1.47 \cdot 10^{-26}$	$1.05 \cdot 10^{-30}$
	HTP root	$1.49 \cdot 10^{-33}$	$7.87 \cdot 10^{-34}$	$3.65 \cdot 10^{-33}$

ISSN 1434-8454

ISRN DLR-FB—2020-47